INFORMATION TO USERS

This manuscript has been reproduced from the microfilm master. UMI films the text directly from the original or copy submitted. Thus, some thesis and dissertation copies are in typewriter face, while others may be from any type of computer printer.

The quality of this reproduction is dependent upon the quality of the copy submitted. Broken or indistinct print, colored or poor quality illustrations and photographs, print bleedthrough, substandard margins, and improper alignment can adversely affect reproduction.

In the unlikely event that the author did not send UMI a complete manuscript and there are missing pages, these will be noted. Also, if unauthorized copyright material had to be removed, a note will indicate the deletion.

Oversize materials (e.g., maps, drawings, charts) are reproduced by sectioning the original, beginning at the upper left-hand corner and continuing from left to right in equal sections with small overlaps.

ProQuest Information and Learning
300 North Zeeb Road, Ann Arbor, MI 48106-1346 USA
800-521-0600

Near and Far Field Comparison Using Wire-Grid and Patch Models

Leslie Robert Raschkowan

A Thesis

in

The Department of

Electrical and Computer Engineering

Presented in Partial Fulfillment of the Requirements
for the Degree of Master of Applied Science at
Concordia University
Montreal, Quebec, Canada

March 2003

ABSTRACT

Near and Far Field Comparison Using Wire-Grid and Patch Models

Leslie Robert Raschkowan

This thesis examines the accuracy of near field computations obtained using wire grid and surface patch method of moments models. Wire grid results were obtained using *NEC*, a point matching implementation, and *MBC*, a Galerkin implementation. The surface patch results were obtained using *Junction*. In the near field, a flat plate and a sphere illuminated with an incident plane wave are investigated. For the far field examinations, wire grid models examine the radar cross section of two flat plates as well as the radiation pattern of a monopole mounted on a sphere. In addition, a high frequency band sweep of a helicopter model is performed.

Good near field results are obtained using wire grid models so long as the field points are not too close to the wires. Patch models allow field points much closer to the surface since the current is distributed over the surface. Excellent far field results are obtained for both the plate and the sphere. The frequency sweep generally showed good results though anomalies were evident at certain frequencies.

Wire grid results were obtained using *NEC* and *MBC* though the results indicate that the type of Moment Method formulation for wire grids was not a major factor. Surface patch results obtained with *Junction* were used to validate the wire grid near field plate results. Validation for the sphere is by an exact solution.

ACKNOWLEDGEMENTS

It has been a long journey to get to this point and I would sincerely like to thank Dr. Robert Paknys for guiding the way. I have truly enjoyed our many discussions on various related topics. I would also like to thank Dr. Stan Kubina for his advice over the years. His enthusiasm of his on-going research and guidance during this period has been an inspiration.

I have enjoyed my many technical discussions with Ken Deegan who has provided insight into many different aspect of engineering. Similarly, Michael Slater's endeavours and determination have served as a personal source of motivation. Special thanks to Richard Hull for having proof read my work.

I would like to mention a few people who have given me inspiration over the years. I have always considered myself lucky to have a personal friend like Robert Marx M.D. who I have always considered a 'top gun'. I have always admired how my friend Peter Maag has combined his wit, intelligence, and unique character into the successful career he has made for himself. I must also mention my special friend Neil Davies who is always happy-go-lucky with a clear vision of his priorities.

I wish to thank my brother Norman for the support over the years, and for being an example of being able to excel in business and still a nice guy. I would also like to thank my brother Walter for helping me to focus on my thesis and offering sound advice for getting it completed.

Special mention to my parents who always instilled the importance of education but also for allowing me to make mistakes along the way. My mother's return to school to complete her university degree after having her three children was an impressive accomplishment. I wish my father would have still been around to see mine.

Lastly, the most important factor that helped me complete this thesis was the encouragement and sacrifice my wife Johanne made for me. Existing these last months as "the thesis widow", to quote my friend Mr. Slater, was a task she took on willingly

and without reservation. This work would never have been completed without you. I love you.

Contents

List of Figures

List of Tables

LIST OF SYMBOLS

A	Vector potential function
E	Electric field
E^{inc}	Incident electric field
E^{scatt}	Scattered electric field
H	Magnetic field
J_S	Electric surface current density
J_T	Total electric current density
M_S	Magnetic surface current density
P_f	Poynting vector
S	Power density
β or k	Phase contant or wave number
ϵ	Permittivity
η	Intrinsic impedance
η_o	Intrinsic impedance of free space
λ	Wavelength (in metres)
μ	Permeability
ω	Radial frequency
ρ_T	Total electric charge
σ	Conductivity
σ	Radar Cross-Section
σ_S	Surface charge density
V	Voltage
I	Current
Z	Impedance
a	Wire radius

$\hat{n}$	Unit vector normal to wire surfaces
Δ	Wire segment length
$\hat{J}_n(\ )$	Bessel function of the first kind
$H_n^{(2)}(\ )$	Hankel function of the second kind
W_m	Weighting function

Chapter 1

Introduction

Computational Electromagnetics (CEM), the study of electric and magnetic fields using numerical techniques or simulations, continues to benefit from the ongoing advances in micro-computer technology. Powerful software tools, such as the Numerical Electromagnetics Code (NEC)[1] and Multi-radius Bridge Currents (MBC)[2] can be used to solve scattering or antenna problems for very complex geometries.

The continuing growth of computing power available in workstations and personal computers allows researchers to further push the limits of these simulation techniques, and to determine stricter guidelines for their accurate use.

1.1 Background

The prediction and analysis of antenna radiation characteristics has been a field of intense interest since the advent of wireless communications. Naval and aviation applications drove much of the research that continues to this day. Far field analyses, such as Radar Cross Section prediction, continue to be applied in the aerospace realm producing advances such as the development of stealth technology.

An application of interest to both near and far field antenna analysis is the effect of mounting an antenna on the fuselage or structures of various aircraft. Depending on the location of the antenna installation, considerable distortion of the radiated fields can occur.

Computer modelling of antennas on structures provides a relatively low cost alternative to full scale or scale-model measurements which require weather dependant outdoor or expensive indoor ranges. Antenna location or characteristics can be modified and measurements "easily" recalculated providing designers and researchers great flexibility.

In addition, the near field present near a conducting surface is of great interest in antenna and electromagnetic compatibility applications. The prediction of potential hazard to personnel or equipment in the presence of strong EM sources is such an example. The electromagnetic compatibility of an antenna to nearby equipment has proven catastrophic in the past. During the Viet Nam war in the 1960s, a high power radar sweep aboard a United States aircraft carrier triggered a military aircraft to accidentally fire a missile while on deck of the carrier resulting in a terrific chain of explosions, fire and loss of life.

1.1.1 Wire Grid Modelling

Historically, Richmond's *Thin Wire* code [3] was one of the first applications to apply method of moment modeling of arbitrary shapes with wire grid models. This ground breaking effort included numerical results for the backscatter echo area of wire loops, plates, spheres and hemispheres which showed good agreement with experimental data. *Thin Wire* employed point-matching by forcing the tangential electric field to vanish at the center of each wire segment.

Tilston and Balmain significantly extended Richmond's code after observing asymmetric artifacts displayed when analyzing symmetric structures [4]. The development of *Multi-radius Bridge Current MBC* code [2] addressed this problem and provided a multi-radius solution instead of the uniradius Thin Wire code. MBC implements a *piecewise-sinusoid Galerkin* formulation shown to be one of the best methods for obtaining rapid convergence [5].

The development of *Numerical Electromagnetics Code (NEC)*[1] had its origins

in a scattering code *BRACT*[6] spawned from some of Richmond's early work[7]. *Antenna Modelling Program (AMP)*[8], based on BRACT, was one of the first widely used moment method implementations, and a subsequent revision of AMP was used to develop NEC. NEC uses the moment method to solve the electric field integral equation (EFIE) for wire models and/or the magnetic field integral equation (MFIE) for surface patch models. The EFIE is suitable for both open and closed bodies but the MFIE applies only to closed surfaces. In this thesis, NEC is only used for wire models.

1.1.2 Surface Patch Modelling

Patch models can accurately represent surface current for smooth bodies without sharp edges. NEC uses rectangular patches to represent surfaces however the MFIE based solution is only appropriate for closed bodies. An EFIE formulation using planar rectangular patches was developed by Wang *et al*[9]. The use of quadrilateral patches and sinusoidal basis functions was presented by Singh and Adams[10], also using the EFIE.

Triangular shaped surfaces are the most appropriate for modelling arbitrary shapes because of ability to accurately conform to any shape or boundary. Rao *et al.*[11] developed a surface patch code *Patch* combining the advantages of triangular patch modeling and using the EFIE formulation allowing scattering problems by either open or closed arbitrary conducting bodies.

1.2 Objective of the Report

There are several different codes available to analyze antenna and scattering problems, however it seems as though NEC is considered to be a benchmark. A great deal of analysis has been done with this code to discover the limitations of its use, and several guidelines have been developed that should to be followed to obtain "accurate"

results.

In some cases, even when these guidelines are followed, anomalies in the results occur. These problems include ficticious loop currents in the solution and incorrect currents at the cavity resonant frequencies of the scatterer[11].

The EMC laboratory at Concordia University has been involved in the development of several software packages used for the visualization and analysis of NEC solution files. One of the objectives of this project is to utilize a different EM code, specifically MBC, and perform a side-by-side comparison of the two sets of results.

Both codes are implementations of the Method of Moments, a numerical technique to calculate the fields in radiating or scattering problems. The MBC code utilizes the Galerkin method, considered to be better than the *point-matching* approach used by NEC. Thus this report will also serve to compare the Galerkin method to the point-matching approach.

Another objective is to examine the near field results of two basic geometric forms, a plate and a sphere, and try to "push the codes to the limit". The objective is to attempt to attain an effective modelling guideline using the ratio of the model grid size and the minimum height above the model that can still provide an accurate result.

1.3 Methodology of the Report

The comparison of the two codes will be broken down into two sections: Chapter 4 will focus on the near field experiments and Chapter 5 will focus on the far field.

1.3.1 Near Field Experiments

In the near field, the comparison of the two codes will consist of two separate evaluations:

1. Near-field scattering of a plane wave incident on a conducting square plate

2. Near-field scattering of a plane wave incident on a conducting sphere.

Near-field scattering of a plane wave incident on a conducting square plate

The solutions generated by the two codes will be compared to each other to evaluate how close to the wire-grid model the codes can accurately predict the scattered fields. The equal area rule is investigated by varying the radii of the wire-grid models.

Near-field scattering of a plane wave incident on a conducting sphere

The solutions generated by the two codes will be compared to an exact solution to evaluate the accuracy of the codes. In one case, the wire radii of the wire-model sphere will vary to investigate the same surface rule. In another case, the height above the surface of the sphere will vary to help determine a grid size to height relationship.

1.3.2 Far Field Experiments

In the far field, the comparison of the two codes will consist of three separate evaluations:

1. Radar Cross-Section of a square and rectangular plate
2. Far-field radiation pattern of an antenna placed upon a conducting sphere
3. High frequency sweep of a complex helicopter model.

Radar Cross-Section of a square and rectangular plate

The solutions generated by the two codes will be compared to an approximate solution obtained using physical optics theory, to provide an indication of the accuracy of the codes.

Far-field radiation pattern of an antenna placed upon a conducting sphere

The computed radiation patterns generated by the two codes will be compared to the exact analytical solution to evaluate the accuracy of the codes.

High frequency sweep of a complex helicopter model

The comparison between the two models will consist of a high frequency sweep, ranging from 2.0 MHz to 30.0 MHz, in 0.1 MHz increments. The radiated power, efficiency, and impedance characteristics will be compared. The radiation patterns as well as the current distributions will also be presented.

Chapter 2

Antenna Analysis

2.1 Basic Antenna Theory

2.1.1 Maxwell's Equations

Antenna radiation is an electromagnetic boundary problem, where radiated fields must satisfy Maxwell's equations, the wave equation and the boundary conditions.

The fundamental electromagnetics equations are

$$\nabla \times \mathbf{E} = -j\omega\mu\mathbf{H} \tag{2.1}$$

$$\nabla \times \mathbf{H} = j\omega\epsilon\mathbf{E} + \mathbf{J}_T \tag{2.2}$$

$$\nabla \cdot \mathbf{D} = \rho_T \tag{2.3}$$

$$\nabla \cdot \mathbf{B} = 0 \tag{2.4}$$

$$\nabla \cdot \mathbf{J}_T = -j\omega\rho_T. \tag{2.5}$$

The first four equations are called Maxwell's equations, and the fifth is the continuity equation. Note that the $e^{j\omega t}$ time dependence is assumed and suppressed.

"A sufficient set of boundary conditions (in the time-harmonic form) is

$$\hat{n} \times (\mathbf{H_2} - \mathbf{H_1}) = \mathbf{J_s} \tag{2.6}$$

$$(\mathbf{E_2} - \mathbf{E_1}) \times \hat{\mathbf{n}} = \mathbf{M_s} \tag{2.7}$$

where the electric and magnetic surface currents, $\mathbf{J_S}$ and $\mathbf{M_S}$, flow on the boundary between two homogeneous media."[12] The unit normal vector is directed from medium one to medium two, as illustrated in Figure 2.1.

If one side is an ideal electrical conductor, the boundary conditions become

$$\mathbf{H_{tan}} = \mathbf{J_S} \tag{2.8}$$

$$\mathbf{E_{tan}} = 0. \tag{2.9}$$

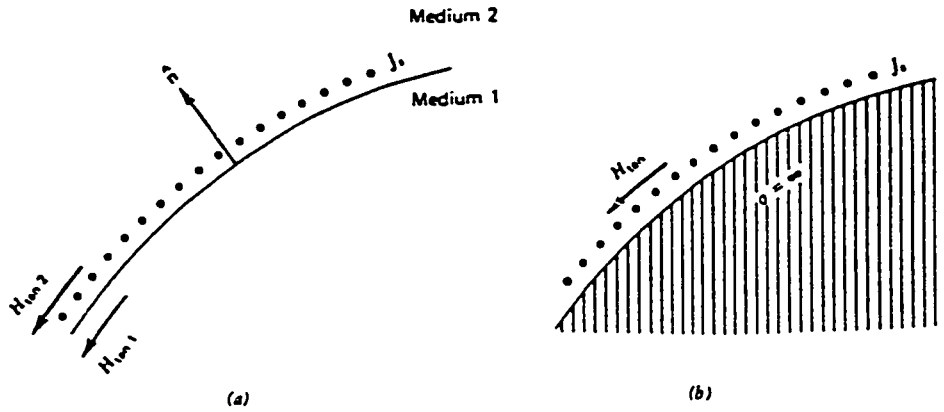

Figure 2.1: Boundary conditions between two media: (a) two homogeneous media, (b) perfect conductor and a homogeneous medium.[12]

2.1.2 Antenna Radiation

If we consider a sinusoidal voltage source applied to an open-ended conducting wire, the source causes electrons in the conductor to accelerate along the wire. As illustrated in Figure 2.2, the electrons build up at the open end of the wire, opposing the initial electron motion. It is this acceleration and deceleration of charge which produces EM radiation[14].

2.1.3 Solution of Maxwell's Equations for Radiation Problems

The procedure for solving the **E** and **H** field from the current distribution J involves solving two curl equations (2.1) and (2.2). These equations are said to be "coupled" because the **E** and **H** terms appear in both, thus they must be solved simultaneously. In order to simplify the solution of **E** and **H** with a given **J**, it is convenient to introduce the vector potential function **A**.

Since equation (2.4) states that $\nabla \cdot \mathbf{H} = 0$, and the vector identity $\nabla \cdot \nabla \times \mathbf{F} \equiv 0$ for any F, we define

$$\mathbf{H} = \nabla \times \mathbf{A}. \tag{2.10}$$

The complete solution is outlined in many sources. The total solution is then found to be

$$\mathbf{A} = \int\int\int \mathbf{J} \frac{e^{-j\beta \mathbf{R}}}{R} dv', \tag{2.11}$$

where the geometry is shown in Figure 2.3.

We then find the magnetic field **H** from the resulting **A** using equation (2.10) and the electric field using equation (2.1). These results are then used to examine the

Figure 2.2: Open-ended wire with a sinusoidal source.[13]

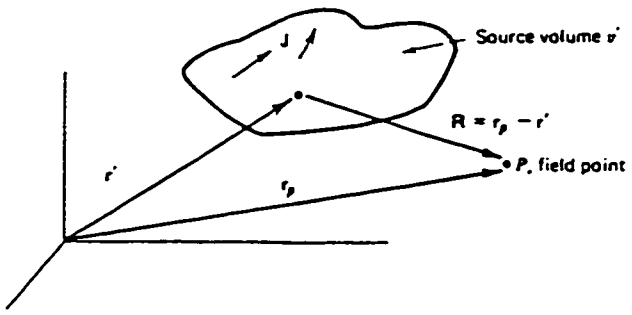

Figure 2.3: Vectors used to solve radiation problems.[12]

radiation of a standard antenna element.

2.2 Ideal Dipole

The principles described in the previous section will now be applied to an ideal dipole, which is a uniform amplitude current element of very small finite length, $z \ll \lambda$. This element can be considered to be a building block to construct a real antenna.

Consider the dipole of constant current amplitude I, shown in Figure 2.4. The segment length is small compared to the wavelength and the distance R. The vector potential function reduces to

$$\mathbf{A} = \hat{\mathbf{z}}\mathbf{I}\int_{\frac{-\Delta z}{2}}^{\frac{\Delta z}{2}} \frac{e^{-j\beta \mathbf{R}}}{4\pi R} dz'. \tag{2.12}$$

Substituting r for R and integrating, we obtain

$$\mathbf{A} = I\Delta z \frac{e^{-j\beta r}}{4\pi r}\hat{\mathbf{z}}. \tag{2.13}$$

This is the approximate solution for a finite element. For an infinitesimal element, this result is exact. Next we calculate the electromagnetic fields as outlined in the previous section to obtain

$$\mathbf{H} = \frac{I\Delta z}{4\pi} j\beta\left(1 + \frac{1}{j\beta r}\right)\frac{e^{-j\beta r}}{r}\sin\theta\,\hat{\phi} \tag{2.14}$$

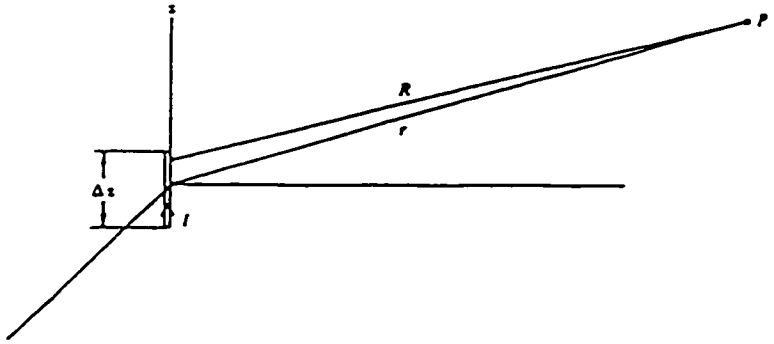

Figure 2.4: The ideal dipole with uniform current I, $\Delta z \ll \lambda$, and $R \approx r$.[12]

$$\mathbf{E} = \frac{I\Delta z}{4\pi} j\omega\mu \left[1 + \frac{1}{j\beta r} + \frac{1}{(j\beta r)^2}\right] \frac{e^{-j\beta r}}{r} \sin\theta\, \hat{\theta} + \frac{I\Delta z}{2\pi} j\omega\mu \left[\frac{1}{j\beta r} + \frac{1}{(j\beta r)^2}\right] \frac{e^{-j\beta r}}{r} \cos\theta\, \hat{\mathbf{r}}. \tag{2.15}$$

2.3 Antenna Characteristics

2.3.1 Near Field (Scattering)

In the near-field region of an antenna, the powers of inverse r terms of the field expressions (2.14) and (2.15) are significant. The Poynting vector,

$$\mathbf{P_f} = \frac{1}{2} \int\int \mathbf{E} \times \mathbf{H}^* ds \tag{2.16}$$

is the complex power flowing out of a closed surface. The complex Poynting vector contains three or more terms with powers of (1/r) in addition to the radiation field term. It turns out that these terms are purely imaginary, indicating reactive power[12].

A plane wave's propagation will be affected by a conducting structure. A conducting object will reflect a wave according to Snell's law, where $\theta_i = \theta_r$[15], as illustrated in Figure 2.5.

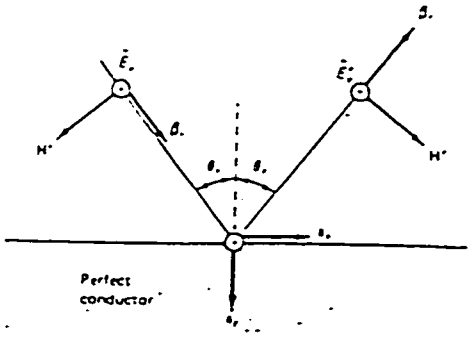

Figure 2.5: Reflection from a perfect conductor.[16]

The reflected wave will cause additive and destructive interference to occur. This phenomena is known as scattering. An example of a plane wave incident on a wire-grid sphere is presented in Figure 2.6.

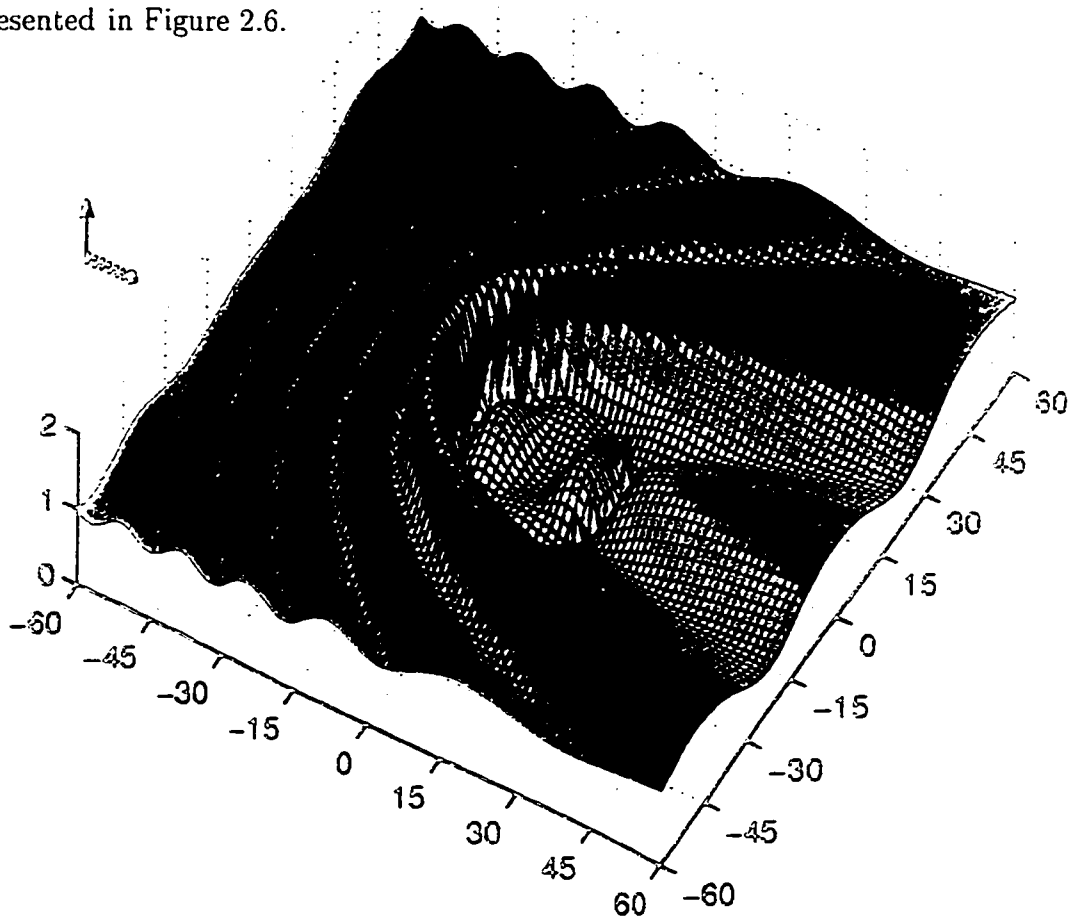

Figure 2.6: Near field of a $\hat{z}$-polarized plane wave incident at 12.5MHz on a 15m radius sphere.

Figure 2.7 shows the standard spherical coordinate system used in this report. It can be used as a reference for the remaining antenna characteristics.

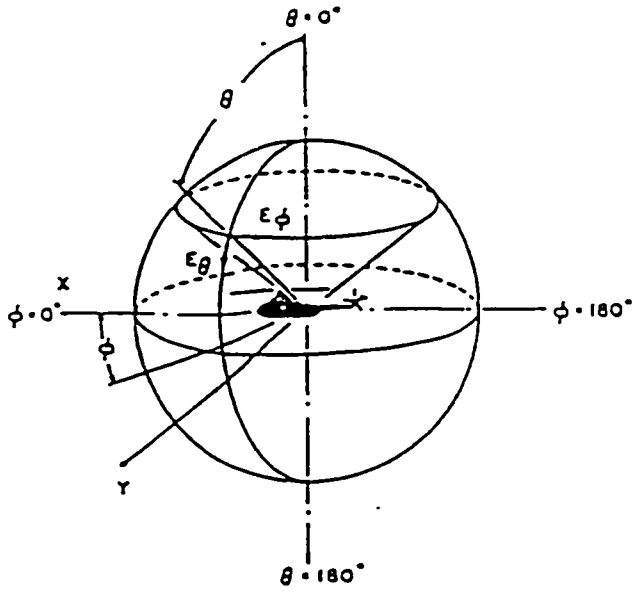

Figure 2.7: Standard spherical coordinate system.[17]

2.3.2 Radiation Pattern (Far Field)

The far-zone fields, or simply the far field, is the region where $\beta r \gg 1$. In this region, the higher order terms become much less significant, and allows us to write Equations (2.14) and (2.15) as

$$\mathbf{E} = \frac{I\Delta z}{4\pi} j\omega\mu \frac{e^{j\beta r}}{r} \sin\theta\hat{\theta} \tag{2.17}$$

and

$$\mathbf{H} = \frac{I\Delta z}{4\pi} j\beta \frac{e^{j\beta r}}{r} \sin\theta\hat{\phi}. \tag{2.18}$$

In the far field, the radiation can be treated as "locally plane" waves, where $\eta_o = E_\theta/H_\phi$.

The radiation pattern is a representation of the far field strength with respect to a fixed distance from the antenna. The idea is to obtain the field strength at various positions, as depicted in Figure 2.8a. Two 2-dimensional patterns, or "cuts," are usually presented: The E plane, representing the magnitude of the normalized field

strength versus θ for a constant ϕ, and the H plane which represents the same field versus ϕ for $\theta = \frac{\pi}{2}$[18]. Figure 2.8 shows the radiation patterns for a z directed dipole.

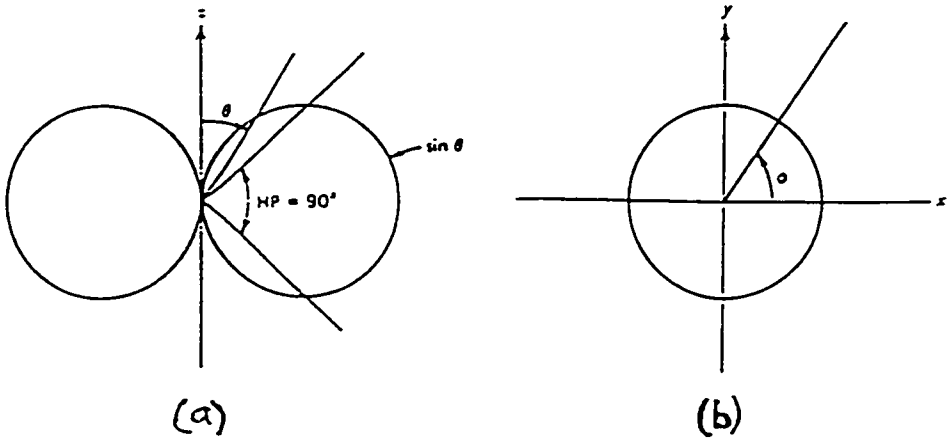

Figure 2.8: Radiation pattern for a z directed dipole. (a) E-plane. (b) H-plane.[18]

2.3.3 Isotropic Level

The isotropic level provides a reference for comparing the directive properties of antennas. The isotropic level is found by taking the total radiated power of the original source, and distributing it uniformly in all directions[19]. An illustration of the radiation pattern of a half-wave dipole and its equivalent isotropic radiator is shown in Figure 2.9.

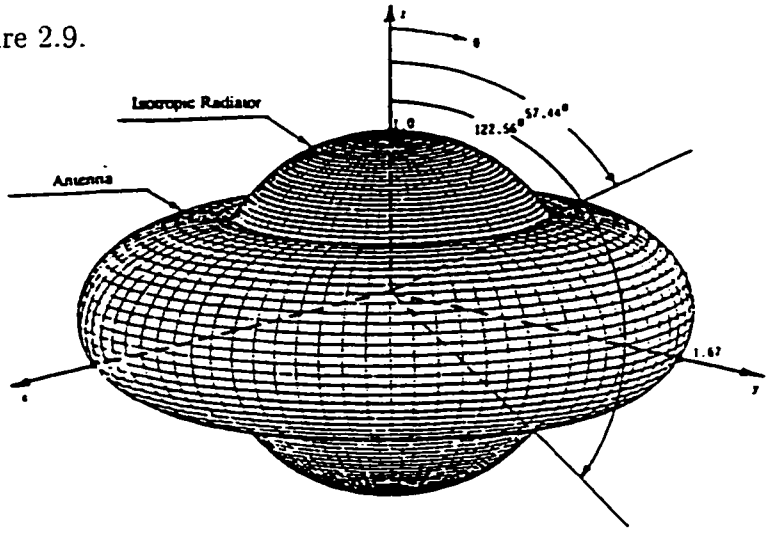

Figure 2.9: Three-dimensional directivity pattern for a $\lambda/2$ dipole and an isotropic source.[20]

2.3.4 Radar Cross-Section (RCS)

The principle of the radar cross-section can be described as the far-field scattering of a plane wave incident on a conducting object. More specifically, an antenna with a gain of G_T transmits a pulse of power P_T, and a receiving antenna with a gain of G_R detects power scattered from a target. Mono-static radar uses the same antenna for transmitting and receiving, while bistatic radar employs a different receiver and transmitter antenna, as illustrated in Figure 2.10.

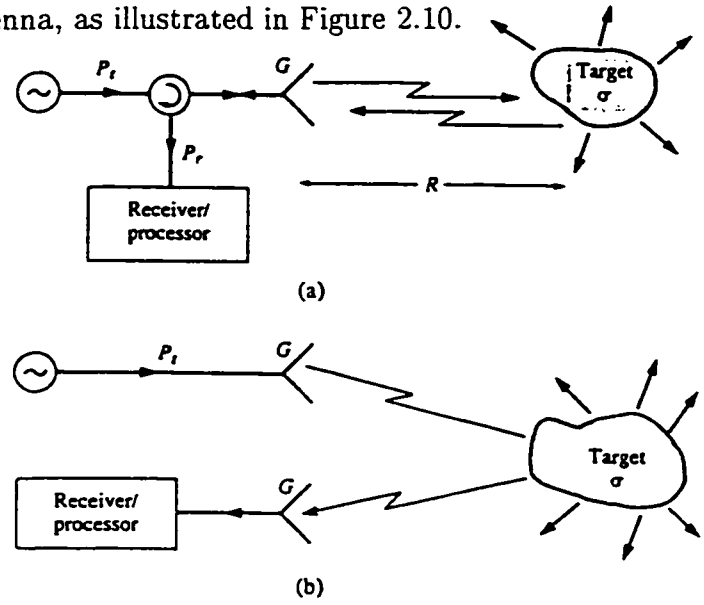

Figure 2.10: Radar Cross-Section examples: (a) Mono-static and (b) bistatic.[21]

"The power intercepted by the target is proportional to the incident power density, so

$$P_{inc} = \sigma S_{inc} = \sigma \frac{P_T}{4\pi r^2} G_T \tag{2.19}$$

where σ is the *radar cross-section* and is the equivalent area of the target as if the target reradiated the incident power isotropically "[22], although in reality this is not the case. The apparent scattered power density arriving at the receiver is

$$S_{scat} = \frac{P_{inc}}{4\pi r^2} \tag{2.20}$$

and the power at the receiver is given by the *radar equation*, in the form of

$$P_R = P_T \frac{\lambda^2 G_R G_T \sigma}{(4\pi)^3 r^4}. \tag{2.21}$$

The radar cross section is the ratio between P_{inc} and P_{scat} given by

$$\sigma = \lim_{r\to\infty} \frac{4\pi r^2 S_{scat}}{S_{inc}} = \lim_{r\to\infty} \frac{4\pi r^2 |E_{scat}|^2}{|E_{inc}|^2}. \tag{2.22}$$

2.3.5 Radiation Efficiency

As much power as possible should be radiated in the solid angle between theta equal 60 and theta equal 120 degrees, for adequate HF antenna communication. "The radiation pattern efficiency, denoted by η_p, is the ratio of the power in both E_θ and E_ϕ in this sector, to the total power radiated by the antenna."[23] The expression, defined by Granger[24] is given by

$$\eta_p = \frac{\int_{\phi=0}^{360}\int_{\theta=60}^{120}(|E_\theta|^2 + |E_\phi|^2)\sin\theta d\theta d\phi}{\int_{\phi=0}^{360}\int_{\theta=0}^{180}(|E_\theta|^2 + |E_\phi|^2)\sin\theta d\theta d\phi} * 100\%. \tag{2.23}$$

2.3.6 Terminal Impedance

The terminal impedance of an antenna will be affected by other antennas or objects that are nearby, but the antenna is to be considered isolated for this report. The input impedance is composed of a real and an imaginary component, namely

$$Z_{in} = R_{in} + jX_{in}. \tag{2.24}$$

The input reactance, X_{in}, represents the power stored in the near field of the antenna. The input resistance, R_{in}, represents dissipation, which occurs in two ways: (i) The heat losses on the antenna and associated hardware are called ohmic losses; and (ii) the power leaving the antenna through radiation, which is of course the purpose of a communication antenna. Usually, the ohmic losses are small compared to the radiated power[25].

2.3.7 Percent E_θ (% E_θ)

The "percent E_θ" parameter is the ratio of the E_θ or vertical component of the power radiated, to that of the total power radiated by the antenna. This is given by

$$\%E_\theta = \frac{\int_{\phi=0}^{360}\int_{\theta=0}^{180}|E_\theta|^2 \sin\theta d\theta d\phi}{\int_{\phi=0}^{360}\int_{\theta=0}^{180}(|E_\theta|^2 + |E_\phi|^2)\sin\theta d\theta d\phi} * 100\%. \tag{2.25}$$

Emphasis is put on maximizing the radiated power in the vertical component when considering the ground wave mode of propagation[26].

2.3.8 Percent sub E_θ (% sub E_θ)

The "percent sub E_θ" or useful percent of E_θ parameter was introduced by Kubina[27]. It is the ratio of the power contained in E_θ between theta equal to 60 and theta equal to 120, to the total power radiated by the antenna. % Sub E_θ is given by the expression

$$\%subE_\theta = \frac{\int_{\phi=0}^{360}\int_{\theta=60}^{120}|E_\theta|^2 \sin\theta d\theta d\phi}{\int_{\phi=0}^{360}\int_{\theta=0}^{180}(|E_\theta|^2 + |E_\phi|^2)\sin\theta d\theta d\phi} * 100\%. \tag{2.26}$$

Chapter 3

Theoretical Basis

Electromagnetic problems usually lead to partial differential equations which have to be evaluated taking into account boundary and initial conditions corresponding to the problem under consideration. *Direct Methods* are methods that provide approximate numerical solutions for differential and integral equations by reducing the problem into a finite system of algebraic equations[28].

In many cases, it is convenient to replace the problem by using an equivalent problem. For instance, it would be desirable to replace integrating a differential equation with a function that results in a simple integral. Such problems are call *Variational Problems*, and methods which allow us to reduce the problem of integrating a differential equation to the equivalent variational problem are called *Variational Methods*.

In 1915, Galerkin[29] published a paper describing a method that did not tie directly to any Variational Method and could thus be applied to any differential or integral equation.

Harrington[30] applied the *Method of Moments* to electromagnetic theory using a general approach that can be applied to almost any analytical or numerical problem.

3.1 Method of Moments

The assumption of a uniform current distribution on the ideal dipole provided a relatively easy method of obtaining the fields caused by the current. We could greatly

increase the number of antenna configurations by eliminating the assumption of the current distribution, however we would need a "general method capable of yielding answers whose accuracy is within the limit of experimental error"[31].

The *method of moments* is the general approach used in both NEC and MBC. It is a procedure for reducing an integral equation of the form

$$\int I(z')K(z,z')dz' = -E^i(z) \tag{3.1}$$

to a system of simultaneous linear algebraic equations in terms of the unknown currents I(z'). We can always express radiation problems as an integral equation in the form of Equation (3.1).

The integral equation is a problem that can only be solved by numeric methods and until only recently was computationally restrictive. The availability of powerful, high speed computers has now made it possible to solve increasingly complex problems, permitting users to test the limits of these simulation techniques.

3.1.1 Pocklington's Integral Equation

In 1897, Pocklington derived a common integral equation arising from the treatment of wire antennas or scatterers. This derivation "enabled him to show that on thin wires the current distribution is approximately sinusoidal and propagates with nearly the speed of light"[31].

Consider the geometry of Figure 3.1.

Assuming that the wire radius $a \ll \lambda$, but that the wire is not infinitely thin, it can be shown that the following integral equation results

$$\frac{1}{j\omega\epsilon_o}\int_{-L/2}^{L/2} I(z')\left[\frac{\delta^2\psi(z,z')}{\delta z^2} + \beta^2\psi(z,z')\right]dz' = -E_z^i(z). \tag{3.2}$$

where $\psi(z,z')$ is the free space Green's function, given by

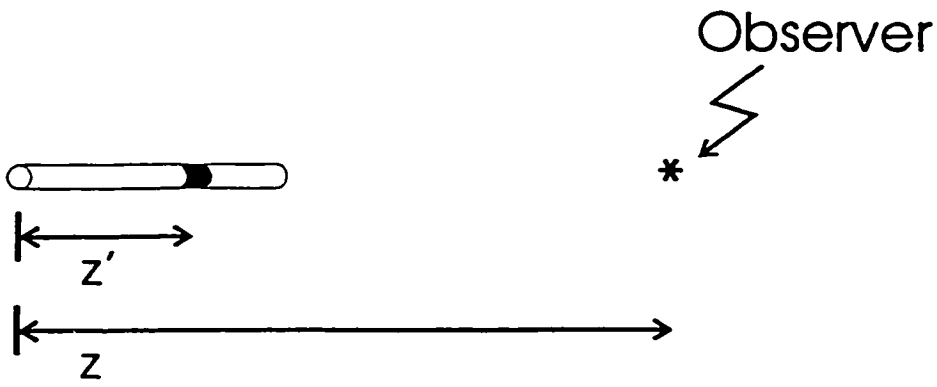

Figure 3.1: Geometry of Pocklington wire segment[31].

$$\psi(z,z') = \frac{e^{-j\beta R}}{4\pi R}, \tag{3.3}$$

where R is the distance from the source to the observer, generally given by

$$R = \sqrt{(x-x')^2 + (y-y')^2 + (z-z')^2}. \tag{3.4}$$

If we define

$$K(z,z') = \frac{1}{j\omega\epsilon_o}\int_{-L/2}^{L/2}\left[\frac{\delta^2\psi(z,z')}{\delta z^2} + \beta^2\psi(z,z')\right]dz', \tag{3.5}$$

then it is clear that Equation (3.2) is in the same form shown in Equation (3.1). This is known as an integral equation of the first kind because the unknown $I(z')$ appears only under the integral.

3.1.2 Integral Equations and Kirchhoff's Network Equations

As stated earlier, the purpose of the moment method is to reduce the integral equation into a system of linear algebraic equations in terms of the unknown current $I(z')$. We can show that the Equation 3.2 is very similar to Kirchhoff's network equations given by

$$\sum_{n=1}^{N} Z_{mn} I_n = V_m, m = 1, 2, 3, \ldots, N. \tag{3.6}$$

so we can thus solve the integral equation using N equations and N unknowns. We will assume that the current is approximated by a *series of expansion functions* F_n such that

$$I(z') = \sum_{n=1}^{N} I_n F_N(z') \tag{3.7}$$

where the I_n's are complex expansion coefficients. For simplicity, the expansion functions will be a set of orthogonal pulse functions given by

$$F_n(z') = \begin{cases} 1 & \text{for } z' \text{ in } \Delta z'_n \\ 0 & \text{otherwise.} \end{cases} \tag{3.8}$$

This function produces a "staircase" approximation to the current distribution, where the wire is divided into N segments of length $\Delta z'_n$, as shown in Figure 3.2.

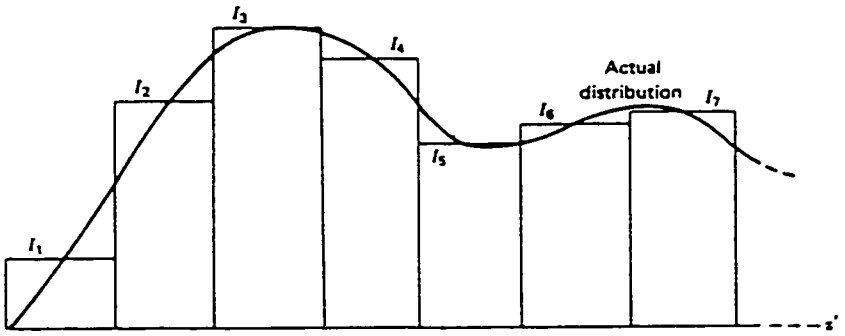

Figure 3.2: "Staircase" approximation to an actual current distribution[31].

We can substitute Equation (3.7) into Equation (3.1) to obtain

$$\int_{-L/2}^{L/2} \sum_{n=1}^{N} I_n F_n(z') K(z_m, z') dz' \approx -E_z^i(z_m) \tag{3.9}$$

where the subscript m on z_m indicates the integral equation is being enforced at segment m. The relationship is now only approximated because we have used an approximate current distribution. Now, by substituting Equation (3.8) into Equation (3.9), we can write

$$\sum_{n=1}^{N} I_n \int_{\Delta z'_n} K(z_m, z')dz' \approx -E_z^i(z_m). \tag{3.10}$$

If we now define

$$f(z_m, z'_n) = \int_{\Delta z'_n} K(z_m, z')dz', \tag{3.11}$$

and then combining the result, we get

$$\int_{-L/2}^{L/2} I(z')K(z_m, z')dz' \approx I_1 f(z_m, z'_1) + I_2 f(z_m, z'_2) + \ldots + I_N f(z_m, z'_N) \approx -E_z^i(z_m), \tag{3.12}$$

as illustrated by Figure 3.2. We have divided the wire into N equal length segments with $\Delta z'_n = \Delta z'$. Each segment has an unknown current, and at the center of any segment, the sum of the scattered fields of all N segments is set equal to the negative incident field at that point. From the boundary condition of a perfect conductor, $E_{inc} + E_{scat} = 0$, we know that the incident field is from either a source located on a wire, (i.e. transmitting example), or from a source located far away, as in a receiving or radar scattering case.

Finally, by defining $Z_{mn} = f(z_m, z'_n)$ and $V_m = -E_z^i(z_m)$, we obtain

$$\sum_{n=1}^{N} Z_{mn} I_n = V_m, \tag{3.13}$$

Point Matching

We have one equation with N unknowns, but we now repeat this process at different points z_m to obtain the additional equations. This process is called *point matching*, a special case of the more general method of moments. The following system of equations results from point matching at N points:

$$
\begin{aligned}
I_1 f(z_1, z_1') + I_2 f(z_1, z_2') + \ldots + I_N f(z_1, z_N') &= -E_z^i(z_1) \\
I_1 f(z_2, z_1') + I_2 f(z_2, z_2') + \ldots + I_N f(z_2, z_N') &= -E_z^i(z_2) \\
I_1 f(z_3, z_1') + I_2 f(z_3, z_2') + \ldots + I_N f(z_3, z_N') &= -E_z^i(z_3) \\
&\vdots \\
I_1 f(z_N, z_1') + I_2 f(z_N, z_2') + \ldots + I_N f(z_N, z_N') &= -E_z^i(z_N)
\end{aligned}
\tag{3.14}
$$

In compact matrix form, this can be written as

$$[Z_{mn}][I_n] = [V_m] \tag{3.15}$$

where $[Z_{mn}]$, $[I_n]$, and $[V_m]$ are referred to as the generalized impedance, current and voltage matrices, respectively. The solution to

$$[I_n] = [Z_{mn}]^{-1}[V_m] \tag{3.16}$$

can now be solved using a standard matrix reduction algorithm. Once the $[I_n]$ terms are solved, we can proceed to determine whatever antenna characteristics that are needed.

3.1.3 Numerical Electromagnetics Code (NEC)

The NEC code is a computer program that calculates the currents flowing on wire-grid models of various structures, and subsequently calculates the electric and magnetic fields resulting from those currents. Wire-grid modelling will be described in Chapter 4. NEC finds the currents in the wire structure by solving Pocklington's Integral Equation using the method of moments. The expansion function used by NEC is in the following form:

$$f(z') = a + b\cos(\beta z') + c\sin(\beta z'), \tag{3.17}$$

and uses the point-matching approach.

Input Format

The input for NEC code is composed of various command lines, called cards, which contain comments, geometry information, frequency, and the desired output. The exact format is very structured, but general descriptions of the important commands are as follows:

CM	Comment card.
GW	Geometry card, containing a tag number, starting and ending point, and the wire radius.
FR	Frequency of the desired evaluation.
NE,NH	Near E or H field evaluation at a specific point.
RP	Radiation pattern evaluated at a specific θ and ϕ. Automatic incrementation is an option.
EN	End of input file.

A sample of a NEC input file can be found in Appendix B.

3.1.4 Weighted Residuals and the Moment Method

In this section, an approach known as the method of weighted residuals will be introduced, a procedure more general than the point matching moment method. We will define the *residual* R to be the sum of the tangential components of the scattered and incident fields,

$$R = E_{tan}^{scat} + E_{tan}^{inc}. \tag{3.18}$$

In the previous example using the pulse expansion functions (Equation (3.8)), we can see that the current distribution used is true only at the matched points, i.e. at the center of each wire segment. In that case, the residual is found from Equation (3.9) to be

$$R(z) = \sum_{n=1}^{N} i_n f(z, z_n') + E_z^i(z). \tag{3.19}$$

When Equation (3.19) is evaluated at $z = z_m$, the residual at that given matched point will be zero since the solution for I_n was obtained using the electric field boundary condition. This is not the case at other points along that segment, as indicated by Figure 3.3, where the total tangential field will not be zero, and therefore the residual will not be zero for $z \neq z_m$, m=1, 2, 3, ..., N.

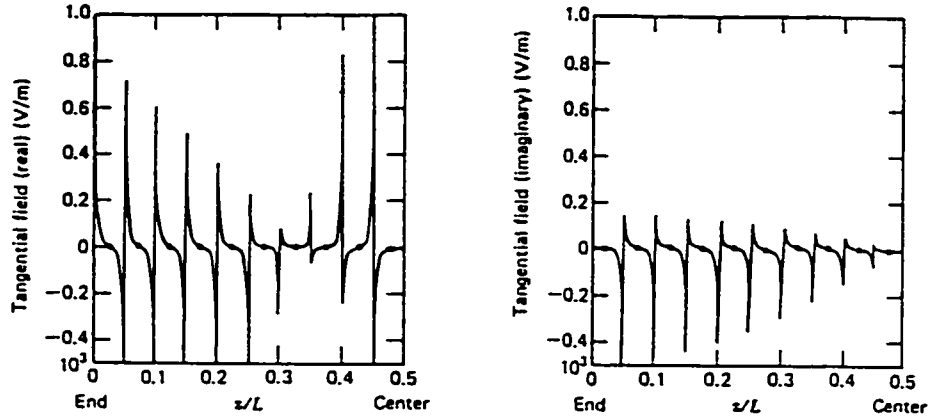

Figure 3.3: Normalized tangential electric field along one-half of a center-fed dipole with pulse expansion functions and delta weighting functions. Dots indicate match point locations[31].

Outside of the specified points, the boundary condition is being relaxed, and we hope that the condition is not violated so badly that its solution is rendered worthless. To improve the solution, we can increase the value of N within reasonable limits. Figure 3.4 illustrates the convergence of input impedance as the number N is increased.

The method of weighted residuals calculates the I_n's currents by forcing the average of the residual to be set to zero as follows:

$$\int W_m(z) R(z) dz = 0, \text{m=1,2,3,...,N} \tag{3.20}$$

where $W_m(z)$ is called the *weighting* function. By substituting Equation (3.19) into Equation (3.20), we obtain

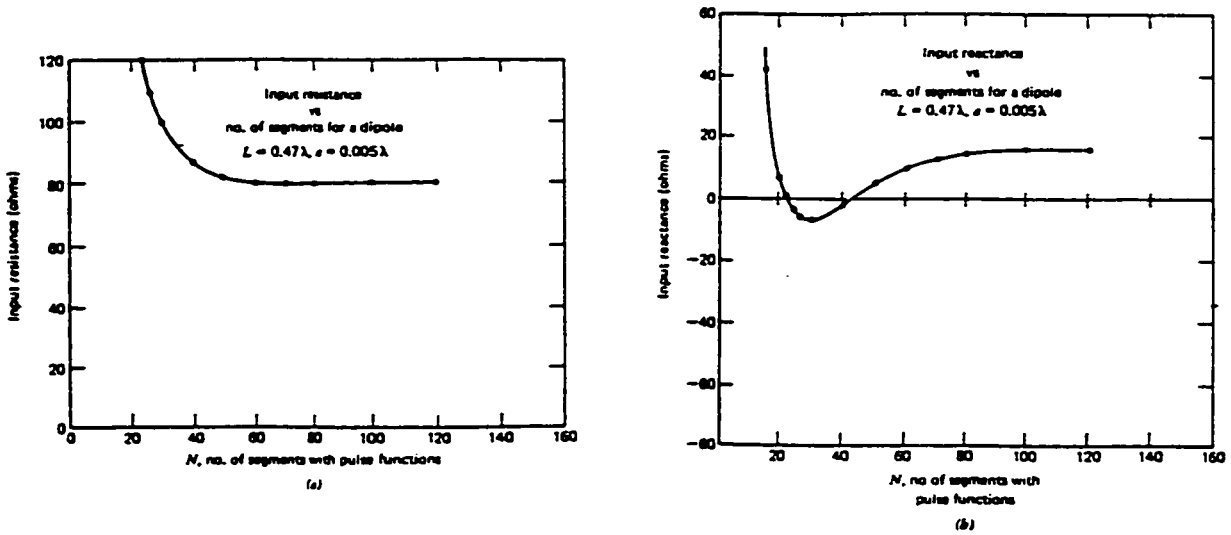

Figure 3.4: Input impedance as a function of number of pulse functions: a) Input resistance, b) input reactance[31].

$$\int_{-L/2}^{L/2} W_m(z) \sum_{n=1}^{N} I_n f(z,z')dz + \int_{-L/2}^{L/2} W_m(z) E_z^i(z)dz = 0, \tag{3.21}$$

If Dirac delta functions are chosen for the weighting functions, then Equation (3.21) reduces to the point matching solution in Equation (3.12).

Galerkin's Method

The choice of the expansion function and the weighting function should reflect the anticipated form of the current of the wire. When the expansion function is the same as the weighting function, the procedure is often referred to as *Galerkin's method.*

The final step is again to relate these quantities to Kirchhoff's network equations. It can be shown that if we denote the scattered field from the n^{th} expansion function of the current by $\mathbf{E_n}^s(\ell)$, then the general mn^{th} element in the generalized impedance matrix will be

$$Z_{mn} = \int_{-\ell/2}^{\ell/2} \mathbf{W_m}(\ell) \cdot \mathbf{E_n}^s(\ell)d\ell, \tag{3.22}$$

and the m^{th} generalized voltage matrix will be

$$V_m = -\int_{-\ell/2}^{\ell/2} \mathbf{W_m}(\ell) \cdot \mathbf{E}^i(\ell)d\ell \tag{3.23}$$

where $\mathbf{W_m}(\ell)$ is the m^{th} weighting function to be located on the axis of the wire, instead of on the wire surface. This is a mathematical simplification that essentially modifies the electric field boundary condition. When doing this, it is best to restrict wires to a radius of less than 0.01λ [31], which is sufficient for most wire antenna and scattering problems.

3.1.5 Multiradius Bridge Currents (MBC)

The MBC code is an extension of the original thin-wire code by Richmond. MBC is a Galerkin method solution using piece-wise sinusoids (PWS), one of the most useful functions for thin wire problems. For z-directed segments, the PWS can be expressed by

$$\mathbf{F}_n(z) = \hat{\mathbf{z}}\frac{\sin\beta(z - z_{n-1})}{\sin\beta(z_n - z_{n-1})}, z_{n-1} \leq z < z_n \tag{3.24}$$

$$\mathbf{F}_n(z) = \hat{\mathbf{z}}\frac{\sin\beta(z_{n+1} - z)}{\sin\beta(z_{n+1} - z_n)}, z_n \leq z < z_{n+1}. \tag{3.25}$$

The PWS is illustrated in Figure 3.5, along with overlapping PWSs.

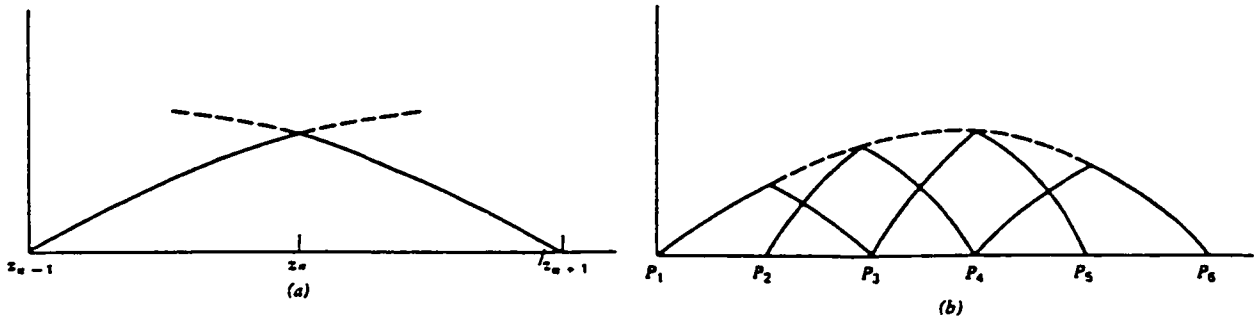

Figure 3.5: a) Piecewise sinusoidal expansion function, b) Overlapping piecewise sinusoidal functions[31].

Input Format

The input format for the MBC code is very cryptic and user unfriendly. It requires the same type of parameters as the NEC code, and a commented printout of sample program is included in Appendix C.

3.1.6 Surface Patch Implementation

This section introduces the formulation of the *Patch* code developed by Rao *et al.*[11].

An incident electric field $\mathbf{E^i}$ incident on an arbitrary perfectly conducting surface S induces surface currents $\mathbf{J_S}$. The scattered electric field $\mathbf{E^s}$ can be computed from

$$\mathbf{E^s} = -j\omega\mathbf{A} - \nabla\mathbf{\Phi} \tag{3.26}$$

with the magnetic vector potential defined as

$$\mathbf{A(r)} = \frac{\mu}{4\pi}\int_S J\frac{e^{-jkR}}{R}dS' \tag{3.27}$$

and the scalar potential as

$$\mathbf{\Phi(r)} = \frac{1}{4\pi\epsilon}\int_S \sigma\frac{e^{-jkR}}{R}dS'. \tag{3.28}$$

with the surface charge density σ related to the current by the continuity equation[11]

$$\nabla \cdot \mathbf{J}_S = -j\omega\sigma_S. \tag{3.29}$$

Enforcing the boundary condition $\hat{n} \times (E^i + E^s) = 0$ on the surface S results with the integral equation

$$-\mathbf{E^i_{tan}} = -(j\omega\mathbf{A} - \nabla\mathbf{\Phi})_{\mathbf{tan}}. \tag{3.30}$$

Basis Function

Having assumed that triangular patches have appropriately represented the surface with respect to edges, faces and boundaries, Rao *et al.*[11] defined the vector basis function as Equation 3.31 associated with the common (i.e. nonboundary) edge of two triangle patches, shown in Figure 3.6.

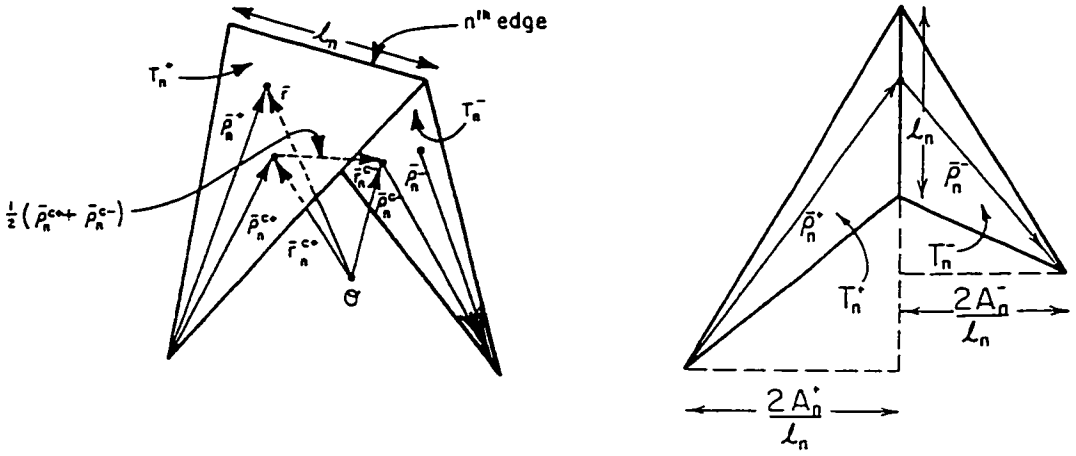

Figure 3.6: Triangular pair and geometrical parameters for patch basis function[11].

The triangle designations T_n^+ and T_n^-, each of area A_n^+ and A_n^- respectively, are determined by the assumed current direction across the nth edge of length ℓ_n, i.e. from T_n^+ to T_n^-. The position vectors ρ_n^+ in T_n^+ are defined with respect to the free vertex of T_n^+, while ρ_n^- are directed towards the free vertex of T_n^-, and r is the position vector defined with respect to the origin. The vector basis function associated with the nth edge is defined as

$$f_n(r) = \begin{cases} \frac{\ell_n}{2A_n^+}\rho_n^+ & \text{for } r \text{ in } T_n^+ \\ \frac{\ell_n}{2A_n^-}\rho_n^- & \text{for } r \text{ in } T_n^- \\ 0 & \text{otherwise.} \end{cases} \tag{3.31}$$

Some of the properties of the basis function f_n, used as an approximation of the surface current, include

1. There is no current component normal to the surface formed by T_n^+ and T_n^- so there is no line charges along the nth edge.

2. The current components normal to the nth edge are constant and continuous across the edge.

3. The surface divergence of f_n is

$$\nabla \cdot f_n(r) = \begin{cases} \frac{\ell_n}{A_n^+} & \text{for } r \text{ in } T_n^+ \\ \frac{\ell_n}{A_n^-} & \text{for } r \text{ in } T_n^- \\ 0 & \text{otherwise} \end{cases} \tag{3.32}$$

and is thus constant for each triangle

3.1.7 Junction patch code

The code Junction[52] was developed by Hwu and Wilton, the latter being a co-author of the original *Patch* code introduced earlier. Junction employed the same surface patch implementation as in Patch and incorporated wire grid modelling. In this report, only the patch modelling approach of Junction is employed.

The input format required for Junction requires the definition of vertices as x, y and z coordinates. These points are subsequently used to define the edges used to make up the triangular patches. Also included in the input file is the definition of field points and other control parameters such as frequency. A printout of the plate input file is included in Appendix D.

3.1.8 Summary

This section has described the point-matching and Galerkin implementation of the moment method. As an illustration of their difference, Figure 3.7 shows the electric field on the conducting surface of a $\lambda/2$ dipole solved using (a) pulse point-matching and (b) Galerkin's piece-wise sinusoids.

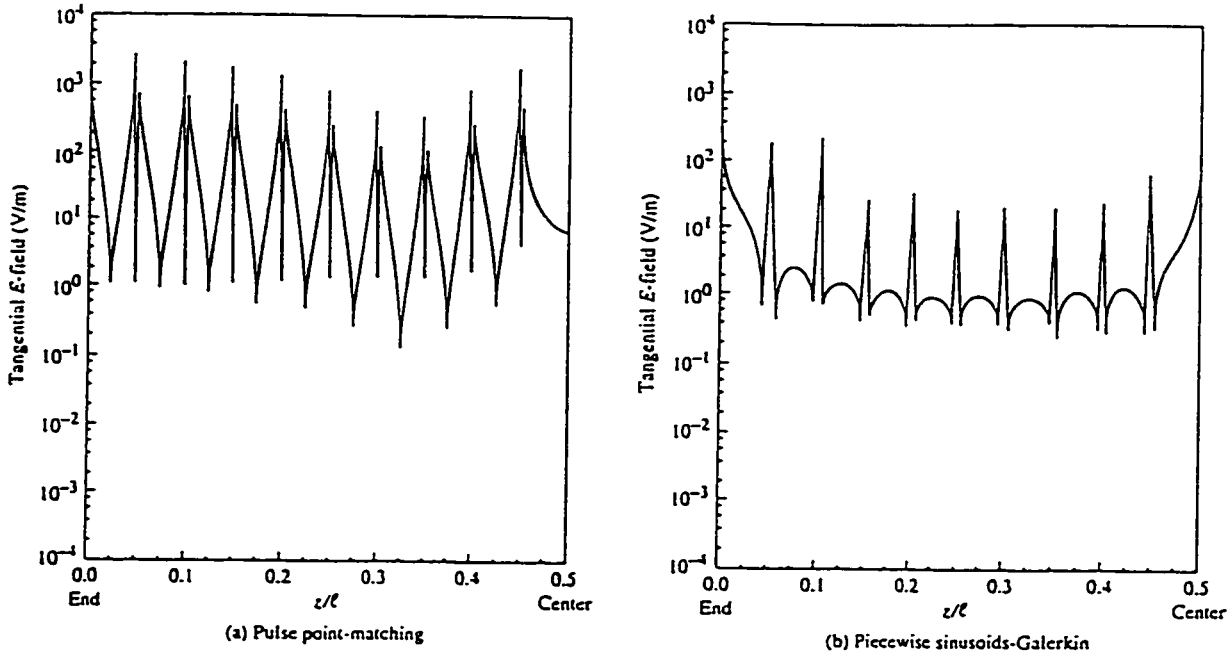

Figure 3.7: Tangential electric field on the conducting surface of a $\lambda/2$ dipole. a) Pulse point-matching, b) Piecewise sinusoids-Galerkin[32].

We have seen in this section that the method of moments makes it possible to reduce an integral equation into a system of linear equations. When we deal with very complex models, we can see why computing power is needed. If we consider a model with 500 wire segments, the [Z] matrix becomes 500 by 500 elements, where each element is comprised of another integral, as symbolized by $f(z_m, z'_n)$ in Equation (3.11).

In order for NEC or MBC to perform as accurately as possible, the wire-grid model must conform to several rules. The integrity of the model is extremely important since meaningful results can only be obtained from models representing the true surface as accurately as possible. The next chapter outlines the important rules to observe, as well as software designed to aid in the proper construction of wire-grid models.

3.2 Wire-Grid Modelling

Wire-grid modelling was first introduced in 1966 by Richmond[3]. The model's construction should follow the geometrical and electrical characteristics of the original structure as closely as possible. Using this technique, grid models can be constructed to represent surfaces of highly complex structures including aircraft and naval vessels.

Geometrically, the wire segments should follow the surfaces of the original structure. The most important electrical consideration is the relationship between the segment length (Δ) and the wavelength (λ)[33].

There are many rules, called modelling guidelines, that must be followed to produce accurate models. The modelling guidelines arise from two sources: The assumptions in the derivation of the EFIE and the limitations of dimensions of segment lengths and radii[34]. The most important guidelines shall be outlined in this chapter.

Note that the guidelines presented in this section are a result of much analysis and scrutiny on the program NEC. There are very few guidelines available for MBC. The original program "thin-wire" by Richmond[3], on which MBC was developed, documents very few modelling rules. The report assumes that "$a \ll \lambda$," "$\Delta \gg a$," and that the "longest wire segment should not greatly exceed $\lambda/4$"[42]. For this reason, the NEC guidelines shall be applied for the MBC models employed in this report.

3.2.1 Modelling Guidelines

Figure 3.8 illustrates the terms associated with wire geometry.

Segment length

In general, the segment length should be smaller than 0.1λ; however longer wires are acceptable where there are no abrupt geometrical changes. Shorter segments increase the solving resolution of NEC; however, very short segments ($\lambda/1000$) will

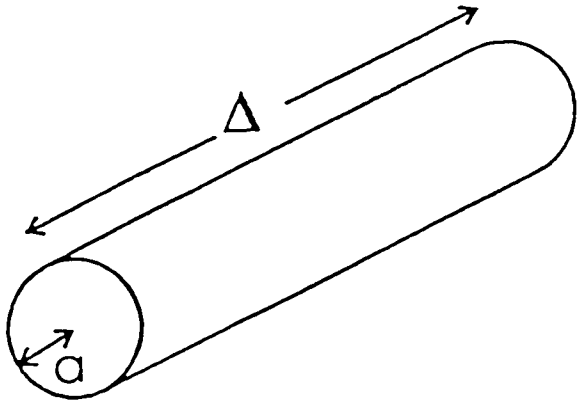

Figure 3.8: Wire segment with label definition.

produce numerical problems[35].

Wire radius

The currents are only considered in the axial direction on a segment. This is considered to be accurate unless $2\pi a/\lambda \ll 1$ or $ka \ll 1$. Segment length must be $\Delta/a > 8$ for errors less than 1%[36].

The wire radii "a" should be calculated so that the total surface of the wire segments is equal to the area of the surface being modeled. The relationship between the radius and the segment length can be determined using the adapted equal-area rule, derived by Trueman[37]. This method relates the areas of the meshes with the length and radius of their components, and is illustrated below in Figure 3.9.

In summary, the rule states that

$$area = \frac{A_1}{\pi L_{t1}} + \frac{A_2}{\pi L_{t2}} \tag{3.33}$$

where,

A_1 = area of mesh #1,
A_2 = area of mesh #2,
$L_{t1} = L_1 + L_2 + L_3 + \Delta$ =periphery of mesh #1,
$L_{t2} = L_4 + L_5 + L_6 + \Delta$ =periphery of mesh #2.

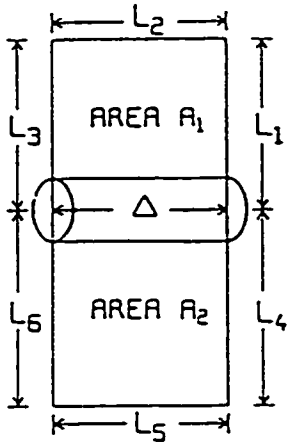

Figure 3.9: Adapted equal area rule[38].

Investigation of self-inductance by Lee et al. [39] found that respecting the same surface rule generated the most accurate results. Ludwig [40] examined 2-D TM polarized wire grid model of a cylinder and found that the far field was accurate when observing the same surface rule even though the tangential field is not accurate between the wires. Paknys [41] extended Ludwig's work by showing that the same surface rule produces the best near field results.

Wire connections

Wire connections occur when two or more wires have coincident endpoints. Segments are considered to be connected if their ends are separated by less than 1000 times the shortest segment length [43], however it is good practice to use identical points. The maximum number of connections to any one junction is 30 [44].

Summary of Modelling Guidelines

The modelling guidelines are shown in Table 3.1 and Table 3.2, outlining the main recommendations for successful model development. The preparation of a proper model entails a balancing of many criteria which are at times contradictory. For in-

stance, the best resolution is obtained by the use of the maximum number of segments, but numerical problems can arise, which limits the number of segments.

MODELLING PARAMETER	EXPECTED RANGE	JUSTIFICATION
Wire radius, a	Adapted equal area rule	To obtain the best accuracy
As related to wavelength, λ	$2\pi a/\lambda < 1$	Due to axial flow of current
Wire segment length, Δ as related to radius a	$\Delta/a \rangle 2$ (Thin-wire Kernel) $\Delta/a \rangle 0.5$ (Extended Thin-wire Kernel)	To avoid oscillation in the current value near voltage sources, lumped loads or free wire ends
As related to wavelength, λ	$\Delta \rangle \lambda/2\pi$	To sample current densely enough per unit wavelength
Angle of intersection of wires, α	Larger than any angle which causes overlapping	Avoid placing the observation point of one wire segment within the volume of another wire
Axial separation of wires, r_a	Several radii apart	Division of current between two overlapping segments is indeterminent
Maximum no. of wires at a junction, N_j	$N_j \langle 30$	Due to dimension limitation in NEC
Source location	Not on an open-ended segment	To avoid non physical situation of driving wire at open end

Table 3.1: Summary of guidelines for individual wires[56].

PARAMETER	TYPE OF DISCREPANCY	LIMIT
	JUNCTION DISCREPANCY	
Coincidence error	Error	Two coincident wires.
RAD/RAD	Warning Error	Longer/Shorter radius $\rangle$ 5.0 Longer/shorter radius $\rangle$ 10.0
Match point error	Error	Volume of one segment contains the centre of another.
SEG/SEG	Error	Longer /shorter segment $\rangle$ 5.0
SEG/RAD	Warning Error	2.0 $\langle$ SEG/RAD $\langle$ 8.0 2.0 $\rangle$ SEG/RAD.
	INDIVIDUAL DISCREPANCIES	
wire length	Error	Length $\langle$ 0.01 M.
SEG/RAD	Warning	2.0$\langle$SEG/RAD$\langle$8 0.5 $\langle$ SEG/RAD $\langle$ 2 EK option
	Error	SEG/RAD $\langle$ 2 SEG/RAD $\langle$ 0.5 EK option
SEG/λ	Note Warning Error	0.05 $\langle$ SEG/WAV $\langle$ 0.1 0.1 $\langle$ SEG/WAV $\langle$ 0.2 SEG/WAV $\rangle$ 0.2 OR $\langle$ 0.001
λ/RAD	Error	WAV/RAD $\langle$ 30

Table 3.2: Summary of guidelines at wire junctions[57].

3.2.2 Model Development Software

In order to ensure that the computational results generated by NEC or MBC are as accurate as possible, it is important that the wire-grid models adhere to the guidelines outlined in the previous section. Models that do not observe these guidelines may cause the code to calculate field and current flows that are not consistent with measurements. Neither code provides any mechanism to validate these modelling guidelines.

Over the years, computer programs have been developed to verify a model's adherence to the guidelines. This section will briefly describe some of the programs used for the evaluation of this report.

MODEL

The program MODEL generates a visual representation of the wire-grid model using a standard NEC input file. MODEL allows the user to display the model from any perspective, and provides a capacity to zoom in on a specific area on the display screen. The wires may be shown in a uniform "stick" form, or represented as cylinders to highlight the different wire radii[19]. Figure 3.10 shows some of the possible outputs.

MESHES and FNDRAD

The program MESHES scans a standard NEC input file for the meshes formed by the inter-connection of wires, and produces several output files containing the vertices and elements involved in each specific mesh. This output is used to find the radius of each wire.

The program FNDRAD (for FiND RADius) uses the area and size of each mesh and applies the adapted equal-area rule to find the wire radius of each segment[37].

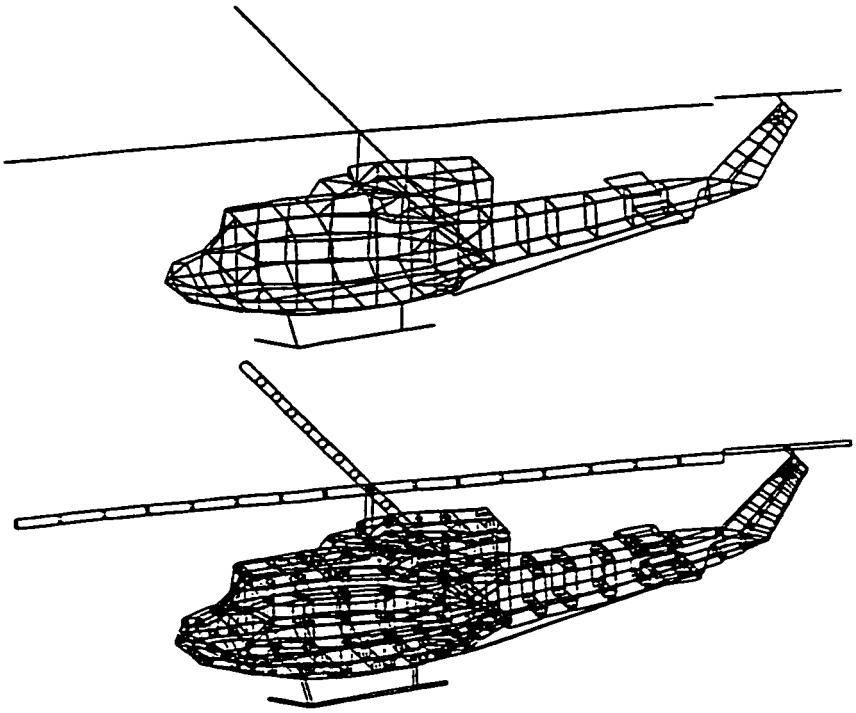

Figure 3.10: Output formats of the program MODEL.

HIDNMOD

The program HIDNMOD (for HIDdeN MODel) uses the mesh information from the output of the program MESHES and produces an image of the model that appears to be solid. An example of the complex helicopter model is shown in Figure 3.11.

CHECK

The program CHECK scans a standard NEC input file and scrutinizes the entire model for fundamental errors according to the modelling guidelines. CHECK's output contains different levels of advisories: Notes (N) for segments approaching the violation boundary, Warnings (W) for segments that violate the lower limit, and Errors (E) for serious breaches to the guidelines. CHECK also produces statistics pertaining to the number of wire segments, their average length, radius, etc[47].

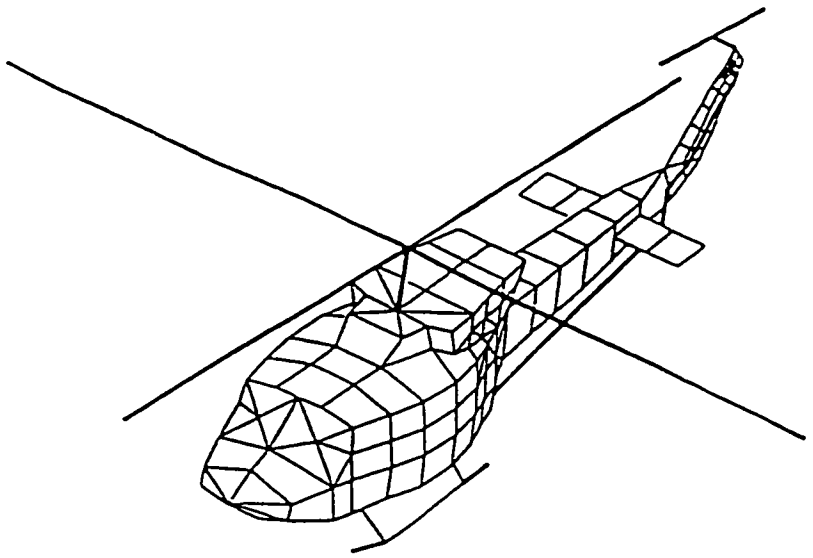

Figure 3.11: HIDNMOD representation of the helicopter model.

3.3 Software Utilities

3.3.1 Analysis Software

ISOLEV

The program ISOLEV (ISOtropic LEVel) computes the isotropic level of the radiating structure as defined in Chapter 2. The program also provides useful data, such as the maximum field strength, total radiated power and input resistance. To calculate these parameters, ISOLEV requires the radiation patterns based on the military standard specifications MIL-A-9080 and examined by [48, 49].Since the far-field disregards the $e^{j\beta r}/r$ term of the field calculation, the field may be considered to be normalized to the distance r, and evaluated at one metre in volts/metre.

PATCMP

The program PATCMP (for PATtern CoMParison) produces a polar plot of the radiation pattern, using the solution file created by ISOLEV. The fields can be plotted versus either phi or theta. The plot can be presented using either linear or decibel scales, and can display either polarization, E_θ or E_ϕ, or both simultaneously.

PATCMP also provides the user the option of displaying the model in the proper orientation, in the upper-left corner of the display[47].

IDIS

The program IDIS (I for current, DISplay) represents the current distribution throughout the wire segments in the model. There are a number of display options available. Currents can be presented in either linear or dB scales. Several display modes are available: rectangular axis, perpendicular-lines and spectrum formats.

The rectangular axis mode plots the current magnitude and phase on a rectangular axis as a function of distance along the current path. The perpendicular mode plots lines representing a function of the current magnitude perpendicular to the wire segments. The spectrum mode shows the current distribution coded with a hot colour scale. Arrows can be displayed to indicate the phase of the current along each segment. An example is shown in Figure 3.12

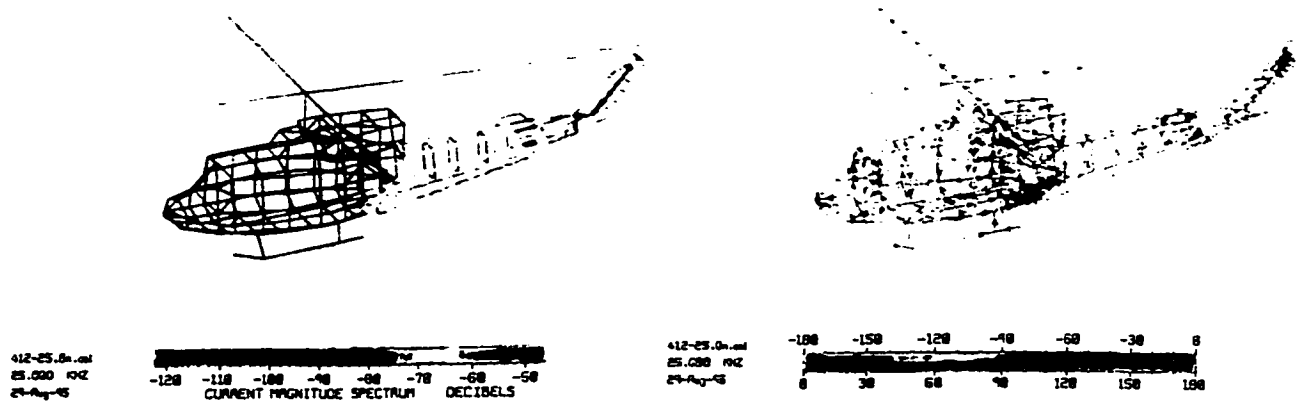

Figure 3.12: Example of IDIS outputs: a) spectrum scale (dB) b) phase scale.

The software is one of the most important tools in understanding the model's (and therefore the antenna's) efficiency. Radiation is produced by currents flowing, so this display program provides some of the best insight into antenna operation.

RPLOT

RPLOT is a general purpose rectangular plotting program. RPLOT uses a two column input file to produce the plots, and the scaling can be linear, log or dB. There is also an impedance scale which allows a representation of the antenna reactance, which would normally be difficult to represent in dB format due to the negative values[47].

3.3.2 Conversion Software

In order to take advantage of the existing model development software and analysis software packages describes in the previous sections, the following programs were written by Raschkowan as part of this thesis.

CONVert

The program CONVert is a utility to translate a NEC input file to the format required for MBC. The program includes the redefinition of the geometry, wire radius designation, desired output, frequency, and ground plane option. The geometry conversion has been substantially tested, and a graphical illustration is presented in Figure 3.13 showing the NEC input file for the complex helicopter using MODEL, and the "thin-wire viewer"[50] representation of the MBC file.

TRANslate

The program TRANslate converts the solution file from the MBC run and converts it into the NEC solution file format. This step was necessary in order to perform the side by side comparison using the analyzing software.

EXTRACt

The program EXTRACt was written to organize the data for the antenna parameters into the two column format needed for RPLOT. The program uncompresses each of

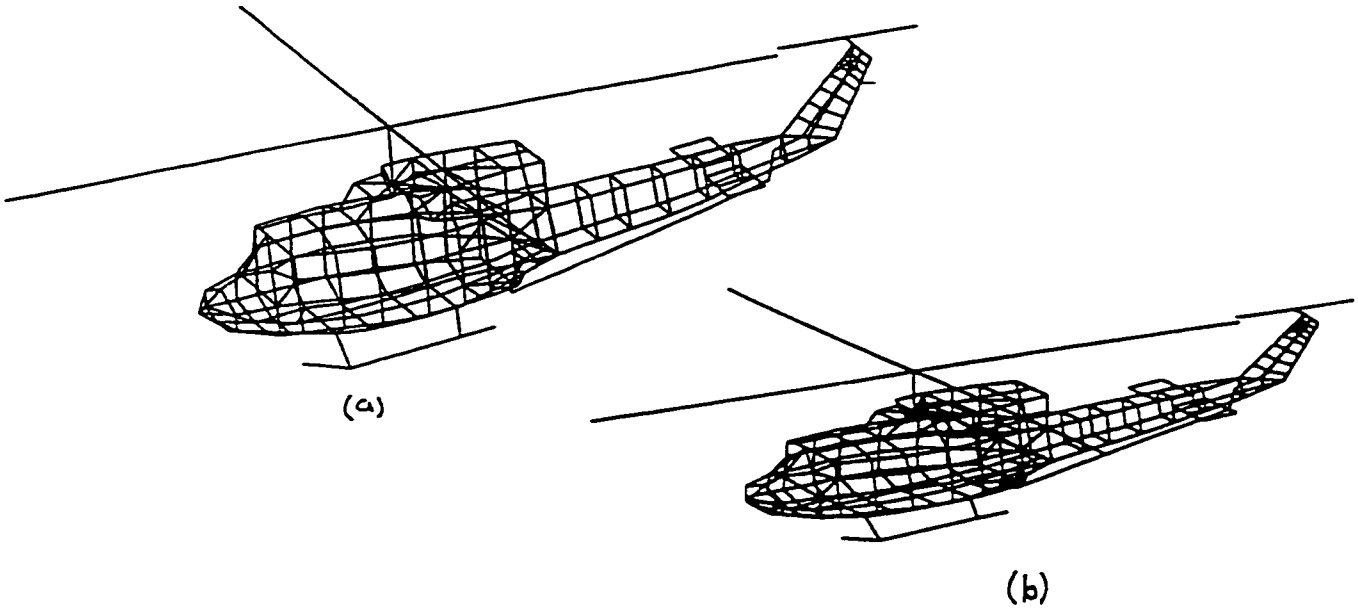

Figure 3.13: Model representation using a) MODEL for NEC and b) thin-wire viewer for MBC.

the solution files (one per frequency) obtained in the frequency sweep. reads the parameters of the maximum field strength, isotropic level, impedance, etc, writes these parameters to individual files ready for RPLOT, and then recompresses the solution file.

The compression of the files is necessary because of the large number (281) of solution files produced per model when carrying out the frequency sweep of the helicopter models, and the large amount of data in each file.

Chapter 4

Near Field Experiments

There has been much research assessing the validity of wire grid modelling performed on the far field calculations but relatively little investigating the near field.

Much of the work in this section was reported in [51], attached in Appendix A.

4.1 Near Field Scattering of a Square Plate

This section investigates the near-field calculations generated by both NEC and MBC of a plane wave incident upon a 1-metre square wire-grid plate, as depicted in Figure 4.1.

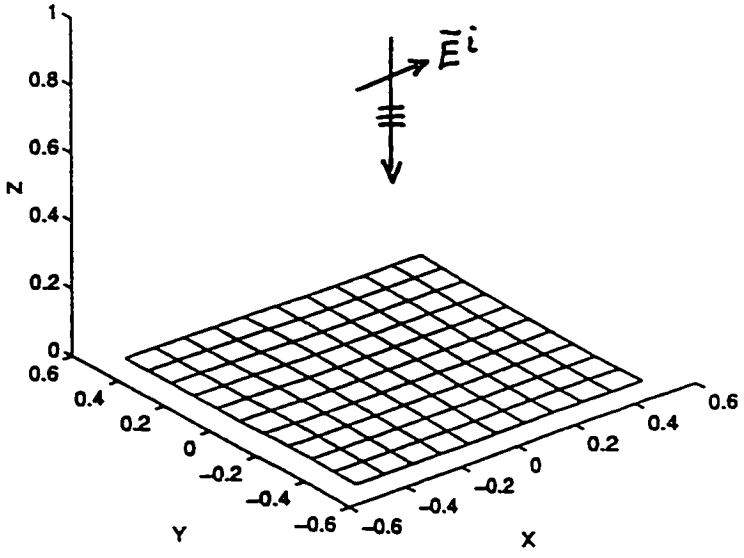

Figure 4.1: Plane wave incident upon 1x1 metre plate.[51]

There is no exact solution for the scattering by a plate. A surface patch model of the plate is evaluated using the Moment Method patch code *Junction* [52] as a comparison. The validation for employing the Junction code as a benchmark for the plate is included in [51] where Junction was compared to the UTD based BSC (Basic Scattering Code)[53] to establish confidence in the patch model.

The 1-metre square plate lies in the x - y plane with the origin at the center of the plate. The calculations are performed at a frequency of 300 MHz. The incident field is $\mathbf{E}^{\mathbf{inc}} = \hat{x}e^{jkz}$, an $\hat{x}$-polarized plane wave with an amplitude of 1 V/m travelling in the $-z$ direction.

The wire grid model evaluated was created with a grid size of $g = 0.1\lambda$. Field points are selected at different heights h above the plate. The relationship between g/h is examined.

In a separate experiment, an examination of the same surface rule is performed by varying the wire radii of the models and comparing the results to the *Junction* solution.

4.1.1 Grid to Height Evaluations

Field points were selected at various heights just above and just below the surface of the plate. Heights of $g/z = \pm 1.25$ and $g/z = \pm 2.5$, were selected. Note that the *lit side* are positive heights and the *shadow side* are negative heights. The total field $\mathbf{E} = \mathbf{E}^{\mathbf{inc}} + \mathbf{E}^{\mathbf{scatt}}$ was plotted, using a reference level of 0 dB = 1 V/m.

Results and Discussion

The results of the tangential E_x field at $g/z = \pm 2.5$ and $g/z = \pm 1.25$ are shown in Figure 4.2.

The results show that anomalies occur in the E_x field as the distance approaches $g/h = 2.5$ on the lit side of the plate, however the anomalies are significant at $g/h = 2.5$ in the shadow, and only subside as the distance increases toward $g/h = 1.25$.

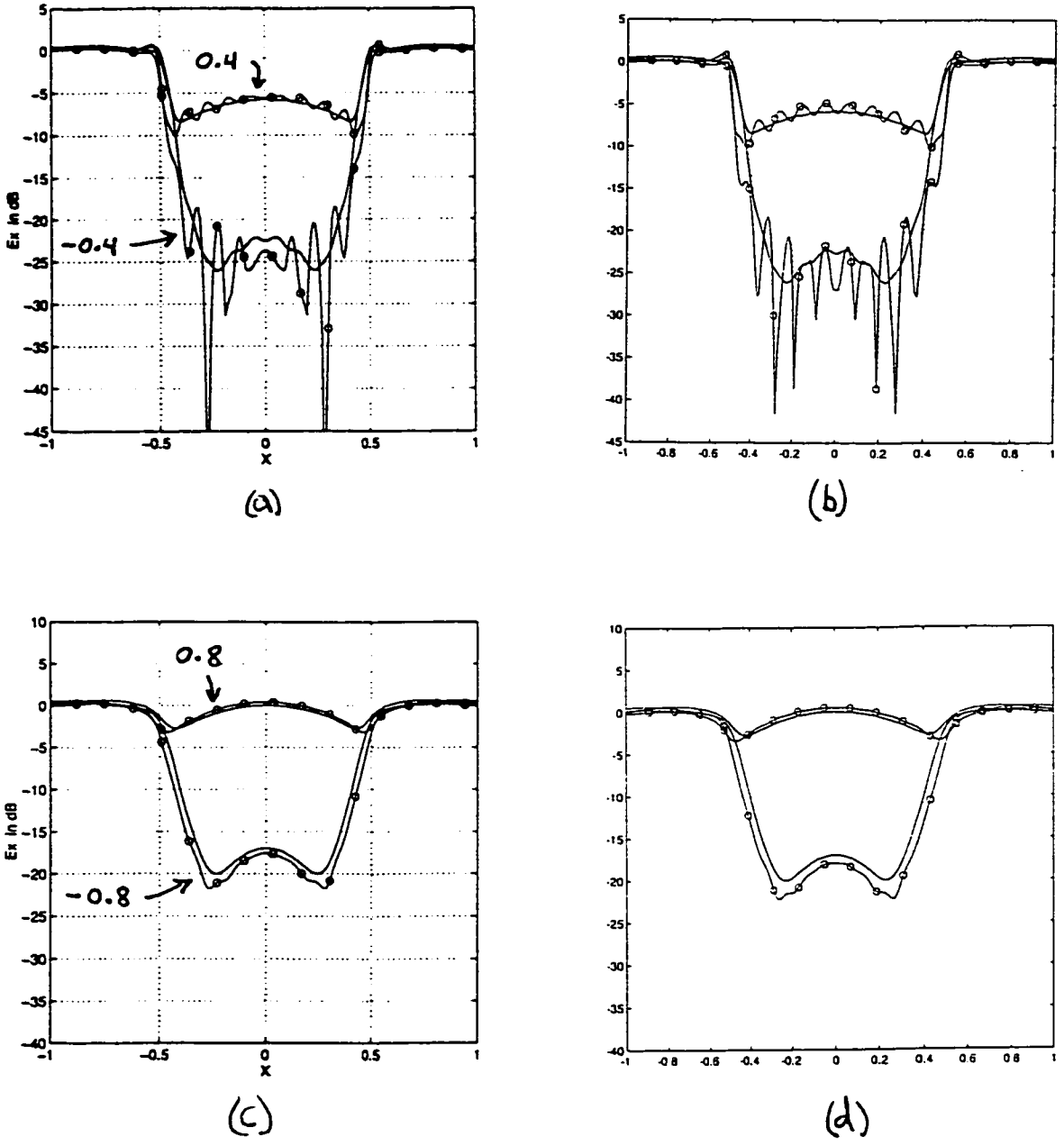

Figure 4.2: E_x field of the 0.1λ grid square plate (a) Junction (—) and NEC (ooo) at $h = \pm 0.04$m (b) Junction (—) and MBC (ooo) at $h = \pm 0.04$m (c) Junction (—) and NEC (ooo) at $h = \pm 0.08$m (d) Junction (—) and MBC (ooo) at $h = \pm 0.08$m

The results of the Normal E_z field at $g/z = 2.5$ and $g/z = 1.25$ are shown in Figure 4.3. Note that only the *lit side* is shown since the E_z field is the same above and below the plate.

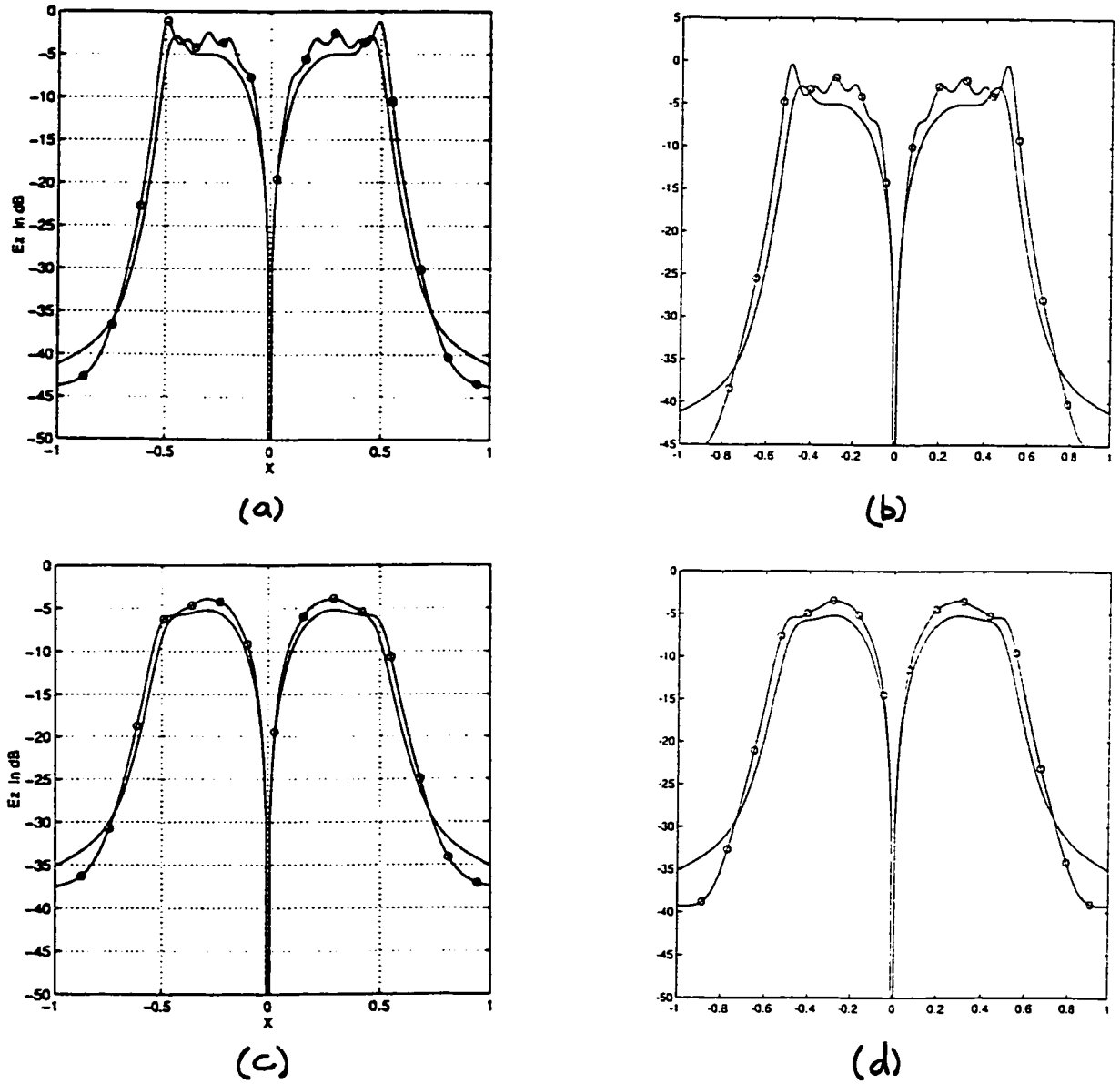

Figure 4.3: E_z field of the 0.1λ grid square plate (a) Junction (—) and NEC (ooo) at $h = 0.04$m (b) Junction (—) and MBC (ooo) at $h = 0.04$m (c) Junction (—) and NEC (ooo) at $h = 0.08$m (d) Junction (—) and MBC (ooo) at $h = 0.08$m

The anomalies in the E_z field shown in Figure 4.3 at $g/h = 2.5$ are the same magnitude as those seen in the results for E_x.

4.1.2 Same Surface Rule Evaluations

The wire-grid modelling guidelines outlined in Section 3.2 indicate that the total surface area of the wire-grid model should equal the surface area of the object under investigation to yield the best results. In this section, comparisons are performed by varying the wire radii of the plate and observing the results.

As in the previous section, a frequency of 300 MHz was used. The height above and below the plate are $g/h = \pm 1.25$ in order to be as close to the surface as possible without having the anomalies interfere with the results.

Results and Discussion

The results of the tangential E_x field at $g/z = \pm 1.25$ are shown in Figure 4.4.

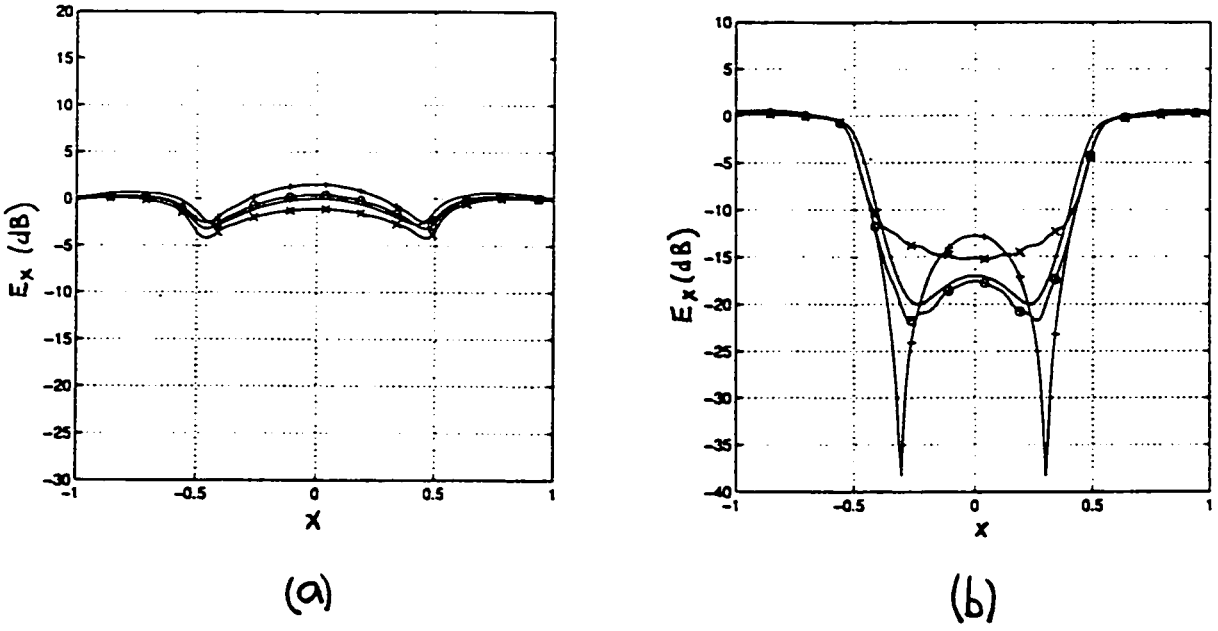

Figure 4.4: Wire radii variations to E_x field of the 0.1λ grid square plate. Comparison between *Junction* (—), and NEC result with a_w (ooo), $\frac{a_w}{2}$ (+++) and $2a_w$ (xxx). (a) $h = 0.08$m and (b) $h = -0.08$m.

The results in Figure 4.4 show that adhering to the same surface rule produces

the best results for the E_x field. The results show that the E_x field in the shadow is more sensitive to wire radius changes than on the lit side of the plate.

The results of the Normal E_z field at $g/z = 1.25$ are shown in Figure 4.5.

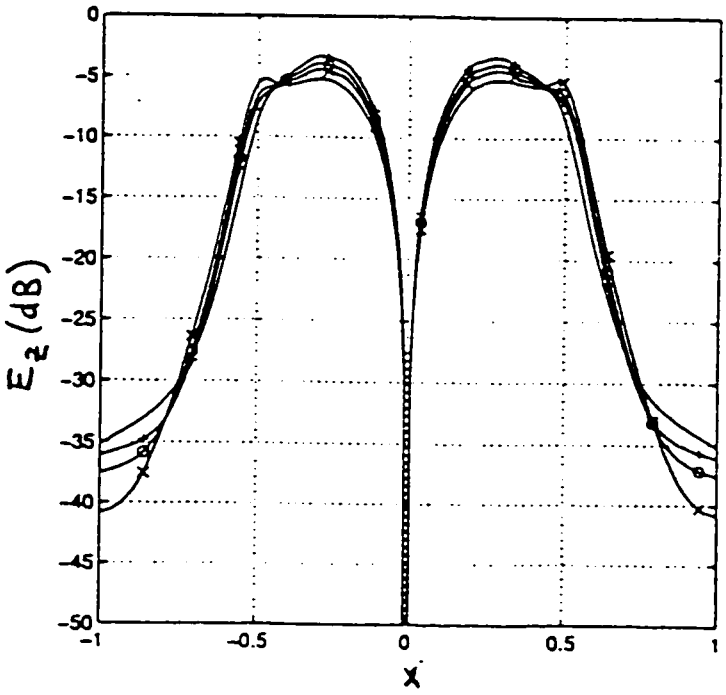

Figure 4.5: Wire radii variations to E_z field of the 0.1λ grid square plate. Comparison between *Junction* (—), and NEC result with a_w (ooo), $\frac{a_w}{2}$ (+++) and $2a_w$ (xxx) at height $h = 0.08$m.[51]

The results of the E_z field indicate that the best results to not occur when the same surface rule is followed. It appears that the same surface rule can not provide the optimum solution for both tangential and normal fields simultaneously[51]. It appears as well from the results that the E_x field is more sensitive to the variations of wire radius than the E_z field.

4.2 Near Field Scattering of a Sphere

This section demonstrates the accuracy and reliability of the moment method in solving near field scattering problems. The results from the two codes will be compared to the exact solution to verify the validity of the calculated solutions. This will also be another example to examine if the Galerkin method is superior to the point matching method.

The near field scattering of a plane wave incident on a 15 metre radius perfectly conducting sphere is used to evaluate the performance of the two codes compared to the exact solution of the problem. Consider the illustration presented in Figure 4.6.

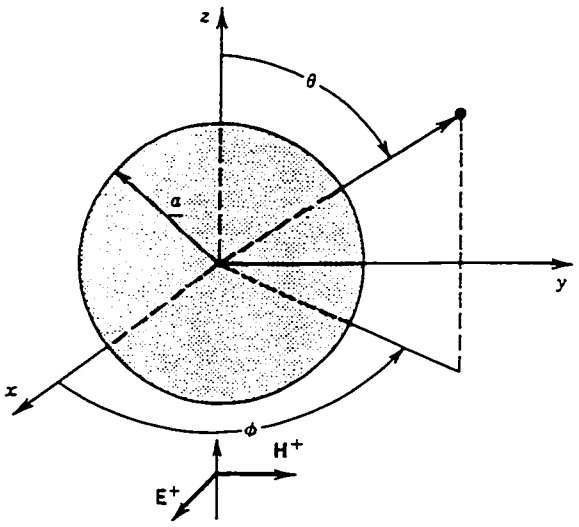

Figure 4.6: Uniform plane wave incident on a conducting sphere[54].

4.2.1 Exact Solution

The exact solution for the scattering of a sphere is available in many texts including Harrington[55] and Balanis[56]. The incident wave is x-polarized and z-traveling, i.e.

$$E_x^i = E_0 e^{-jkz} = E_0 e^{-jkr\cos\theta} \tag{4.1}$$

and

$$H_y^i = \frac{E_0}{\eta} e^{-jkz} = \frac{E_0}{\eta} e^{-jkr\cos\theta}. \tag{4.2}$$

The scattered field can be expressed using the following potentials:

$$A_r^s = \frac{E_0}{\omega\mu}\cos\phi \sum_{n=1}^{\infty} b_n \hat{H}_n^{(2)}(kr) P_n^1(\cos\theta) \tag{4.3}$$

and

$$F_r^s = \frac{E_0}{k}\sin\phi \sum_{n=1}^{\infty} c_n \hat{H}_n^{(2)}(kr) P_n^1(\cos\theta). \tag{4.4}$$

The total field can be expressed using the following:

$$A_r^t = \frac{E_0}{\omega\mu}\cos\phi \sum_{n=1}^{\infty} \left[a_n \hat{J}_n(kr) + b_n \hat{H}_n^{(2)}(kr)\right] P_n^1(\cos\theta) \tag{4.5}$$

and

$$F_r^t = \frac{E_0}{k}\sin\phi \sum_{n=1}^{\infty} \left[a_n \hat{J}_n(kr) + c_n \hat{H}_n^{(2)}(kr)\right] P_n^1(\cos\theta), \tag{4.6}$$

where the boundary conditions are $E_\theta = E_\phi = 0$ at $r = a$ requiring

$$a_n = \frac{j^{-n}(2n+1)}{n(n+1)}, \tag{4.7}$$

$$b_n = -a_n \frac{\hat{J}_n'(ka)}{\hat{H}_n^{(2)\prime}(ka)}, \tag{4.8}$$

$$c_n = -a_n \frac{\hat{J}_n(ka)}{\hat{H}_n^{(2)}(ka)}. \tag{4.9}$$

The **E** and **H** are then determined using the relationships in equations (4.10) through (4.15) from [57]:

$$E_r = \frac{1}{\hat{y}}\left(\frac{\partial^2}{\partial r^2} + k^2\right) A_r \tag{4.10}$$

$$E_\theta = \frac{-1}{r\sin\theta}\frac{\partial F_r}{\partial\phi} + \frac{1}{\hat{y}r}\frac{\partial^2 A_r}{\partial r\partial\theta} \tag{4.11}$$

$$E_\phi = \frac{1}{r}\frac{F_r}{\partial\theta} + \frac{1}{\hat{y}r\sin\theta}\frac{\partial^2 A_r}{\partial r\partial\phi} \tag{4.12}$$

$$H_r = \frac{1}{\hat{z}}\left(\frac{\partial^2}{\partial r^2} + k^2\right) F_r \tag{4.13}$$

$$H_\theta = \frac{1}{r\sin\theta}\frac{\partial A_r}{\partial \phi} + \frac{1}{\hat{z}r}\frac{\partial^2 F_r}{\partial r \partial \theta} \tag{4.14}$$

$$H_\phi = -\frac{1}{r}\frac{A_r}{\partial \theta} + \frac{1}{\hat{z}r\sin\theta}\frac{\partial^2 F_r}{\partial r \partial \phi}. \tag{4.15}$$

The resulting total electric and magnetic fields of a plane-wave incident on the sphere are the following:

$$\mathbf{E}_r^t = \frac{E_0 \cos\phi \sin\theta}{j(kr)^2} \sum_{n=1}^{\infty} n(n+1)\left[a_n \hat{J}_n(kr) + b_n \hat{H}_n^{(2)}(kr)\right] P_n^1(\cos\theta) \tag{4.16}$$

$$\begin{aligned}\mathbf{E}_\theta^t = {} & \frac{E_0 \cos\phi}{kr}\left(-\sum_{n=1}^{\infty}\left[a_n \hat{J}_n(kr) + c_n \hat{H}_n^{(2)}(kr)\right] P_n^1(\cos\theta)\right) \\ & + \frac{E_0 \cos\phi}{jkr}\left(\sum_{n=1}^{\infty}\left[a_n \hat{J}_n'(kr) + b_n \hat{H}_n^{(2)\prime}(kr)\right] P_n^{1\prime}(\cos\theta)\right)\end{aligned} \tag{4.17}$$

$$\begin{aligned}\mathbf{E}_\phi^t = {} & \frac{E_0}{kr}\sin\theta\left(\sum_{n=1}^{\infty}\left[a_n \hat{J}_n(kr) + c_n \hat{H}_n^{(2)}(kr)\right] P_n^{1\prime}(\cos\theta)\right) \\ & + \frac{E_0}{jkr}\sin\theta\left(-\sum_{n=1}^{\infty}\left[a_n \hat{J}_n'(kr) + b_n \hat{H}_n^{(2)\prime}(kr)\right] P_n^1(\cos\theta)\right)\end{aligned} \tag{4.18}$$

$$\mathbf{H}_r^t = \frac{1}{j\eta}\frac{E_0}{(kr)^2}\sin\theta\sin\phi \sum_{n=1}^{\infty} n(n+1)\left[a_n \hat{J}_n(kr) + c_n \hat{H}_n^{(2)}(kr)\right] P_n^1(\cos\theta) \tag{4.19}$$

$$\begin{aligned}\mathbf{H}_\theta^t = {} & \frac{E_0 \sin\theta}{\eta kr}\left(-\sum_{n=1}^{\infty}\left[a_n \hat{J}_n(kr) + b_n \hat{H}_n^{(2)}(kr)\right] P_n^1(\cos\theta)\right) \\ & + \frac{E_0 \sin\theta}{\eta jkr}\left(\sum_{n=1}^{\infty}\left[a_n \hat{J}_n'(kr) + c_n \hat{H}_n^{(2)\prime}(kr)\right] P_n^{1\prime}(\cos\theta)\right)\end{aligned} \tag{4.20}$$

$$\mathbf{H}_{\phi}^{t} = \frac{E_0}{\eta kr}\cos\phi\left(-\sum_{n=1}^{\infty}\left[a_n\hat{J}_n(kr)+b_n\hat{H}_n^{(2)}(kr)\right]P_n^{1\prime}(\cos\theta)\right)$$
$$+\frac{E_0}{\eta jkr}\cos\phi\left(\sum_{n=1}^{\infty}\left[a_n\hat{J}_n'(kr)+c_n\hat{H}_n^{(2)\prime}(kr)\right]P_n^{1}(\cos\theta)\right) \qquad (4.21)$$

Note that the Bessel $a_n\hat{J}_n$ terms represent the incident field and that the Hankel $H_n^{(2)}$ terms represent the scattered field.

4.2.2 Computational Solution

A plane wave incident on a 15 metre radius wire-grid sphere will be used to compare the near field scattering of the two codes. A sphere with wires every 22.5° will be used as illustrated in Figure 4.7.

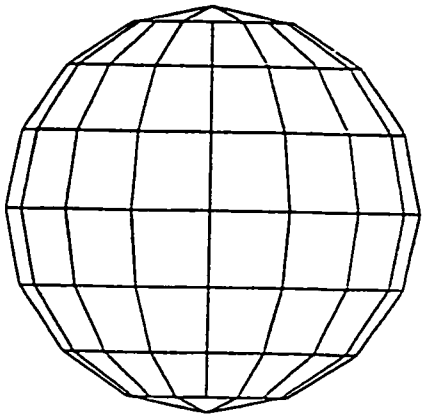

Figure 4.7: Sphere used for near field scattering comparison.

Model preparation was performed by generating the three dimensional coordinates of the various segments centered at the origin, with a radius of $a = 15m$. Wire spacing for the model is $\Delta\phi = \Delta\theta = \pi/8$. The model development software packages described in Section 3.2.2 were then utilized.

The longest segment of each model is at the equator determining the grid size g. Field points are evaluated at the equator with $\theta = 90°$ and $0 \leq \phi < 360°$. The frequency was chosen to ensure that the longest segment in either model would not exceed $\lambda/4$. In this model, the longest segment is $5.853m$ with wire radius $a_w = 0.9128$m. The tested frequency was 12.8 MHz resulting in a grid size of $\lambda/4$ and $ka = \frac{2\pi}{\lambda}a = 4.0$. The total field $\mathbf{E} = \mathbf{E^{inc}} + \mathbf{E^{scatt}}$ was plotted, using a reference level of 0 dB = 1 V/m.

The patch model for Junction was generated for the "$\pi/8$" model by creating one diagonal across each grid in order to build the triangular input required. The

evaluation between the exact solution and the Junction patch solution were indistinguishable at all the tested heights and so they are not shown. Further experiments were performed very close to the surface and some anomalies did develop.

4.2.3 Grid to Height Evaluations

The fields were calculated at three different heights h above the sphere to evaluate the relationship of g/h, i.e. the grid size and height for this comparison: $g/h = 1.25$; $g/h = 2.5$; and $g/h = 3.75$. The geometry is illustrated below in Figure 4.8, and the results incorporate the incident and scattered fields for each of the components.

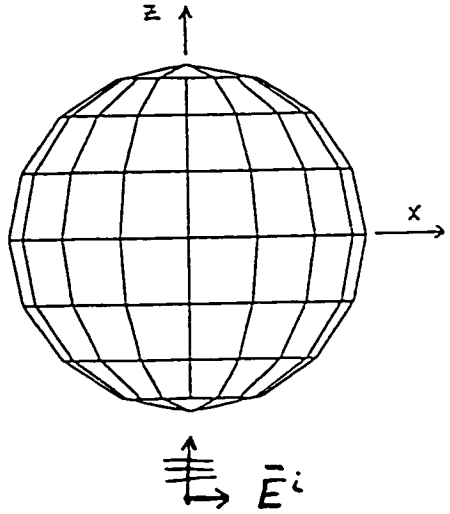

Figure 4.8: Geometry of plane wave incident on the sphere.

Procedure

The procedure consisted of the following for both spheres:

1. Converting existing NEC files to MBC using program CONV.
2. Preparing the Junction input file.
3. Running Junction, NEC and MBC.
4. Generating exact solution results using [58].

These results were then compared using Matlab, presenting graphical representations of the significant components, namely E_r, E_ϑ, and H_ϕ. Each figure will compare one of these components, at the three heights, for both spheres.

Results and Discussion

The results for the E_r component versus θ at $g/h = 3.75$ and $g/h = 2.5$ over the sphere are presented in Figure 4.9.

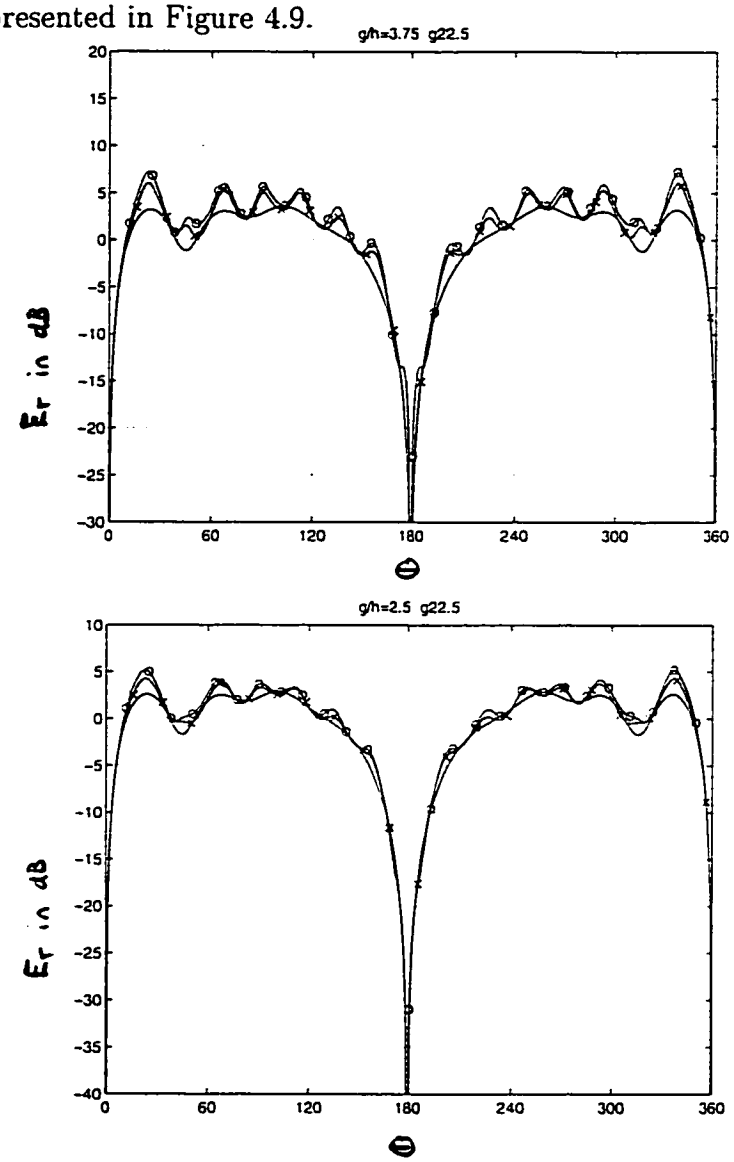

Figure 4.9: E_r vs. θ results at (a) $g/h = 3.75$, (b) $g/h = 2.5$ over sphere. Comparison of the exact solution (—), NEC (+++) and MBC (ooo).

In general, the computational results obtained with NEC and MBC show very good agreement with the exact solution. However the NEC and MBC results very close (i.e. $g/h = 3.75$) to the surface of the sphere show anomalies or "wiggles" compared to the exact solution. The magnitude of the anomalies is comparable in the NEC and MBC, with the wiggles corresponding to the longitudinal junctions at

the equator. As we move away from the surface at $g/h = 2.5$, the characteristics of the anomalies remain but their magnitude has decreased.

The results for the E_r component versus θ at a distance of $g/h = 1.25$ over the sphere, are presented in Figure 4.10.

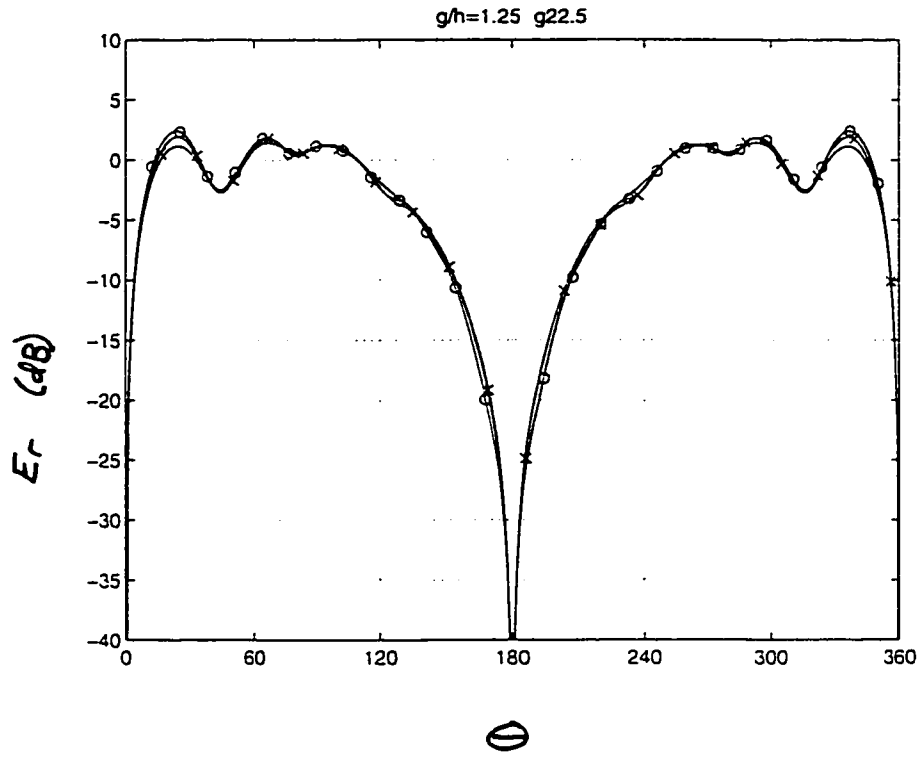

Figure 4.10: E_r vs. θ results $g/h = 1.25$ over sphere. Comparison of the exact solution (—), NEC (+++) and MBC (ooo).

At this distance, the computational results from NEC and MBC are almost identical to the exact solution. The evaluation between the exact solution and the Junction patch solution were indistinguishable at all the tested heights and so they are not shown. Further experiments were performed very close to the surface and some anomalies did develop.

The next results are for the E_θ component versus θ, presented in Figure 4.11,

showing a distance of $g/h = 3.75$ and $g/h = 2.5$ over the sphere. Theoretically, the tangential E_θ component should decrease to zero as the height decreases to the surface of the sphere.

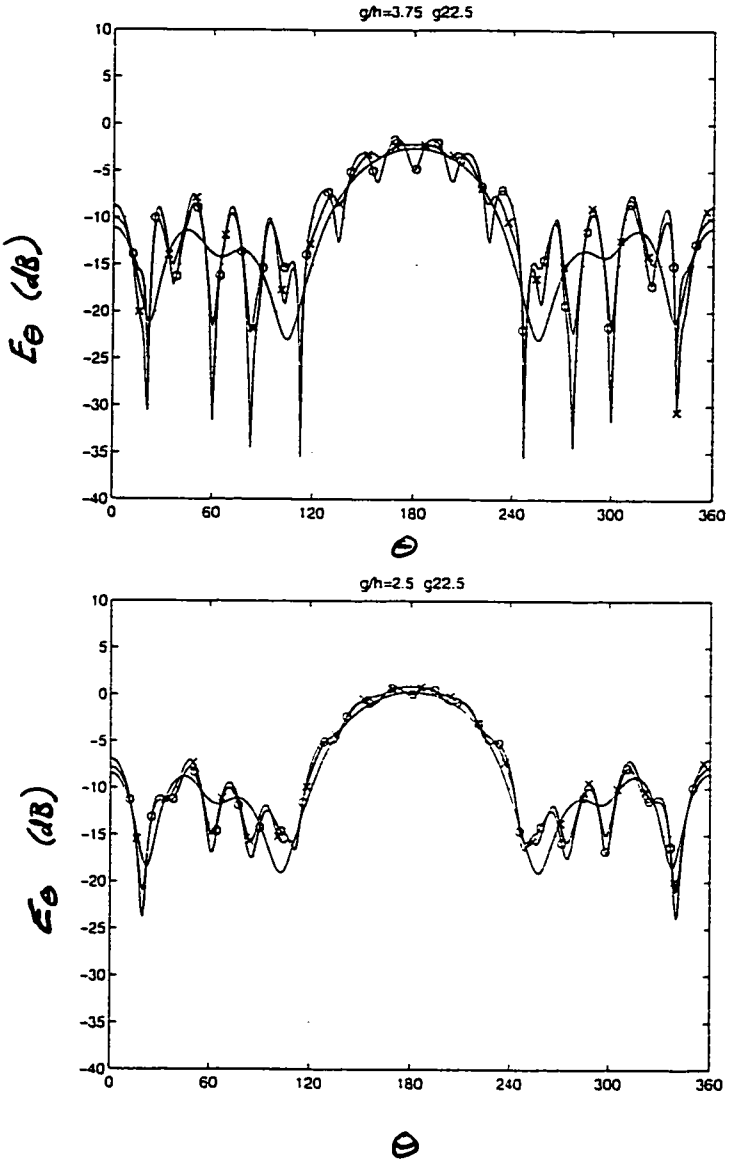

Figure 4.11: E_θ vs. θ results at (a) $g/h = 3.75$, (b) $g/h = 2.5$ over sphere. Comparison of the exact solution (—), NEC (+++) and MBC (ooo).

Close to the surface at $g/h = 3.75$ the anomalies are much more significant than those observed in the normal field ($\mathbf{E_r}$ above). Once again, the number of wiggles corresponds to the logitudinal junctions at the equator. As we move further from

the surface to $g/h = 2.5$, the agreement with the exact solution is much improved, though the anomalies are still significant in the complex model.

The results at a distance of $g/h = 1.25$, shown in Figure 4.12 indicate that there is excellent agreement with the exact solution. Again, there is almost no perceivable difference between the results of MBC and NEC.

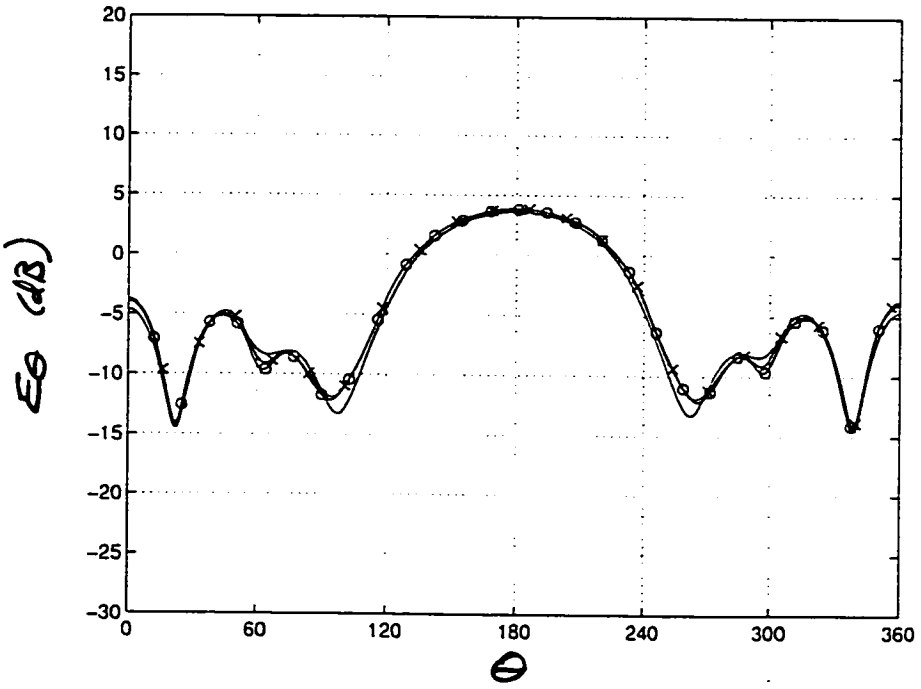

Figure 4.12: E_θ vs. θ results at $g/h = 1.25$ over sphere. Comparison of the exact solution (—), NEC (+++) and MBC (ooo).

The final results are for the H_ϕ component versus θ at distances of $g/h = 3.75$

and $g/h = 2.5$, presented in Figure 4.13.

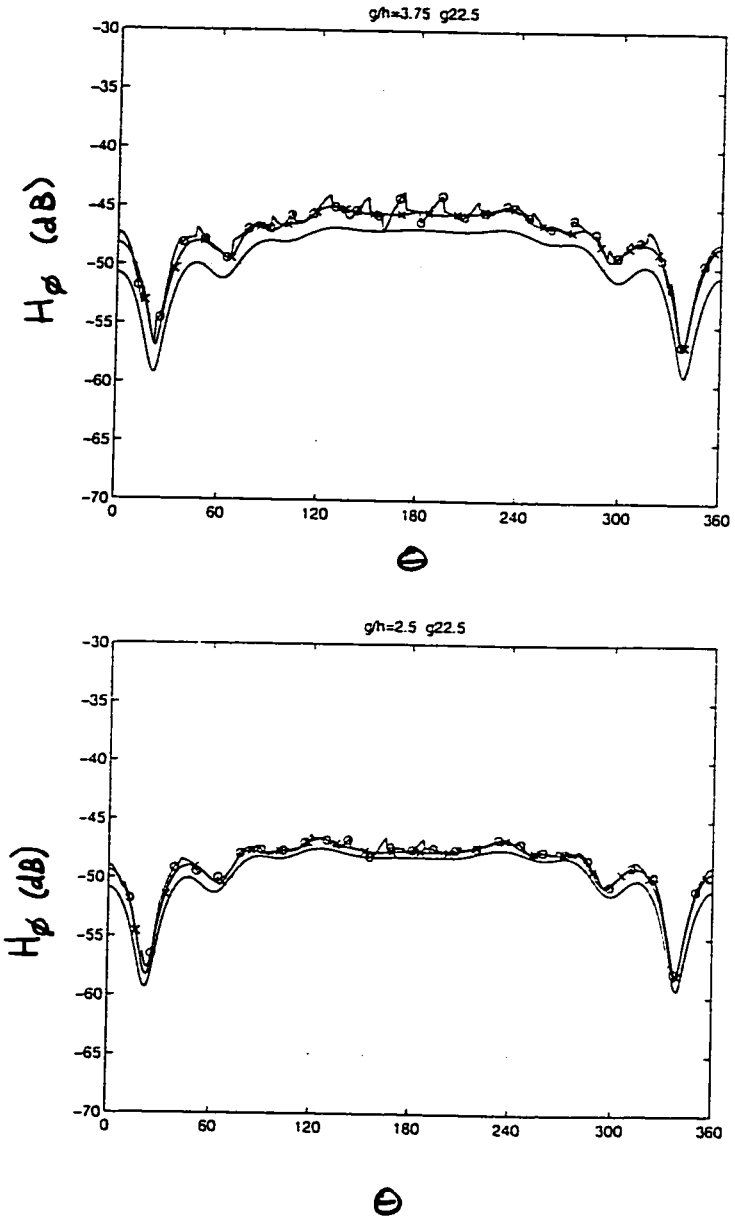

Figure 4.13: H_ϕ vs. θ results at (a) $g/h = 3.75$, (b) $g/h = 2.5$ over sphere. Comparison of the exact solution (—), NEC (+++) and MBC (ooo).

At $g/h = 3.75$ the NEC and MBC results show good agreement with the exact solution, though there is a slight offset in the level. As the distance increases to $g/h = 2.5$, the computed solutions from the two codes are consistent with the exact solution. It is interesting to note that the MBC solution exhibits some asymmetric spikes which NEC does not produce.

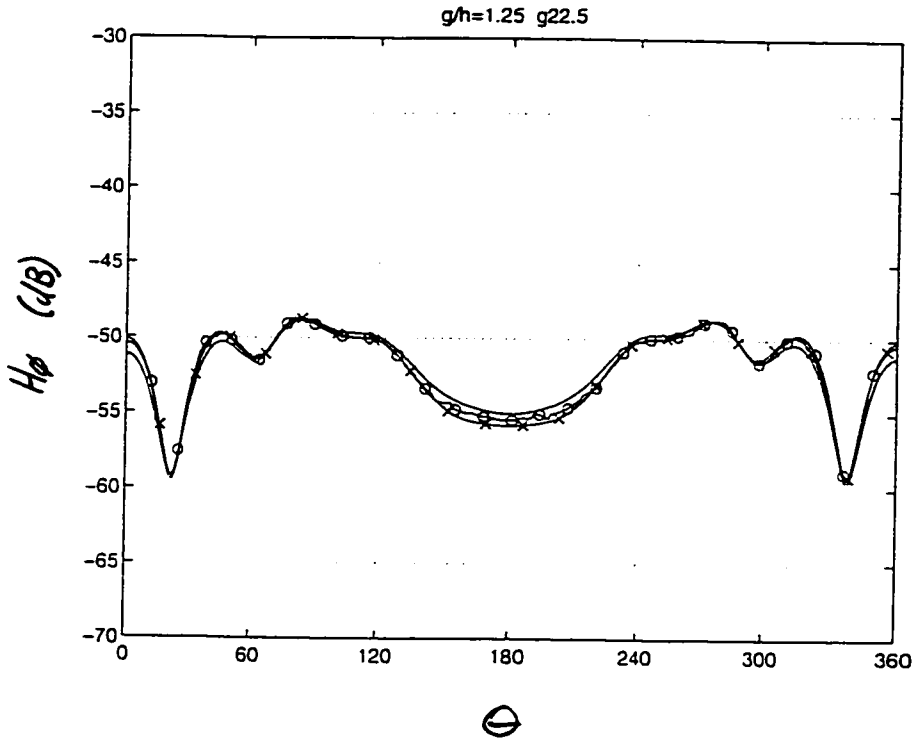

Figure 4.14: H_ϕ vs. θ results at $g/h = 1.25$ over sphere. Comparison of the exact solution (—), NEC (+++) and MBC (ooo).

The results at $g/h = 1.25$, shown in Figure 4.14, indicate that the solutions of the two codes show excellent agreement. At this height above the sphere, the spikes observed in the MBC solution closer to the surface are no longer visible.

It is interesting to note that the $E_\theta/H_\phi \approx 377 \approx \eta_o$, which would be expected when the radiation behaves like "locally plane" waves as in the far field region.

4.2.4 Same Surface Rule Evaluations

An examination of the same surface rule was performed by comparing the exact solution to that generated by NEC with wires too thin and too thick. The $\pi/8$ model sphere is used at field points a distance of $g/h = 1.25$ or 4.68 m off the surface from the equator of the sphere in order to minimize the anomalies yet obtain results as close as possible to the surface of the sphere. The grid size at the equator is $g = 5.853$m with a wire radius of $a_w = 0.9128$m. A frequency of 5.1248 MHz was chosen resulting in a grid size $g = 0.1\lambda$ and $ka = 1.6$.

Results and Discussion

The results for the E_r component versus θ are presented in Figure 4.15.

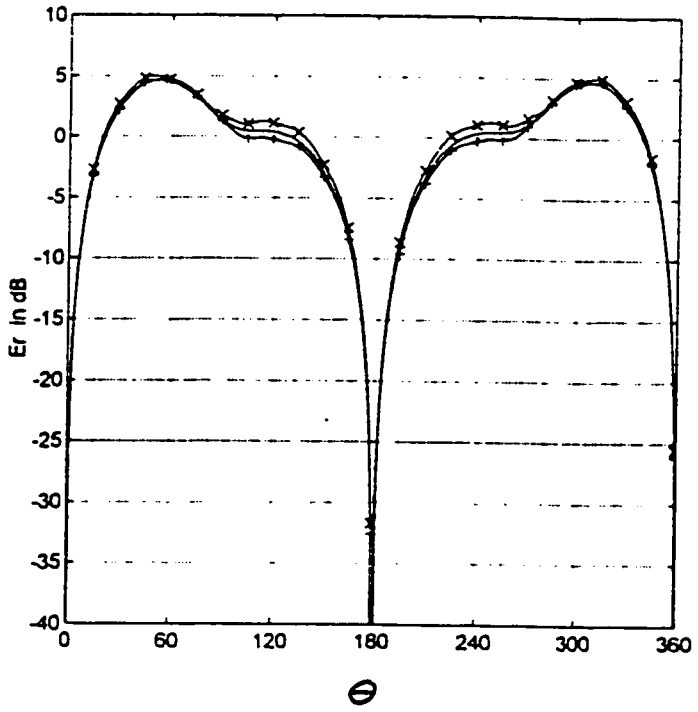

Figure 4.15: E_r vs. θ results achieved by varying wire radii. Exact solution (—) compared with NEC at $a_w/2$(+++) and $2a_w$ (xxx) at height $g/h = 1.25$.

The results for the E_θ component versus θ are presented in Figure 4.16.

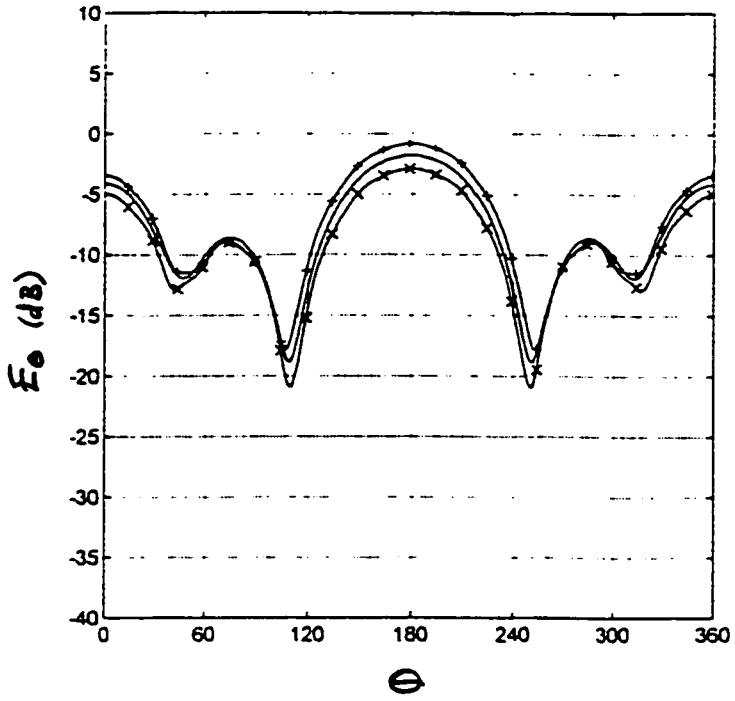

Figure 4.16: E_θ vs. θ results achieved by varying wire radii. Exact solution (—) compared with NEC at $a_w/2$(+++) and $2a_w$ (xxx) at height $g/h = 1.25$.

Compared to the plate, the results of the tangential field vary much less due to variations of wire radius of the model. However adhering to the same surface rule generated the best calculated results for both the normal and tangential E fields unlike the results observed with the plate in Section 4.1.2. The same experiment was repeated with MBC yielding almost identical results.

4.2.5 Summary

The results of this section indicate that Junction is very well suited for the computation of the near field for smooth bodies. It was also found that wire grid modelling provides very good results provided a minimum distance of $g/h = 2.5$ on the lit side,

and $g/h = 1.25$ on the shadow side are respected. Generally, optimal electric field results are computed when the same surface rule is respected. though this did not hold true for the normal electric field on the plate.

There is almost no difference between the results of NEC and MBC in the near fields. This is somewhat surprising since their formulations are very different. This indicates that the implementation type of the moment method used in wire grid modelling is not a major determinant.

Chapter 5

Far Field Experiments

5.1 RCS of Two Plates

5.1.1 Objective

The objective of this demonstration is to present a first comparison between the MBC and NEC codes, and to try to validate them with an approximate solution, namely Physical Optics. The use of two simple geometries should build confidence in the accuracy of the two codes. Using a frequency of 300 MHz, two different grid sizes, 0.1λ and 0.25λ, are used to compare the results of the MBC and NEC codes.

5.1.2 Methodology

The bistatic radar cross-section of a plane wave incident on two plates is calculated, where one plate is 1m by 1m, and the other is 3m by 1m. The incident plane is $\hat{x}$ polarized travelling in the $-z$ direction, i.e. $\mathbf{E}^{inc} = \hat{x}e^{jkz}$. The geometry of the problem is pictured below in Figure 5.1. The results will be compared to the physical optics solution.

5.1.3 Procedure

The procedure for this study consisted of the following:

1. Creating the NEC input files.
2. Converting NEC files to MBC using program CONV.

3. Running NEC and MBC.
4. Running P.O. solution.

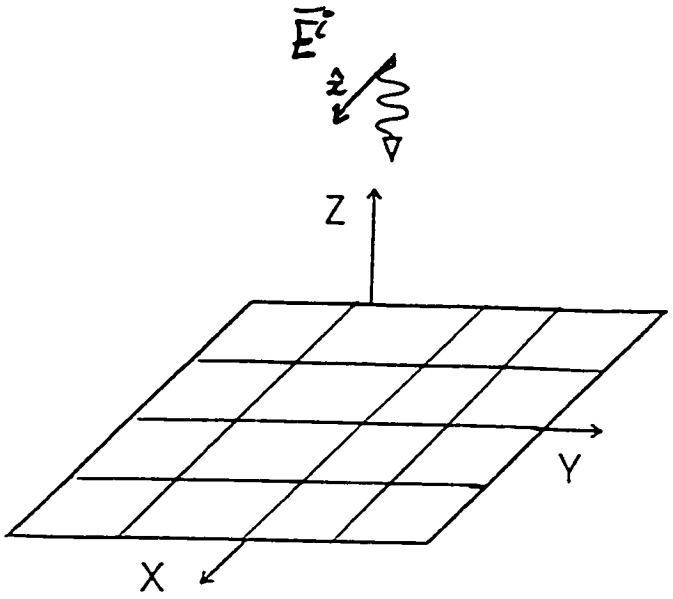

Figure 5.1: Geometry for the incident field on the plate.

The results are then presented graphically by calculating the Radar Cross-Section using the E_θ field as described in equation (2.22), using Matlab.

5.1.4 Results and Discussion

The results of the $1 \times 1m$ plate are shown below in Figure 5.2. For both grid sizes, the graphs show very good agreement for both the NEC and MBC results. The maximum level when measured broadside converge toward the physical optics solution, with the finer grid showing very good results.

The results of the 3×1 plate are shown below in Figure 5.3. Here again, the graphs show very good agreement for both the NEC and MBC results for both grid sizes, with the finer grid matching the physical optics result over a wider range than that of the 1×1 plate results.

It is interesting to note that the modelling guidelines for NEC suggest that 0.2λ be the longest segment used, yet NEC still produces almost the same results as MBC.

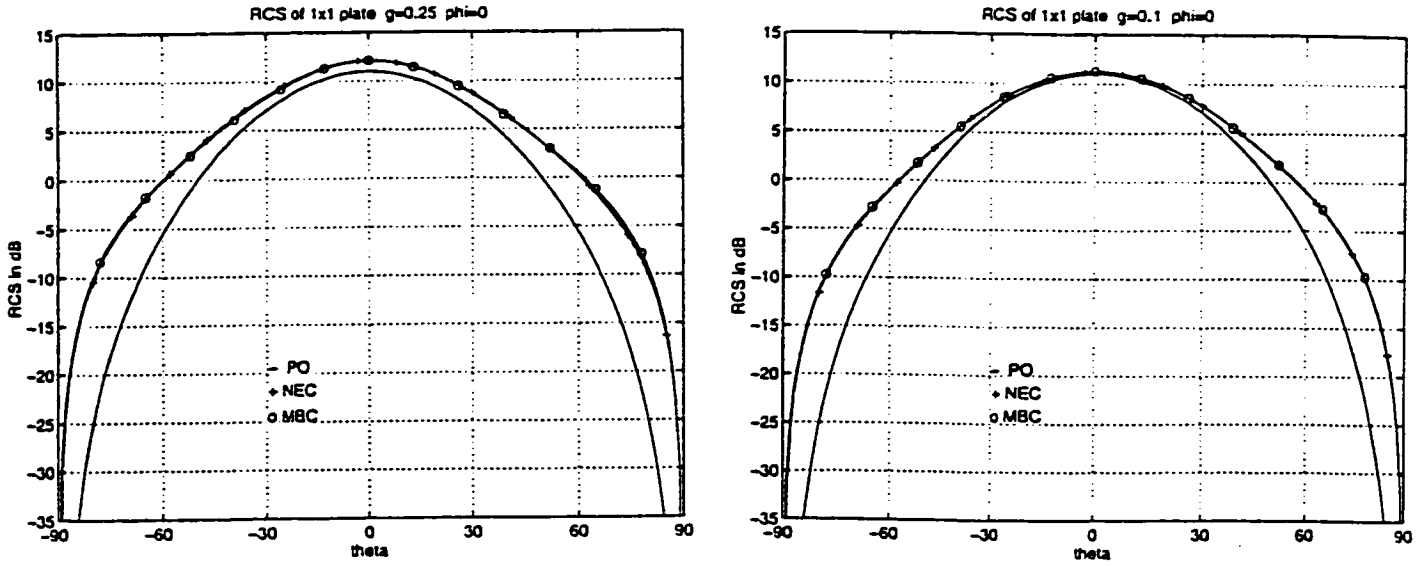

Figure 5.2: RCS results for 1×1 plate. a) 0.25λ grid, b) 0.1λ grid.

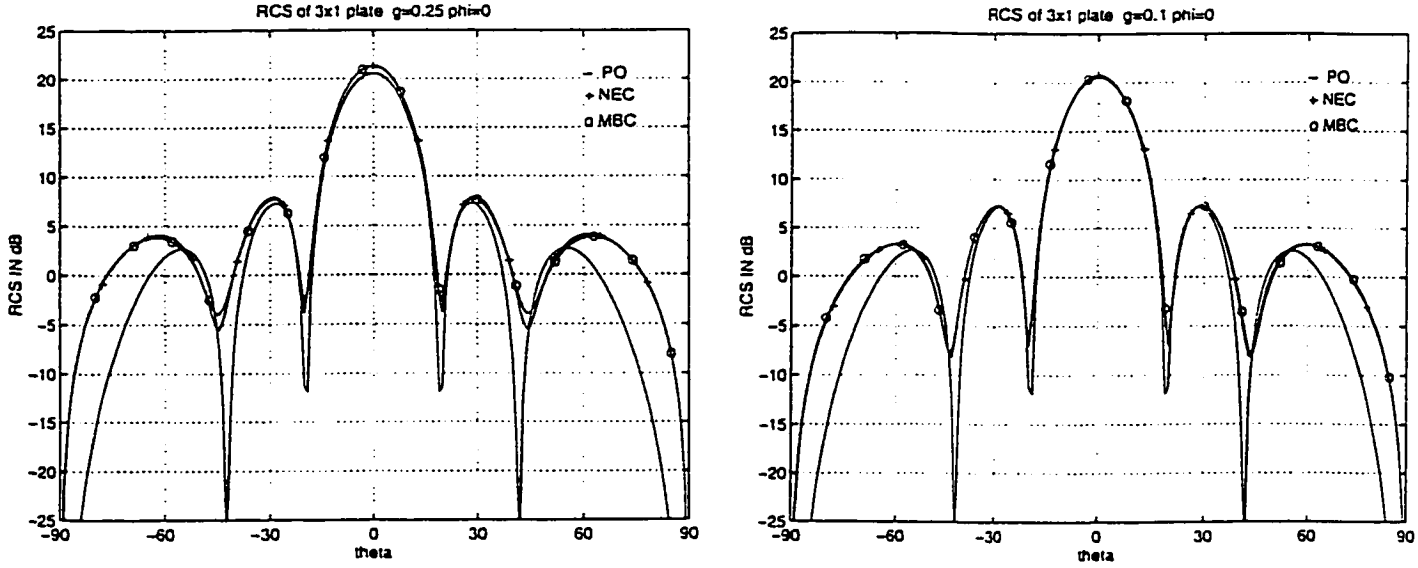

Figure 5.3: RCS results for 3×1 plate. a) 0.25λ grid, b) 0.1λ grid.

5.2 Radiator on a Conducting Sphere

The radiation pattern of an antenna placed on the North pole of a sphere is examined in this section. Using the Reciprocity Theorem, the exact solution of a plane wave incident upon the sphere in Section 4.2.1 is used to determine of the radiated fields caused by an antenna on the sphere, and these calculated resulted are compared to the results generated by NEC and MBC. The solution to the antenna mounted on a sphere is solved in [59]

5.2.1 Exact Solution

Reciprocity Theorem

Similar to its application to basic electrical circuit analysis, the reciprocity theorem can be used to relate the transmission and reception characteristics of radiating systems.

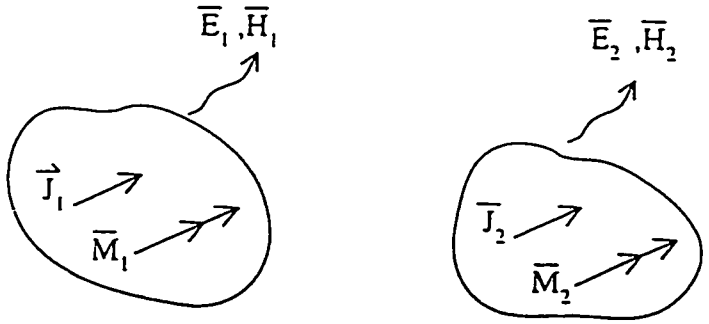

Figure 5.4: Example of Reciprocity Theorem.

If we consider the example presented in Figure 5.4, it can be shown [60] that

$$\int_V \mathbf{E}_1 \cdot \mathbf{J}_2 - \mathbf{H}_1 \cdot \mathbf{M}_2 dv' = \int_V \mathbf{E}_2 \cdot \mathbf{J}_1 - \mathbf{H}_2 \cdot \mathbf{M}_1 dv'. \tag{5.1}$$

The reciprocity theorem in the form of Equation 5.1 is used to establish that the transmitting and receiving patterns of an antenna are the same[61].

Plane Wave Source

In order to use reciprocity, we first determine a source of the plane waves in Section 4.2.1. Consider an electrically small dipole $I_1\ell_1(\hat{x})$ placed far from the sphere at location $(r_1, \pi, 0)$, as per Figure 5.5.

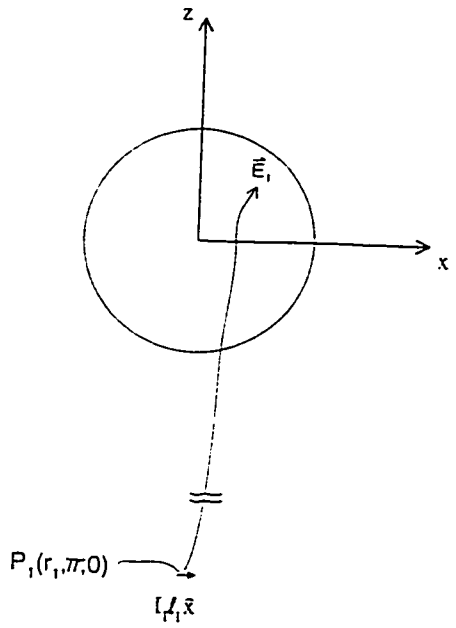

Figure 5.5: Conducting sphere and a dipole source.

For an electrically small dipole,

$$A_x = \frac{\mu I_1 \ell_1}{4\pi} \frac{e^{-jkR_1}}{R_1} \tag{5.2}$$

and

$$\mathbf{E}_x \simeq -j\omega \mathbf{A}_x = \frac{-j\omega\mu I_1 \ell_1}{4\pi} \frac{e^{-jkR_1}}{R_1}. \tag{5.3}$$

Using the far-field approximation

$$R_1 \simeq r_1 + a\cos\theta \tag{5.4}$$

for any points 'p' on the sphere, we obtain

$$\mathbf{E}_x = \frac{-j\omega\mu I_1\ell_1}{4\pi}\frac{e^{-jkr_1}}{r_1}e^{-jka\cos\theta} \tag{5.5}$$

noting that $z = a\cos\theta$. By defining

$$E_0 = \frac{-j\omega\mu I_1\ell_1}{4\pi}\frac{e^{-jkr_1}}{r_1}, \tag{5.6}$$

and fixing the values of r_1 and $I_1\ell_1$, we obtain a plane wave

$$\mathbf{E}^{\mathrm{i}} = \mathbf{E}_{\mathbf{x}} = E_0 e^{-jkz}. \tag{5.7}$$

This plane wave $\mathbf{E}^{\mathrm{i}}$ produces the scattered field portion of $\mathbf{E}_{\mathrm{r}}$ (Equation 4.16) on the sphere or

$$\mathbf{E}_{\mathrm{r}} = f(\theta,\phi) = \frac{E_0\cos\phi\sin\theta}{j(kr)^2}\sum_{n=1}^{\infty} n(n+1)\left[b_n\hat{H}_n^{(2)}(kr)\right]P_n^1(\cos\theta). \tag{5.8}$$

For compactness, we shall define this field as

$$\mathbf{E}_{\mathrm{r}} = f(\theta,\phi). \tag{5.9}$$

Reciprocal Solution

We want to evaluate the far field produced by a radially directed small monopole $I\ell\hat{r}$ placed upon the conducting sphere as illustrated in Figure 5.6.

To solve this problem, we use the Reciprocity Theorem and note that with the absence of magnetic sources $\mathbf{M}$, Equation (5.1) reduces to

$$\int_V \mathbf{E_1}\cdot\mathbf{J_2}dv' = \int_V \mathbf{E_2}\cdot\mathbf{J_1}dv'. \tag{5.10}$$

Applying reciprocity to the current system, we obtain

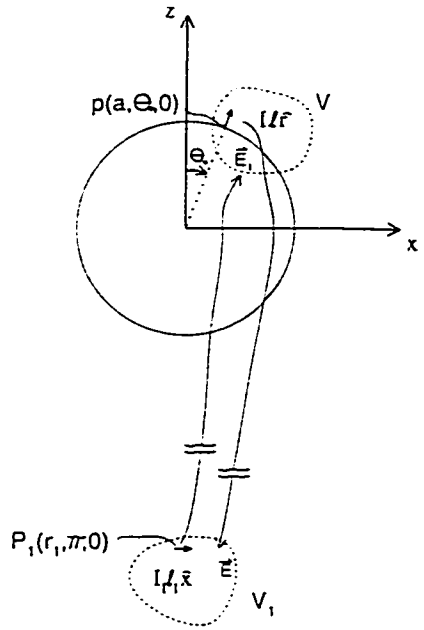

Figure 5.6: Conducting sphere with a dipole source and the reciprocal problem with a monopole mounted on the surface of the conducting sphere.

$$\int_V \mathbf{E_1} \cdot \hat{r} I \ell dv = \int_V \mathbf{E} \cdot \hat{x} I_1 \ell_1 dv_1. \tag{5.11}$$

As we have assumed that the sources are electrically small, we can thus view these sources as *delta*-sources. Hence Equation 5.11 is reduced to

$$\mathbf{E_1} \cdot \hat{r} I \ell \mid_p = \mathbf{E} \cdot \hat{x} I_1 \ell_1 \mid_{p_1} \tag{5.12}$$

or

$$\mathbf{E}_{x_{(p_1)}} = \frac{I\ell}{I_1 \ell_1} \mathbf{E_1} \cdot \hat{r} \mid_p . \tag{5.13}$$

Using equations 5.6 and 5.7, and the compact form of the radial field in Equation 5.8, we obtain

$$\mathbf{E_1} \cdot \hat{r} \mid_p = -\frac{j\omega\mu I_1 \ell_1}{4\pi E_0} \frac{e^{-jkr_1}}{r_1} f(\theta, \phi). \tag{5.14}$$

Substituting this into Equation 5.13 produces

$$\mathbf{E}_{\mathbf{x}(p_1)} = -\frac{j\omega\mu I \ell}{4\pi E_0} \frac{e^{-jkr_1}}{r_1} f(\theta, \phi). \tag{5.15}$$

To take into account the rotation of the geometry, we translate using $r = a$, $\theta = \pi - \theta_0$, and with $\hat{x} \cdot \hat{\theta} = -1$, we produce the radiation pattern

$$\mathbf{E}_\theta = +\frac{j\omega\mu I \ell}{4\pi E_0} \frac{e^{-jkr_1}}{r_1} f(\pi - \theta_0, \phi). \tag{5.16}$$

Substituting back in the value of $\mathbf{E_r}$ for $f(\theta, \phi)$, collecting terms and simplifying, the radiation pattern can be expressed as

$$\mathbf{E}_\theta = \frac{\eta I \ell}{4\pi jkr} e^{-jkr} \sum_{n=1}^{\infty} \frac{j^n (2n+1)}{\hat{H}_n^{(2)\prime}(ka)} P_n^1(\cos(\pi - \theta_0)). \tag{5.17}$$

5.2.2 Computational Solution

The 15 metre radius wire-grid sphere with wires every 22.5°, used in Section 4.2.2, will be used to compare the radiated field of the MBC and NEC codes. A monopole antenna of length $a/5$ or 3.0m is placed on the north pole as illustrated in Figure 5.7, and the results are compared to the exact solution produced in the previous section. Note that there are more wire junctions at the North and South poles of the model, and thus their wire radii are thinner than those at the equator, as calculated by the model development software packages Meshes and FNDRAD.

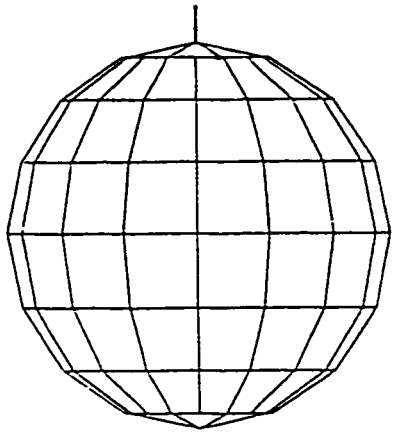

Figure 5.7: Sphere with monopole used for far field radiation pattern comparison.

Wavelengths λ of $6a$, $4a$ and $2a$ i.e. $90m$, $60m$ and $30m$ respectively were selected resulting in frequencies of 3.331 MHz, 4.997 MHz and 9.995 MHz respectively for the three cases.

Procedure

The procedure for the evaluation of radiation patterns produced by a monopole placed on a conducting sphere consisted of the following:

1. Converting existing NEC files to MBC using program CONV.
2. Running NEC and MBC.
3. Generating exact solution results.

The resulting radiation patterns were then processed using Matlab.

5.2.3 Results and Discussion

The radiation pattern for the case $\lambda = 6a$ is presented in Figure 5.8. At this frequency, the wavelength is three times the size of the model. The results indicate that the NEC, MBC and exact solutions are almost indistinguishable from each other.

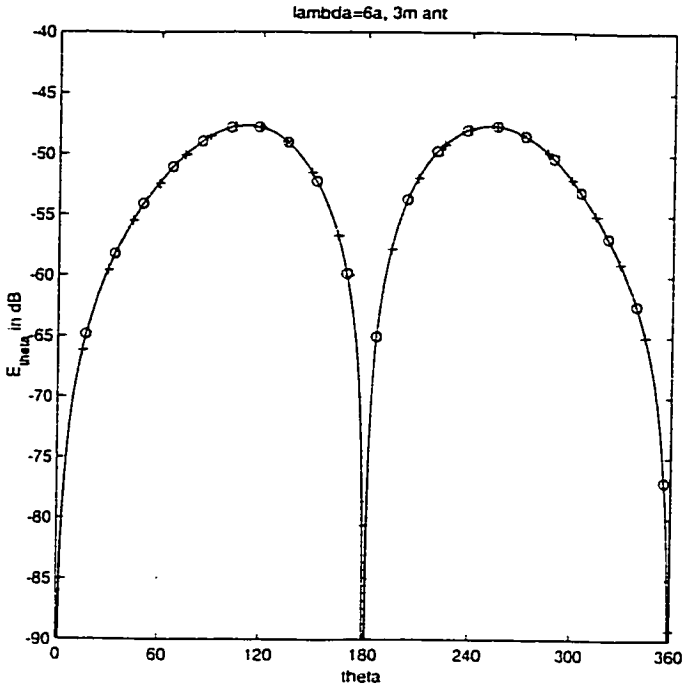

Figure 5.8: Radiation pattern of the monopole on a conducting sphere with $\lambda = 6a$. Comparison of the exact solution (—), NEC (+++) and MBC (ooo).

Decreasing the wavelength to two times the sphere diameter, i.e. $\lambda = 4a$, both codes generate results that agree very closely with the exact solution, as illustrated in Figure 5.9.

Further decreasing the wavelength to $\lambda = 2a = 30.0m$, the dimension of the sphere model, the results by both codes still show good agreement with the exact solution. The results are shown in Figure 5.10. However results obtained by further reducing the wavelength did not converge properly. This was to be expected since the moment method is best suited for models smaller than one wavelength.

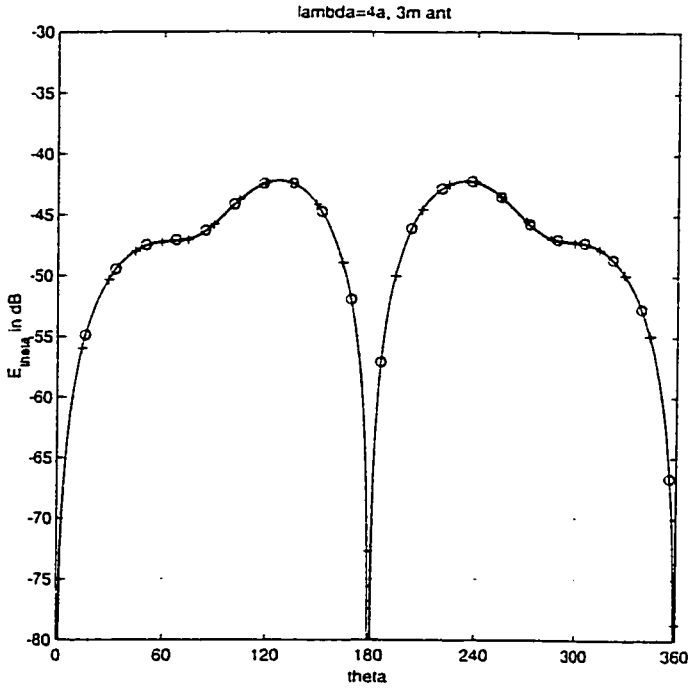

Figure 5.9: Radiation pattern of the monopole on a conducting sphere with $\lambda = 4a$. Comparison of the exact solution (—), NEC (+++) and MBC (ooo).

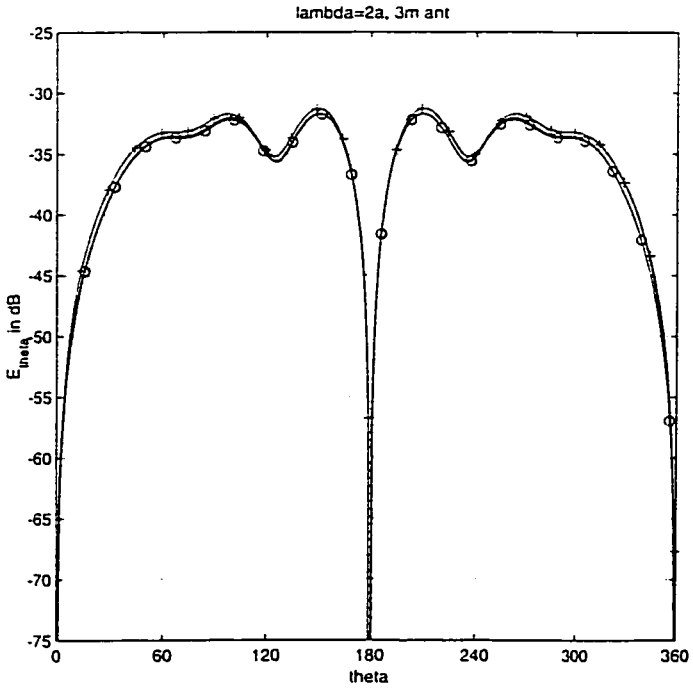

Figure 5.10: Radiation pattern of the monopole on a conducting sphere with $\lambda = 2a$. Comparison of the exact solution (—), NEC (+++) and MBC (ooo).

5.2.4 Same Surface Rule Evaluation

An examination of the same surface rule was performed by comparing the exact solution to that generated by MBC with wires too thin and too thick. A frequency of 4.995 MHz was chosen resulting in a wavelength $\lambda = 4a = 60m$. Results in the previous section showed excellent agreement with the exact solution when respecting the same surface rule.

The grid size at the equator is $g = 5.853$m with a wire radius of $a_w = 0.9128$m. The wire radii are double the 'proper' value for one evaluation of MBC, and then half the 'proper' value for another, where the proper values are those which respect the same surface rule.

Results and Discussion

The results shown in Figure 5.11 support once again that respecting the same surface rule produces the most accurate results. Nearly identical results were obtained when performing this evaluation with NEC.

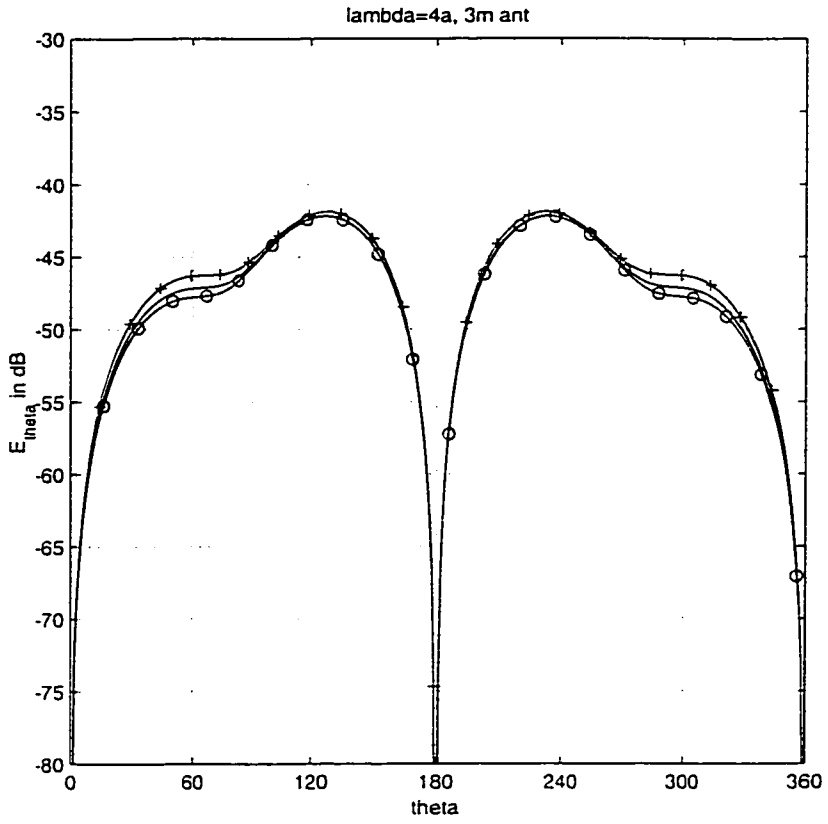

Figure 5.11: Radiation pattern of the monopole on a conducting sphere with varying wire radii at $\lambda = 4a$. Comparison of the exact solution (—), MBC with $2a_w$ (+++) and MBC with $a_w/2$ (ooo).

5.3 Bell-412 Helicopter Model Frequency Sweep

Modern aircraft incorporate a large number of antennas for different communication and navigation requirements. For example, consider the multitude of antennas connected to the Canadair Global Express in Figure 5.12. With the large conducting surface of an aircraft, it is important to understand how the structure may interfere with an antenna's operation. The coupling of different systems is also a concern in these applications, and electromagnetic codes such as NEC and MBC are powerful tools to help gain insight into potential electromagnetic compatibility (EMC) problems.

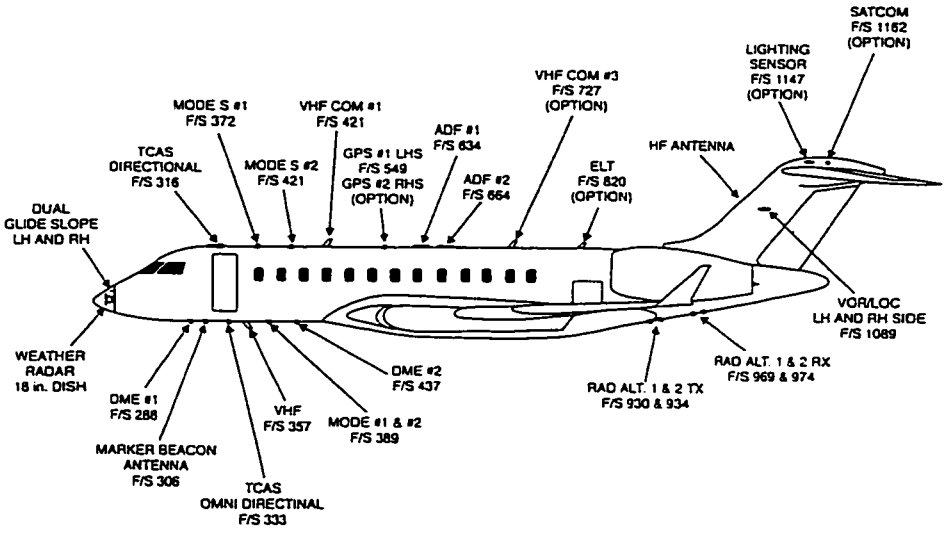

Figure 5.12: Antenna location diagram for the Canadair Global Express.[62]

5.3.1 Background

The analysis of antenna placement on aircraft requires considerable measurement of radiation patterns over the antenna's operating range. Ground breaking research by Granger[63] investigated the interaction of various types of antennas mounted

on airframes. He found the relationship between the aircraft dimensions and the wavelength impacts antenna characteristics. The size of many aircraft are comparable with the wavelength of the HF band thus their structure has significant impact upon the antenna performance.

Granger[64] also investigated the distribution of current on various aircraft structures. In the HF band, he researched the relationship between antenna performance and current resonances resulting from the comparable size of the airframe and the wavelength, and provided valuable insight into the input impedance and radiation patterns for many aircraft antennas.

5.3.2 Related Research

As computer modelling developed, it has rendered this task into a manageable activity by providing a means of predicting radiation patterns as well as RF current flows along the surface of the aircraft. The performance of the antenna mounted on the aircraft body can be assessed by performing multiple frequency sweeps. Powerful software packages assist in the visualization of the results by presenting graphical representations of the current distribution, providing insight to the resonance of the aircraft as well as nulls and lobes of the radiation patterns.

For decades now, numerical modelling has been implemented to predict antenna radiation patterns or scattering problems at research institutions around the world, including the EMC Laboratory. Some of the pioneering work included wire grid models of various helicopter HF antennas examined by Kubina and Pavlasek[65].

There have been a number of graduate students who have applied numerical modelling of antennas in aerospace applications at the Concordia University EMC Laboratory. Larose[66] performed a numerical analysis of HF antennas mounted upon a wire grid model of the CP-140 Aurora. The models ranged in complexity from simple to relatively complex configurations. The study compared the computed radiation and antenna input characteristics of each model with those measured on a range.

Later, a series of wire-grid models of the C130 Hercules with five HF antennas were developed by Rosenzweig[67]. In 1994, Luu[19] studied the antenna-to-antenna and antenna-to-airframe HF coupling of two aircraft, namely the C130 and the Canadair CL-600 Challenger jet. Continuing advances in computer power enabled a HF frequency sweep with relatively fine precision intervals.

Bahsoun[17] developed the first helicopter models at the EMC Laboratory. The results of an HF antenna mounted on the airframe obtained by numerical techniques were compared to those of measurements performed on a scale model.

Esfandiari[35] performed an analysis on a Bell CH-135 helicopter. The study performed a comparison of scale-model measurements to the results of computer simulations of two different HF antennas mounted on the structure.

5.3.3 Objective

This section of the report will compare a high frequency sweep of a complex helicopter model using the two codes. Although there will be no measured test results to compare with the solutions of the codes, this exercise will introduce some of the techniques employed when performing antenna analysis.

5.3.4 Methodology

The high frequency sweep will range from 2.0 MHz to 30.0 MHz in incremental steps of 0.1 MHz. The comparison will examine the total radiated power, the efficiency in the various components as described earlier in this report, the radiation patterns and the representative currents on the structure.

5.3.5 Model Preparation

Substantial work has been done at Concordia University's EMC laboratory with respect to the modelling of different aircraft, including many airplanes and helicopters. The Bell-412 helicopter has a height of $4.57m$, fuselage length of $12.7m$ metres, with

rotor diameter measuring $14.0m$.

It is desirable to use a single model for the HF band usually tested (2-30 MHz) where the wavelength varies from $150m$ to $10m$. The ratio of segment length to wavelength varies substancially. The conventional practice at the EMC Laboratory is to design the model such that a maximum segment length of $\lambda/10$ occurs at a frequency of about 11 MHz. This trade-off helps to minimize the degradation of the results as the frequency increases towards the high end of the band. The complex model of the Bell 412 helicopter used in this report was developed in the EMC lab over the years[17, 35].

In these previous works, the results of other analysis using the complex model were compared to actual measurements on a scale model at the National Research Council's antenna range in Ottawa, Ontario. The results of the actual measurements compared to those of the NEC simulations showed agreement both quantitatively and qualitatively[35]. The antenna used in this study is a short circuited transmission line antenna connected from the aft of the cabin to the tip of the tail. The model of the antenna is shown in Figure 5.13 with the antenna wire radii exagerated for emphasis.

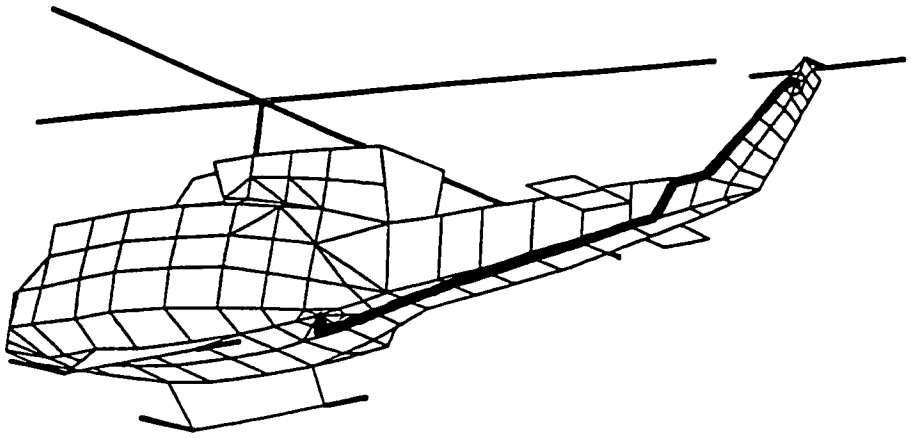

Figure 5.13: Emphasized tran-line antenna mounted on the helicopter.

5.3.6 Procedure

NEC runs

Once the program cards (i.e. the NEC input file GW cards) containing the model were completed, the radiation pattern control cards were inserted for the radiation pattern specifications required[48, 49], and the frequency was selected for the run, and then the resulting file was input to NEC. The output of NEC is passed through STRIP, a small program used to remove unnecessary information from the solution file, and then passed through ISOLEV. The resulting solution files were then compressed using the Unix utility GZIP.

MBC runs

To perform the MBC runs, the following procedure was required:

1. Convert NEC input file to MBC file using program CONV (i.e. nec.gw $\Rightarrow$ mbc.in)
2. Copy NEC input file (nec.gw $\Rightarrow$ mbc.sol)
3. Run MBC (mbc mbc.in mbc.out)
4. Translate MBC solution file to NEC format using program TRAN (mbc.out $\Rightarrow$ nec.sol)
5. Append translated solution to copied NEC file (i.e. cat nec.sol $\gg$ mbc.sol)
6. Run program ISOLEV.

This procedure produces an MBC output in the NEC format, and thus enables us to perform the side-by-side comparison with the established software.

These two procedures were repeated for all the frequencies in the sweep. Once completed, the program EXTRAC was used to produce the input files for RPLOT. The comparison of the various antenna parameters is then analyzed using the software outlined in Chapter 4.

The different rectangular views of the developed model are presented in Figure 5.14

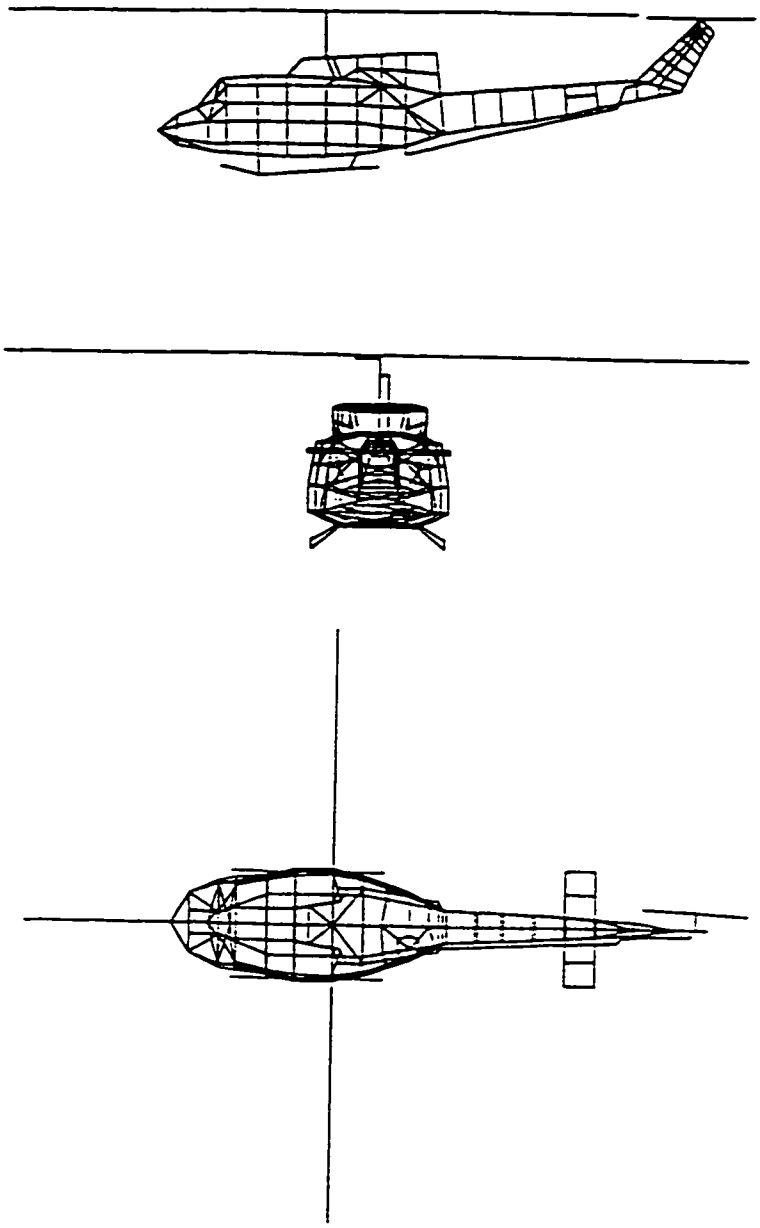

Figure 5.14: Rectangular views of the helicopter model.

5.3.7 Results and Discussion

Frequency Sweep

This section contains the results obtained in the frequency sweep. Figure 5.15 presents the total radiated power and isotropic level respectively.

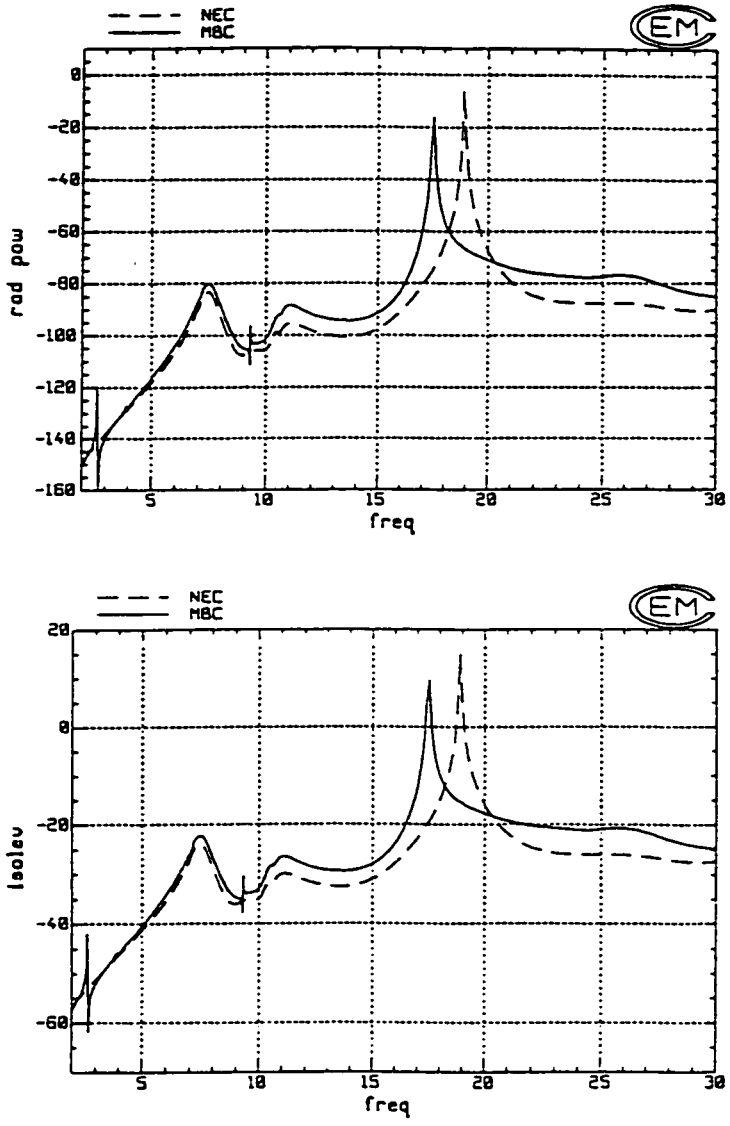

Figure 5.15: Power comparison results with MBC (—) and NEC (- -): a) Total radiated power b) Isotropic results.

The results show that the MBC solution produces anomalies at approximately 2.6 MHz and 9.5 MHz. Further investigation into these anomalies led the MBC code author Tilston to update two subroutines within the program. In subsequent evaluations with MBC and NEC the anomalies were no longer present[68].

Also of interest are the two "humps" around 7 MHz and 11 MHz. These frequencies give indications of resonant modes when significant currents develop along the rotors or airframe. Current flowing to the rotors is evident illustrated in Section 5.3.7 presenting the current distribution at 7.0 MHz.

The radiated power efficiency results, shown in Figure 5.16 reveal similar characteristics.

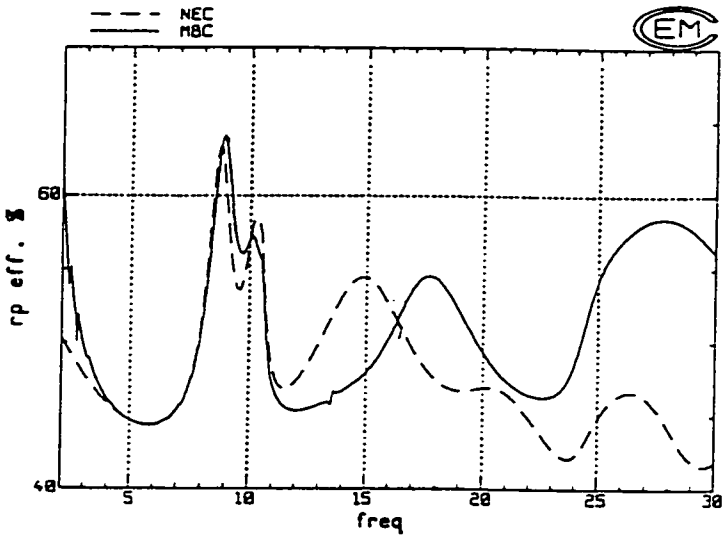

Figure 5.16: Radiated power efficiency results.

Next, the results of the "percent" E_θ and sub E_θ are shown in Figure 5.17.

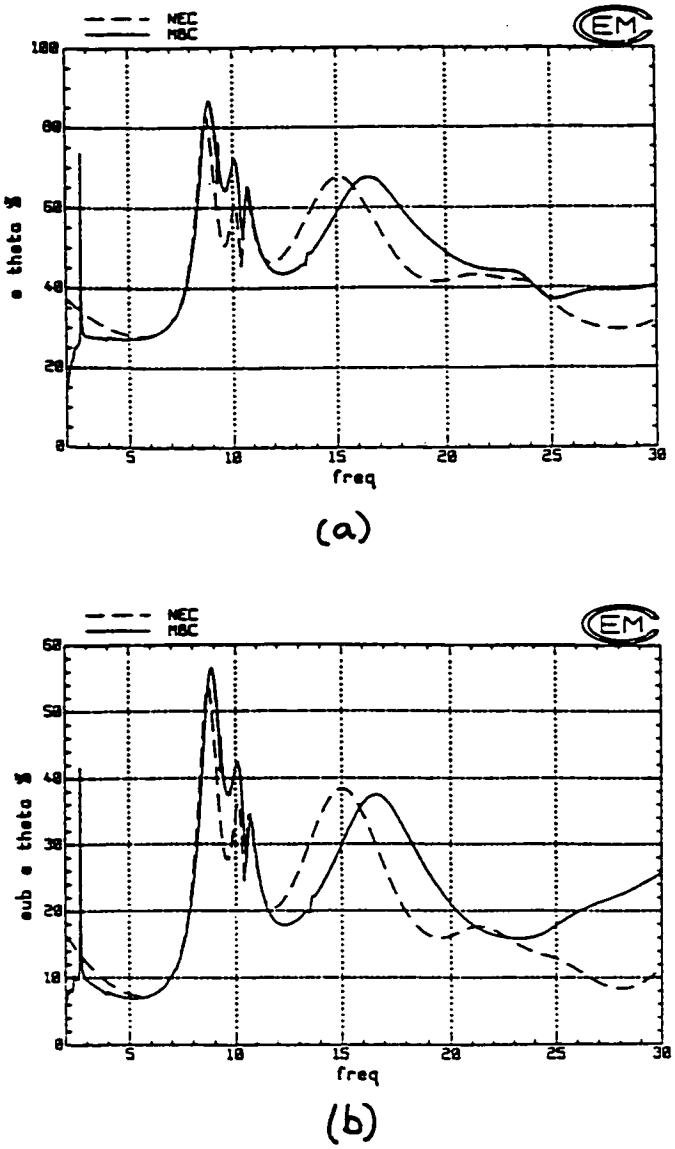

Figure 5.17: a) Percent E_θ results b) Percent sub E_θ results.

The impedance results are presented in Figures 5.18 and 5.19.

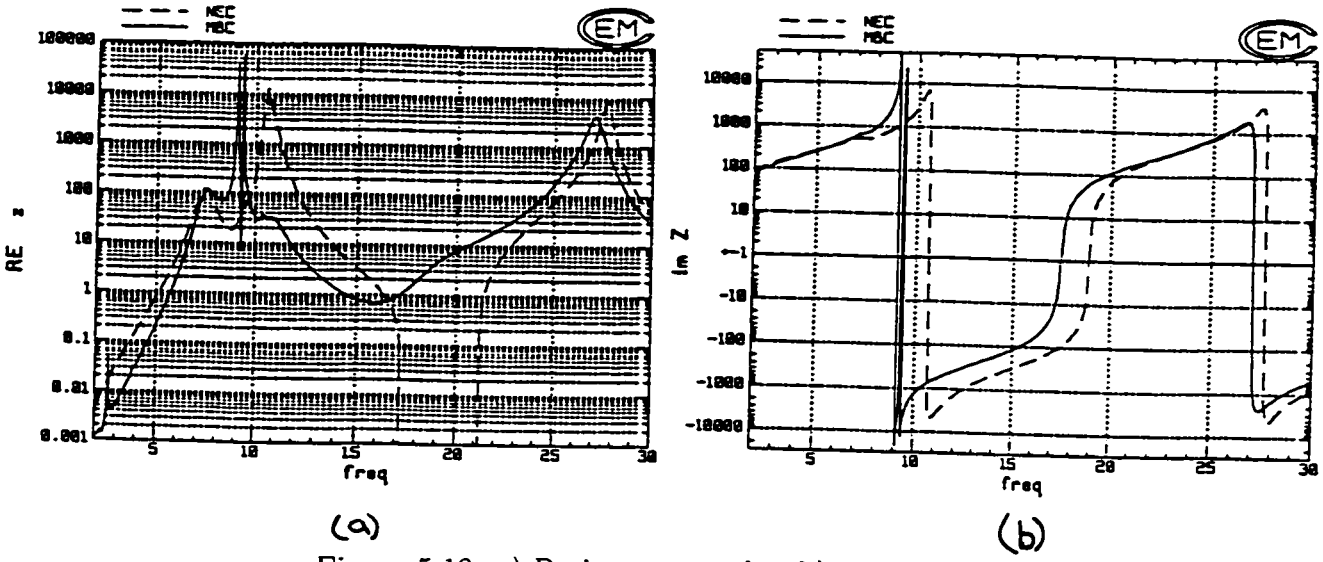

Figure 5.18: a) Resistance results, b) reactance results.

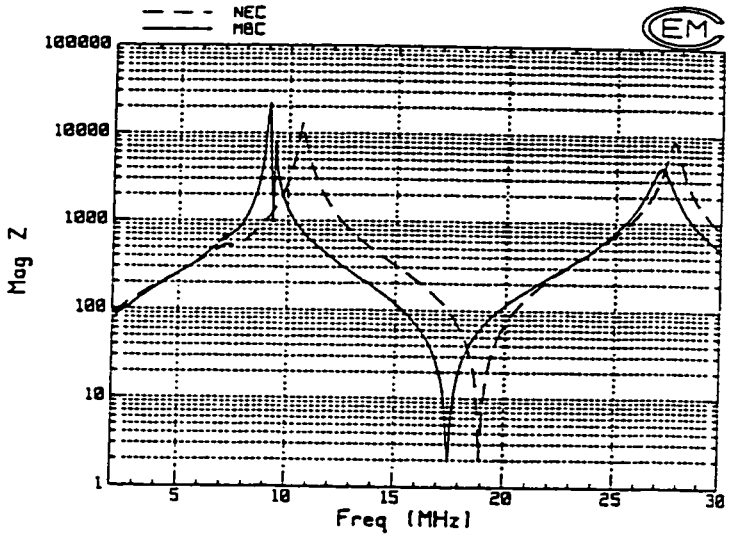

Figure 5.19: Impedance magnitude.

The results of the two codes match very closely in the band from 2.0 MHz to around 7.0 MHz and then between 22.0 MHz and 30.0 MHz, with very little difference between the two sets of results. The rest of the sweeps display an apparent frequency shift, but the trends and levels of the results are similar.

The resonant peaks in the power plots for the two sets of results are shifted approximately 1.5MHz from each other. Similarly, the impedance curves illustrate

a similar shift, though the MBC curve experiences some oscillation around 10 MHz. The impedance curves also highlight one of the concerns which prompted this study, namely the negative resistance calculated by the NEC code in the frequency range between 17 and 21 MHz. The negative impedance is a known problem occurring with NEC and requires further segmentation around the source of the antenna.

Radiation Pattern

The following section contains the comparison of the radiation patterns generated by the two codes. Several frequencies are presented to illustrate the similarities and differences in the patterns throughout the frequency sweep.

As the results of the frequency sweep have shown, the results at the lower frequencies match very well. The radiation pattern for the frequency of 7.0 MHz, shown in Figure 5.20, confirms this as well demonstrating the near perfect match between the two solutions.

If we now examine a higher frequency, we can notice a substantial difference between each of the patterns. A frequency of 20.0 MHz is presented in Figure 5.21.

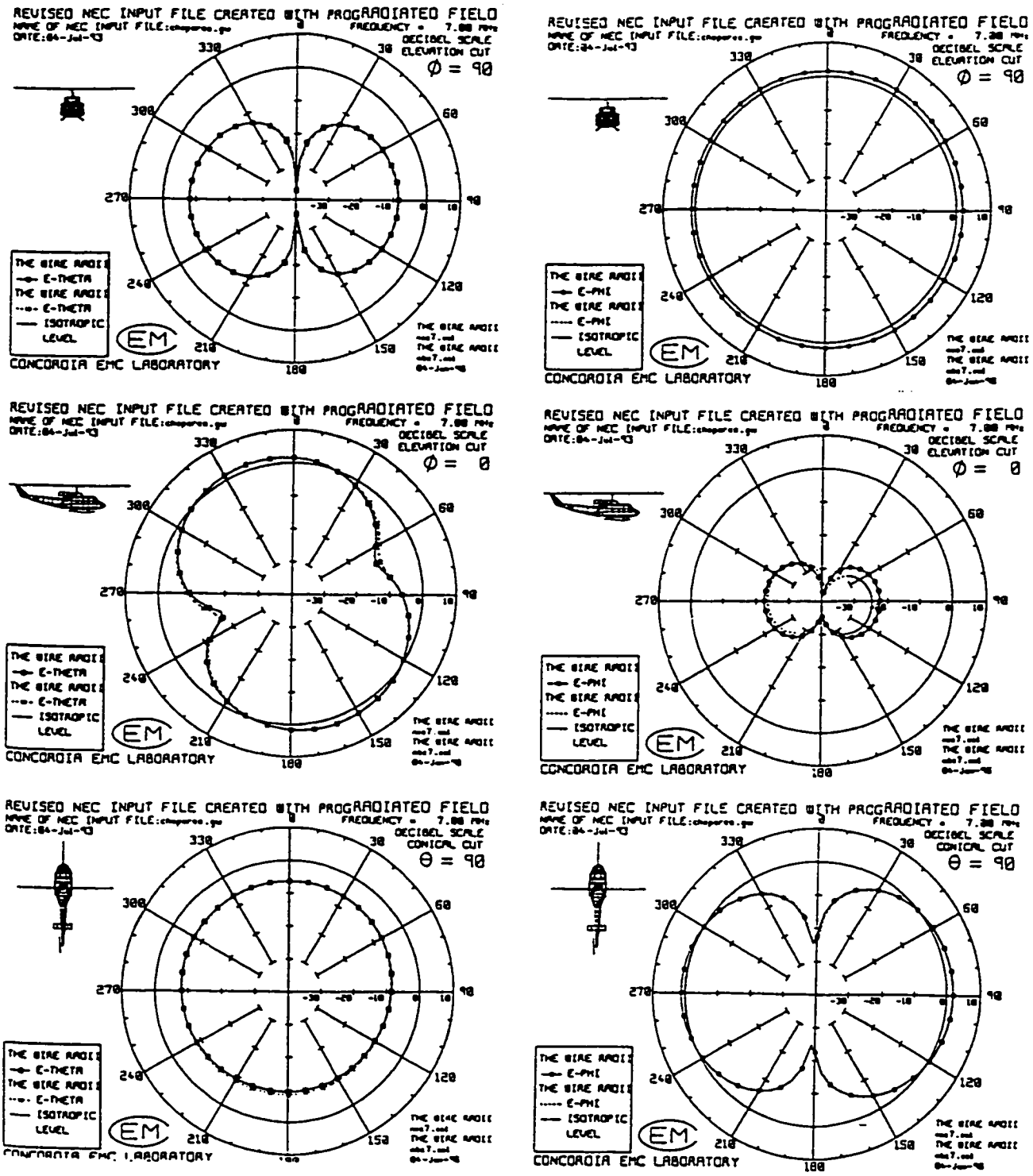

Figure 5.20: Roll, pitch and yaw plane E_θ and E_ϕ radiation patterns for 7.0 MHz, with NEC (-o-) and MBC (- -).

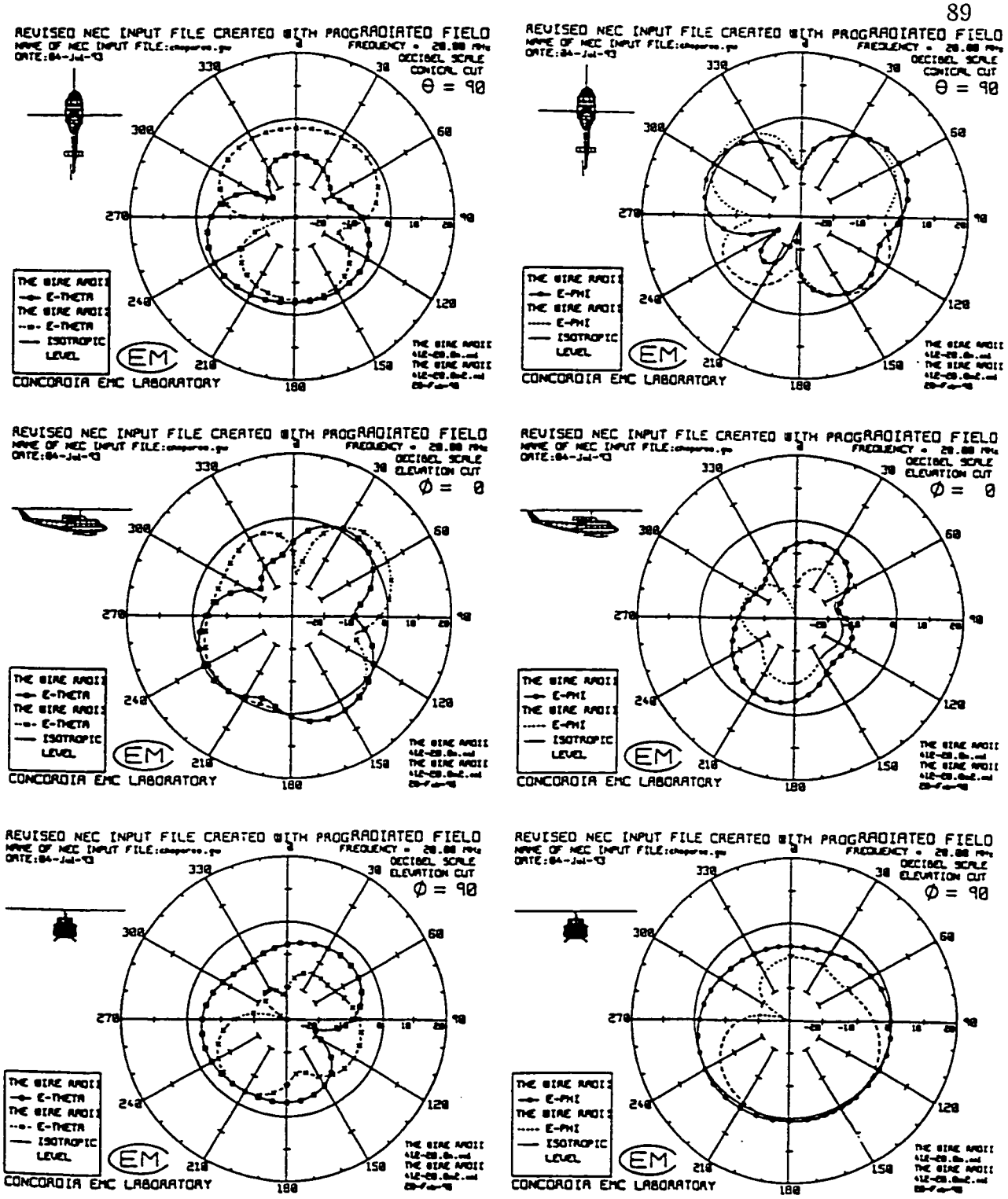

Figure 5.21: Roll, pitch and yaw plane E_θ and E_ϕ radiation patterns for 20.0 MHz, with NEC (-o-) and MBC (- -).

Current Distribution

As was the case with the previous results, the current distributions for the lower frequencies are very similar, as demonstrated by the results at a frequency of 7.0 MHz shown in Figure 5.22.

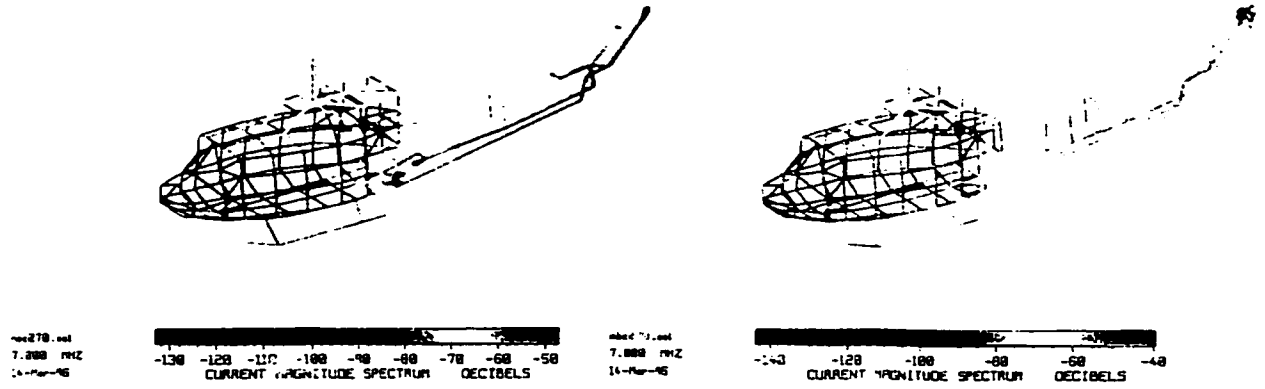

Figure 5.22: Current distribution of NEC (left) and MBC (right) results at 7.0 MHz.

As mentioned in Section 5.3.7 which illustrated a "hump" in the radiated power at 7 MHz indicating a resonant mode, this figure shows a high current flowing along the rotor blades. The rotor shaft is greatly illuminated (i.e. red) since all the current flowing to the rotor blades must pass through this path.

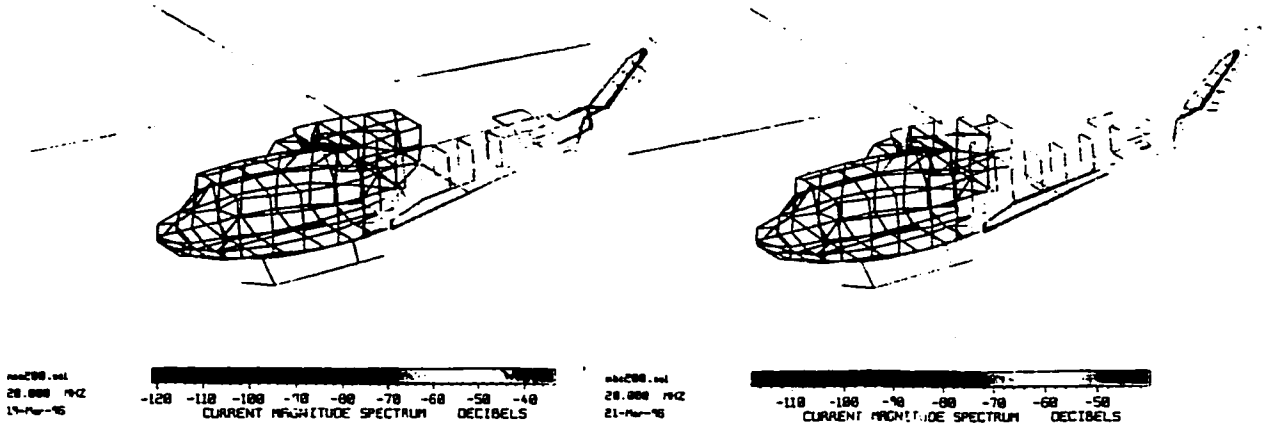

Figure 5.23: Current distribution of NEC (left)and MBC (right) results at 20.0 MHz.

The current distributions for the results at the higher frequency of 20 MHz are presented in Figure 5.23. Again the current distributions are very similar with similar behaviour appearing along the tail section as well as the current flowing near the antenna source at the base of the cabin.

However, when we examine the frequency sweep where one of the anomalies in the radiated power had occurred (refer to Section 5.3.7), such as around 2.6 MHz, a curious result is observed. The current distribution of the MBC results shows a very high current circulating in the tail section, a trait not shared in the NEC result. These results are presented in Figure 5.24.

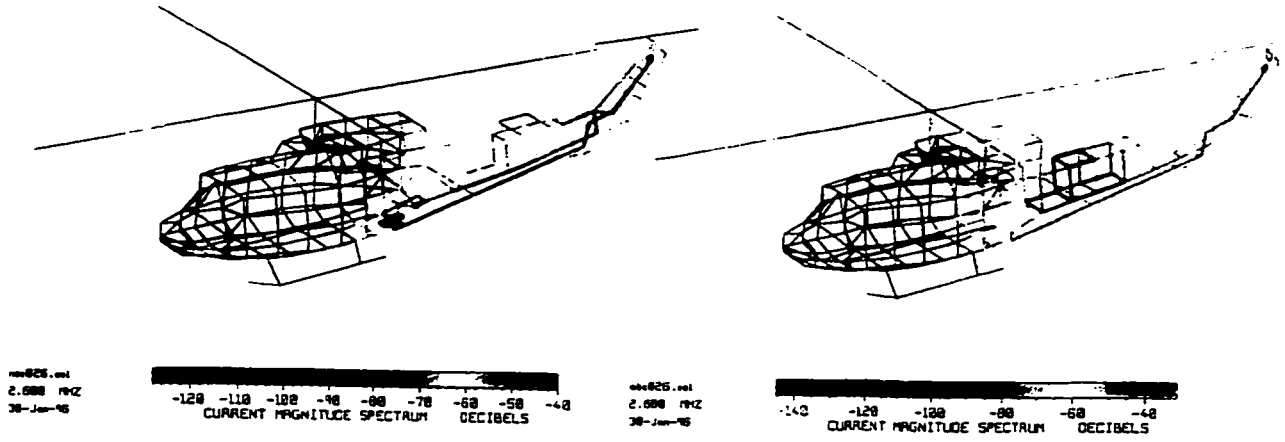

Figure 5.24: Current distribution of NEC (left) and MBC (right) results at 2.6 MHz.

What is curious about this result is that one of the factors that initiated this study was the phenomena of circulating currents being produced by the NEC code. This is visible in the triangular tail section near the rear rotor of the model, but does not appear to be as prevalent as the large loop current revealed in the MBC result.

This loop current was subsequently attributed to a problem in the implementation of two subroutines in the MBC code which were discovered as a result of further research into this anomaly[68].

Chapter 6

Conclusion

This thesis contains a comparison of electromagnetic problems using various solution techniques. The examination of some of the existing wire-grid modelling guidelines were explored as well as attempting to provide a guide to how close we may approach the "object under test" to yield reliable results.

The near field results obtained from a patch model are smoother than those of a wire grid model with the same segmentation size. It was observed however that good results can be obtained provided that the field points are $g/h = 2.5$ on the lit side, and $g/h = 1.25$ on the shadow side. Field points closer to the surface resulted in very similar anomalies, in both position and amplitude, in NEC and MBC. This result is interesting since their implementations are so different. NEC uses a sine and cosine basis function and point matching, while MBC uses piece-wise sinusoids and Galerkin's method.

Examination showed that the same surface rule in the plate and sphere near field demonstrated the best results most of the time. It worked for the tangential electric field of the plate and sphere as well as the normal field of the sphere, but not for the normal electric field on the plate. It was also observed that the normal electric field was less sensitive to violations of the same surface rule.

The far field tests for the plate and the sphere demonstrated that there was very little perceivable difference between the NEC and MBC results. The results of the

antenna mounted on the sphere resulted in excellent agreement with respect to the exact solution until the frequency became too high for the wire segment size. As the wavelength increases, the resulting radiation pattern resembles a small antenna over a ground plane with a bit of distortion due to the shape of the sphere.

The comparison of the helicopter model with the two different moment method code implementations produced results with good agreement, in general. Some interesting aspects surfaced including a frequency shifted peak in the radiated power, as well as some apparent glitches in the MBC impedance results arising from circulating currents in the tail section though subsequent research found the problem related to a code implementation problem. Further research into this topic could include performing measurements on a scale model or actual aircraft to allow a true evaluation of the results. This would be valuable since it could validate the results and provide a benchmark solution similar to that developed for the sphere comparisons.

Bibliography

[1] G. J. Burke and A. G. Poggio, "Numerical electromagnetics code (NEC) - Method of moments," Report UCID - 18834, Lawrence Livermore National Laboratory, 1981.

[2] M. A. Tilston and K. G. Balmain, "A multiradius, reciprocal implementation of the this wire moment method," IEEE Trans on Antennas and Propagation, pp. 1636-1644, Oct. 1990.

[3] J. H. Richmond, "A Wire-Grid Model for Scattering by Conducting Bodies," IEEE Transactions on Antennas and Propagation, vol. AP-14, November, 1966, pp. 782-786.

[4] M. Vainberg and K. G. Balmain, "On prediction of the asymmetry resonance phenomenon of log-periodic dipole antennas," Canadian Electrical Engineering Journal, vol. 6, no. 3, pp. 31-34, July 1981.

[5] C. M. Butler and D. R. Wilton, "Analysis of various numerical techniques applied to thin-wire scatterers," IEEE Trans on Antennas and Propagation, vol. AP-23, pp 534-540, July 1975.

[6] RCS Computer Program BRACT, Log-Periodic Scattering Array Program - II, MBAssociates Report No. MB-R69/46, Contract No. F04701-68-C-0188, 1969.

[7] J. H. Richmond, "Digital computer solutions of the rigorous equations for scattering problems," Proc. IEEE 53, pp. 796-804, 1965.

[8] Antenna Modeling Program - Engineering Manual, MBAssociates Report No. MB-R74/62, 1974.

[9] N. N. Wang, J. H. Richmond, and M. C. Gilreath, "Sinusoidal reaction formulation for radiation and scattering from conducting surfaces," IEEE Trans. on Antennas and Propagation, vol. AP-23, no. 3, pp. 376-382, May 1975.

[10] J. Singh and A. T. Adams, "A non-rectangular patch model for scattering from surfaces," IEEE Trans. on Antennas and Propagation, vol. AP-27, no. 4, pp. 531-535, July 1979.

[11] S. M. Rao, D. R. Wilton, and A. W. Glisson, "Electromagnetic scattering by surfaces of arbitrary shape," IEEE Trans. on Antennas and Propagation, vol. AP-30, no. 3, May 1982.

[12] W. L. Stutzman and G. A. Thiele, Antenna Theory and Design, New York, N. Y., John Wiley and Sons, 1981, pp. 6-17.

[13] M. Slater, "The Optimization of a Two-Monopole Broadside Array Using Reflectors With Variable Height and Spacing," Technical Report, Dept. of Electrical and Computer Engineering, September, 1994, p. 4.

[14] Balanis, "Antenna Theory: A Review," IEEE Transactions on Antennas and Propagation, Vol. 80, no. 1, January 1992, pp. 8,9.

[15] M. F. Iskander, Electromagnetic Fields and Waves, Prentice Hall, Englewood Cliffs, New Jersey, p. 450.

[16] Iskander, p. 445.

[17] Y. Bahsoun, "Evaluation of an HF Helicopter Antenna Measurements and Numerical Techniques," Master's Thesis, Faculty of Engineering and Computer Science, Concordia University, Montreal, Quebec, Canada, March 1982.

[18] Stutzman and Thiele, pp. 17–25.

[19] Q. C. Luu, "Numerical Techniques for the Study of HF Coupling Modes on Large Aircraft," Concordia University Thesis (M. A. Sc.), Dept. of Electrical and Computer Engineering, 1984, pp. 68, 69.

[20] C. A. Balanis, "Antenna Theory: A Review," Proc. IEEE, Vol. 80, No. 1 January 1992.

[21] D. M. Pozar, Microwave Engineering, Addison-Wesley Publishing Company Inc., Sept. 1993, p. 682.

[22] Stutzman and Thiele, pp. 63, 64.

[23] Bahsoun, p. 44.

[24] J. V. Granger,"System Consideration in Aircraft Antenna Design," I. R. E. Transaction on Airborne Electronics, vol. AE-1, December, 1951, pp. 1.2.

[25] Stutzman and Thiele, p. 47.

[26] Bahsoun, p. 45

[27] S. J. Kubina, "Radiation Characteristics of Vehicle Mounted Antennas and Their Application to Comprehensive System Design," McGill University Thesis (Ph. D.), Montreal, August, 1972.

[28] S. G. Mikhlin, "Variational Methods in Mathematical Physics," New York, N. Y., Pergamon Press, 1964.

[29] B. G. Galerkin, "Rods and Plate, Series Occuring in Various Questions Concerning the Elastic Equilibrium of Rods and Plates," Engineer's Bulletin, No. 19, 1915, pp. 897-908.

[30] R. F. Harrington, "Field Computation by Moment Methods," New York, N. Y., MacMillan, 1968.

[31] Stutzman and Thiele, pp. 306-324.

[32] E. K. Miller and F. J. Deadrick, "Some computational aspects of thin-wire modeling" in Numerical and Asymptotic Techniques in Electromagnetics, 1975. Springer-Verlag.

[33] Burke and Poggio, 116, p. 3.

[34] Burke and Poggio, 116, pp. 1-6.

[35] S. Esfandiari, "Analysis of HF Antennas on a Helicopter by Scale-Model Measurements and Computer Modelling," Master's Thesis, Faculty of Engineering and Computer Science, Concordia University, Montreal, Quebec, Canada, March 1992. p. 116.

[36] Bahsoun, p. 68,69.

[37] C. W. Trueman, "Wire-Grid Model Construction and Verification Using Programs MESHES, FNDRAD and CHECK," Concordia EMC Laboratory, June, 1990.

[38] Esfandiari, p. 21.

[39] K. S. H. Lee, L. Martin, and J. P. Castillo, "Limitations of Wire Grid Modelling of a Closed Surface," IEEE Trans. on Electromagnetic Compatibility, Vol. EMC-18, No. 3, pp. 123-129, August 1976.

[40] A. C. Ludwig,"Wire Grid Modeling of Surfaces," IEEE Trans. on Antennas and Propagation, Vol. AP-35, pp. 1045-1048, Sept. 1987.

[41] R. Paknys, "The Near Field of a Wire Grid Model," IEEE Trans. on Antennas and Propagation, Vol. 39, No. 7, pp. 994-999, July 1991.

[42] Richmond, pp. 1-4.

[43] Burke and Poggio, p. 6.

[44] Burke and Poggio, pp. 1-6.

[45] Esfandiari, p.42.

[46] Esfandiari, p.50.

[47] C. W. Trueman, S. J. Kubina, "The Calculation of Radar Cross-Section in the HF Band by Wire-Grid Modelling," Technical Note No. TN-EMC-90-01, EMC Laboratory, Concordia University, April 1990, pp. 118-121.

[48] C. W. Trueman and S. J. Kubina, "RCS of Fundamental Scatterers in the HF Band by Wire-Grid Modelling," Canadian Conference on Electrical and Computer Engineering, Ottawa, Sept. 4-6, 1990.

[49] S. R. Mishra, C. L. Larose, M. Flynn and C. W. Trueman, "A Database of Measured Data for RCS Code Validation," 10th Annual Review of Progress in Applied Computational Electromagnetics Society, Monterey, CA, March 21-26, 1994.

[50] D. Davis, Thin-Wire Viewer, EMC Laboratory, Concordia University, Montreal, Quebec, Canada.

[51] R. Paknys and L. R. Raschkowan, "Moment Method Surface Patch and Wire Grid Accuracy in the Computation of Near Fields," ACES journal, Volume 12, No. 3, November, 1997, pp. 16-25.

[52] S. U. Hwu and D. R. Wilton, "Electromagnetic scattering and radiation by arbitrary configurations of conducting bodies and wires," Applied Electromagnetic Laboratory, University of Houston Dept. of Electrical Engineering Tech. Rept 87-17, May 23, 1998.

[53] R. J. Marhefka and W. D. Burnside, "Numerical Electromagnetic Code - Basic Scattering Code (version 2), part 1: User's Manual," Department of Electrical Engineering, The Ohio State University ElectroScience Laboratory, Tech. Report., prepared under Contract N00123-79-C-1469 for Naval Regional Contracting Office, 712242-14, Dec. 1982.

[54] C. A. Balanis, "Advanced Engineering Electromagnetics," pp.651, John Wiley & Sons, 1989.

[55] R. Harrington, "Time-Harmonic Electromagnetic Fields," pp.293-298. McGraw-Hill, 1961.

[56] C. A. Balanis, "Advanced Engineering Electromagnetics," pp.650-656, John Wiley & Sons, 1989.

[57] R. Harrington, p.269.

[58] R. Paknys, Computer Program "sph_nf.for," Concordia University, Montreal, Canada, June 1996.

[59] R. Harrington, pp.298-299.

[60] Balanis, pp.323-325.

[61] R. S. Elliott, "Antenna Theory and Design," pp. 38-41, Prentice Hall, Englewood Cliffs, N. J. , 1981

[62] Canadair, "Global Express User Manual," Canada, 1996

[63] J. V. N. Granger, and J. T. Bolljahn, "Aircraft Antennas," Proceedings of the I. R. E., Vol. 43., pp 533-50, May 1955.

[64] J. V. N. Granger, and T. Morita, "Radio-Frequency Current Distributions on Aircraft Structures," Proceedings of the I. R. E., Vol. 43., pp 932-938, August 1951.

[65] S. J. Kubina, and T. J. F. Pavlasek, "Evaluation of HF Antenna for Helicopters and Small Aircraft," International Conference on Antennas for Aircraft and Spacecraft, pp. 165-170, Institution of Electrical Engineers, Savoy Place, London WC2, 3-5 June 1975.

[66] C. L. Larose, "Advances in Wire-Grid Modelling of Antennas and Auxiliary Computer Graphics Systems with the CP-140 Case Study," Master's Thesis, Faculty of Engineering and Computer Science, Concordia University, Montreal, Quebec, Canada

[67] B. R. Rosenzweig, "Numerical Modelling of EC-130 Airframe and Antenna Installation for Prediction of Radiation Characteristics over the HF Band." Master's Thesis, Faculty of Engineering and Computer Science, Concordia University, Montreal, Quebec, Canada.

[68] S. J. Kubina, private conversations regarding subsequent research at the EMC Laboratory and detailing Tilston's update to MBC subroutines, Concordia University, Montreal, Quebec, Canada, 1999.

Appendix A

Related ACES Journal Paper and Errata

This Appendix contains a copy of the report "Moment Method Surface Patch and Wire Grid Accuracy in the Computation of Near Fields" written by R. Paknys and L. R. Raschkowan, and published in the Applied Computational Electromagnetics Society Journal in November 1997.

The following errors were included in the original publication and are addressed in this section.

On page 17, the middle sentence of Section 2-A should have stated:
Fig. 2 show the tangential field E_x and the normal field E_z at $z = \pm 0.04$.

On page 18, the middle sentence of Section 2-B should have stated:
An increased grid size of $g = 0.25$ m at 300 MHz was also tried, and anomalies of comparable magnitude were obtained at $z = 0.1$ on the lit side and $z = -0.2$ on the shadow side.

On page 21, the last sentence of Section 3 should have stated:
The frequency was chosen as 5.12 MHz so that $ka = 1.6$ and $g = 0.1\lambda$.

THE APPLIED COMPUTATIONAL ELECTROMAGNETICS SOCIETY JOURNAL

Vol. 12 No. 3 November 1997

TABLE OF CONTENTS

Moment Method Surface Patch and Wire Grid Accuracy in the Computation of Near Fields

Robert Paknys and Leslie R. Raschkowan

Department of Electrical and Computer Engineering
Concordia University, Montreal, PQ, Canada H3G-1M8
E-mail: paknys@ece.concordia.ca

Abstract—**The accuracy of surface patch and wire grid moment method models for the computation of near fields is investigated. A sphere and a flat plate with plane wave illumination are examined.**

It is found that wire grids exhibit stronger near field anomalies than surface patches, which have the current more distributed over the surface. Nevertheless, good results can be obtained with a wire grid, provided that a small distance from the wire grid surface is maintained.

The surface patch results are obtained using the *Junction* code. Wire grid results are obtained with both the *MBC* and *NEC* codes. Validation for the sphere is by comparison with an exact solution, and validation for the plate is by comparison with a high frequency UTD solution obtained from the *NECBSC* code.

1 Introduction

The near field close to the surface of a complex shape is of great interest in antennas and electromagnetic compatibility. For example, the radiation characteristics of an aircraft antenna are distorted by the fuselage on which the antennas are mounted. Another example is in the assessment of electromagnetic hazards to personnel and equipment on the deck of a ship, in the presence of strong RF and microwave sources.

The method of moments is a suitable methodology for the calculation of fields scattered by bodies of resonant size and smaller. Numerous codes exist, and assessment of their accuracy for the computation of electromagnetic fields has been a topic of ongoing research for many years. Historically, wire grid models were the first methodology which permitted moment method modeling of scattering by complex shapes. Richmond's *Thin Wire* code [1] was a pioneering effort in this direction. His code was later extended significantly by Tilston and Balmain as the *Multiradius Bridge Current MBC* code [2]. The *Numerical Electromagnetic Code NEC* was developed by Burke et al. [3]. The development of surface patch codes such as *Patch* by Rao et al. [4], *Junction* by Hwu et al. [5], the *Electromagnetic Surface Patch Code ESP*, by Newman [6], and others, have further expanded the applicability of the moment method.

For smooth bodies without sharp edges, surface patches can accurately model the surface current. On the other hand, wire grids can also be useful, as an edge current can be more accurately handled by a wire than a patch. A patch cannot represent the current at the patch edge, so a separate "edge mode" is required. Inclusion of edge modes have been shown to enhance the accuracy [7], though their incorporation into a general purpose code is not straightforward. Another reason for using wires is that if open bodies are modeled with NEC, we must use a wire grid model, as its MFIE based patch model is only appropriate for closed bodies.

Although much work has been done on the validation of wire grids and patches for far field calculations, investigations into the near field are relatively scarce. Ludwig [8] examined a 2-D TM polarized wire grid model of a cylinder and found that

though the tangential field is not accurate between the wires, the far field is accurate, provided that the "same surface rule" is met, i.e. that the total surface area of the wires equals the surface area of the true surface being modeled. Later, Paknys [9] extended Ludwig's work and demonstrated that the same surface rule is also optimum for the near field of a 2-D TM cylinder. Other work has examined the use of surface patches in near field computations. Yang et al. [10] examined a 2-D cylinder and demonstrated the equivalence of pulse basis patch currents and filamentary wire currents, provided that the same surface rule is used. Kashyap and Louie [11] compared the surface currents of plates made of either wire grids or patches, and found that the edge wires have to be made thinner to obtain agreement with a patch model. Burton et al. [12] also used a patch model to study near fields. They constructed a sufficiently detailed model that enabled one to examine the leakage through gaps in a door on a closed box. Kemptner [13] computed the near fields of a metallic cube and an airplane, using a patch formulaton. His results for a cube agreed well with the measured surface current and electric field.

This paper is an investigation into the accuracy of near zone tangential and normal electric fields for 3-D bodies, as computed from surface patch and wire grid models. A square plate and a sphere with plane wave illumination are used as test cases. The accuracy of the patch models are compared to a UTD solution for the plate, and an exact solution for the sphere. For the wire grid models, the same surface rule and the extent of near field anomalies are investigated.

Section 2 examines the near fields of the plate. Section 3 examines the near fields of the sphere. Section 4 compares two different moment method wire codes, MBC and NEC. Section 5 contains the conclusions.

2 Near Field of the Plate

The square plate is 1 × 1 m in size and lies in the $x-y$ plane with the origin at the center of the plate. A wire grid model that has a grid size $g = 0.1$ m is shown in Fig. 1. The wire radius is $a_w = 0.0145$ m, in accordance with the same surface rule. The surface

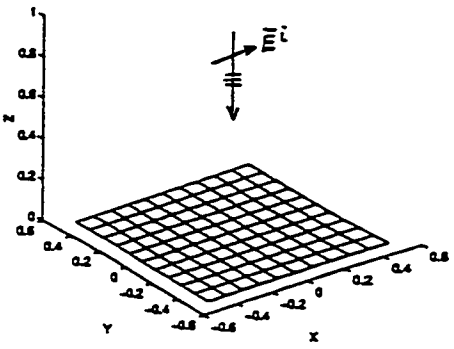

Figure 1: Wire grid model for the 1 × 1 m plate. An $\hat{x}$ polarized plane wave of 1 V/m is normally incident from above. The field point is in the $y = 0$ plane.

patch model is similar, except that each square area is divided into two triangular patches.

The incident field on the plate is a plane wave with an amplitude of 1 V/m, polarized in the $\hat{x}$ direction and traveling in the $-z$ direction, i.e. $\vec{E}^{inc} = \hat{x}e^{jkz}$. The field point is in the $y = 0$ plane. The near field was calculated for several cases, and the total field $\vec{E} = \vec{E}^{inc} + \vec{E}^{scatt}$ was plotted, using a reference level of 0 dB = 1 V/m. Unless otherwise specified, the frequency is 300 MHz so that $g = 0.1\lambda$.

A. Junction and UTD Models for the Plate

The scattering by a plate does not have an exact solution, so results from the UTD based BSC code [14] were compared with the Junction MM patch code, to establish confidence in the patch model. Fig. 2 shows the tangential field E_x and the normal field E_z at $z = \pm 0.04$.[1] The agreement is within 1.2 dB for E_x for all values of x along the plate. The agreement is also within 1.2 dB for E_z near the plate, but gets worse beyond the plate edges where $|x| \geq 0.5$. The reason for this is unknown, but it is speculated that further improvements could be obtained by the inclusion of multiple diffraction effects in the UTD

[1] $|E_z|$ is the same on both sides of the plate so $z \leq 0$ is not shown.

Typo: $z = \pm 0.04$

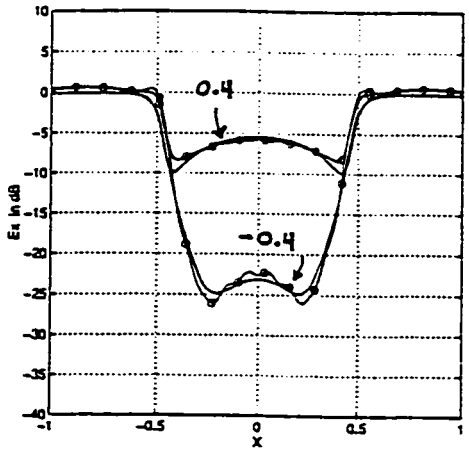

(a)

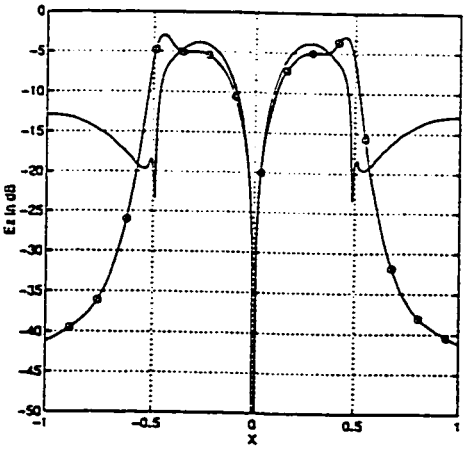

(b)

Figure 2: Comparison of UTD (—) and Junction (ooo) for the plate, with patch size $g = 0.1\lambda$. (a) E_x, $z/g = \pm 0.4$ (b) E_z, $z/g = 0.4$. The field point is in the $y = 0$ plane.

model, and possibly reduced patch size in the patch model. We chose Junction for the subsequent plate model validations.

B. Extent of the Near Field Anomalies

The near field of the wire grid plate was calculated with NEC and compared to Junction. A frequency of 300 MHz and $g = 0.1\lambda$ was used. Fig. 3 shows the near field at a distance of $z/g = \pm 0.4$ and $z/g = \pm 0.8$. At $z/g = 0.4$, the anomalies in E_x and E_z are of comparable magnitude. For E_x, the onset of anomalies occurs at about $z/g = 0.4$ on the lit side, and $z/g = -0.8$ on the shadow side. An increased grid size of $g = 0.25$ m at 300 MHz was also tried, and anomalies of comparable magnitude were obtained at $z/g = 0.1$ on the lit side and $z/g = -0.2$ on the shadow side. This suggests that the onset of anomalies for flat plate structures occurs when $z/g \approx 0.4$ on the lit side, and $|z|/g \approx 0.8$ on the shadow side.

The results in Fig. 3 show that for a given observer height, the wire grid results are not as smooth as those obtained in Fig. 2 using Junction. It was found that anomalies of comparable magnitude could also be observed using Junction, but only for field points much closer to the surface.

C. Test of the Same Surface Rule

It is widely accepted that the same surface rule gives the best result for the field radiated by a wire grid model. To test this assertion, NEC was used to compute the near field for several wire radii, and compared to Junction. The frequency was 300 MHz with $g = 0.1\lambda$. The field points were chosen as close as possible to the plate, but not so close that the anomalies might obscure the results.

Figs. 4a, b show the tangential field E_x at $z/g = \pm 0.8$ and Fig. 4c the normal field E_z at $z/g = 0.8$. It is interesting to note that the same surface rule gives the best result for E_x but not for E_z. Hence, it is not possible to choose a wire radius that is simultaneously optimum for both the tangential and normal field components. It is also noted that E_x is more sensitive to the wire radius than E_z.

Fig. 4 also shows that E_x on the shadow side is more sensitive to wire radius changes than on the

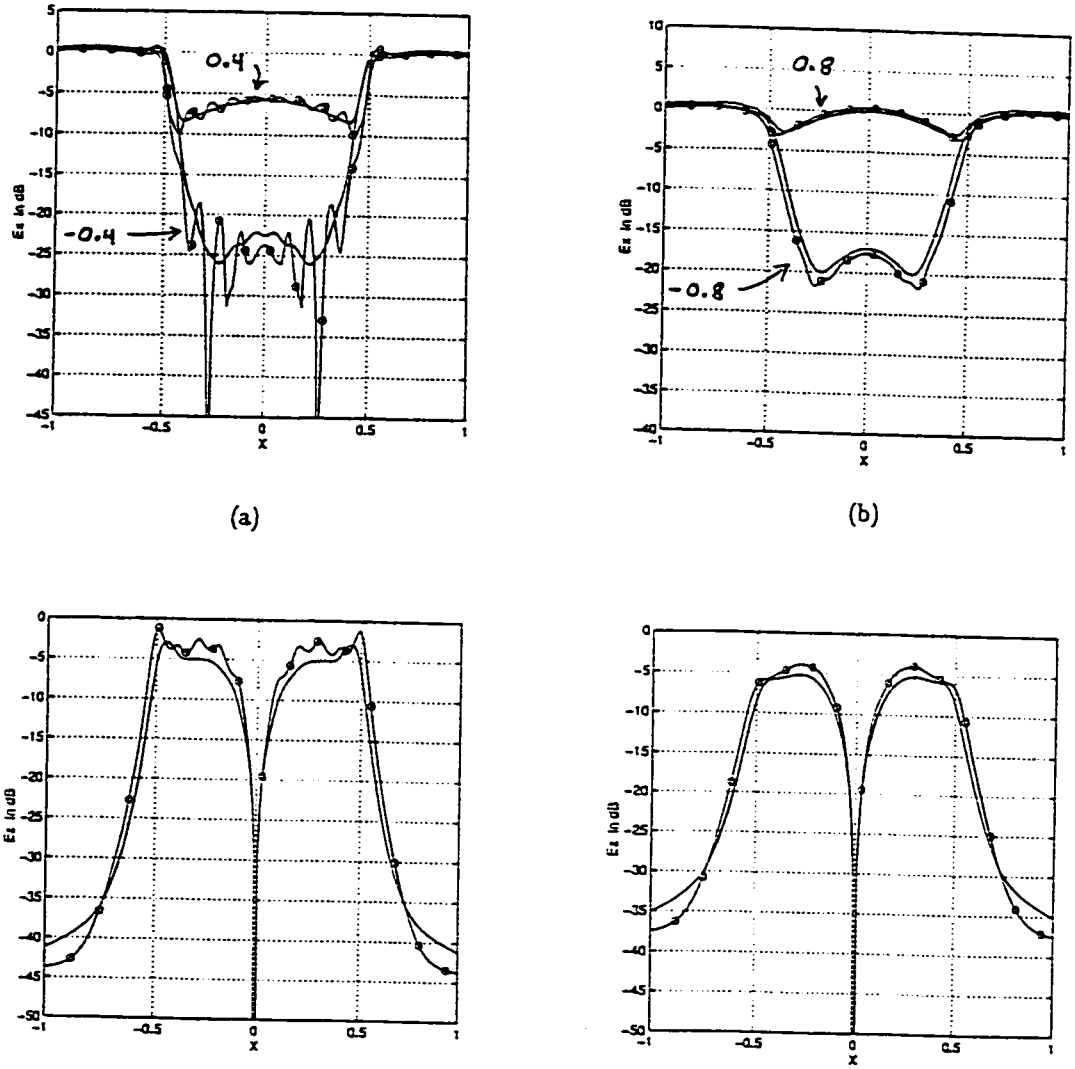

Figure 3: Near field of the plate with grid size $g = 0.1\lambda$. Comparison of NEC wire grid (ooo) and Junction surface patches (—). (a) E_x, $z/g = \pm 0.4$ (b) E_x, $z/g = \pm 0.8$ (c) E_z, $z/g = 0.4$ (d) E_z, $z/g = 0.8$. The field point is in the $y = 0$ plane.

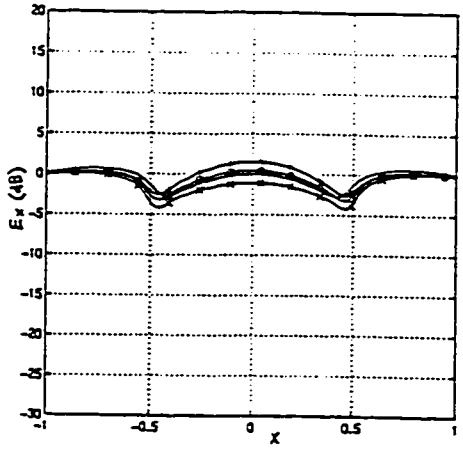

(a)

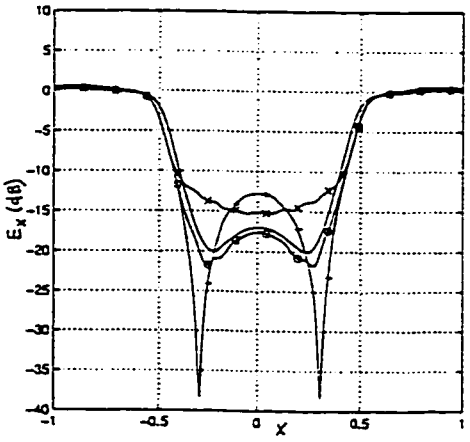

(b)

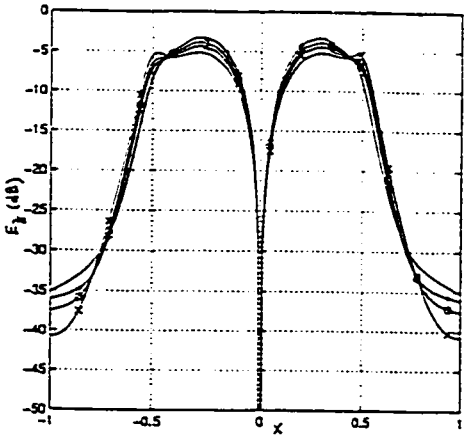

(c)

Figure 4: Effect of wire radius on the near field of the plate, with grid size $g = 0.1\lambda$. The wire radius that satisfies the same surface rule is a_w=0.0145 m. Using NEC, with a_w (ooo), $a_w/2$ (+++), $2a_w$ (xxx). Comparison is with Junction (—). (a) E_z, $z/g = 0.8$ (b) E_z, $z/g = -0.8$ (c) E_z, $z/g = 0.8$. The field point is in the $y = 0$ plane.

lit side. This is probably because the accuracy of E^{scatt} on the shadow side is more critical, as E^{scatt} must cancel E^{inc} in order to accurately predict the low field level on the shadow side of the plate. E^{scatt} was examined separately, and was found to be much less sensitive to wire radius changes than the total field $E^{inc} + E^{scatt}$.

A higher frequency of 750 MHz was also tried. The corresponding grid size in this case is 0.25λ. The results were still good, with typical errors of 2 dB or less. The sensitivity with respect to wire radius was increased for E_x, in the shadow. The sensitivity of E_z remained relatively weak.

D. Field Between the Wires

The previous results were taken along $y = 0$, which happens to be above a wire. To see what happens in other situations, a contour plot in the $x-y$ plane was generated, from which some qualitative observations could be made. Also, to obtain a quantitative comparison, a cut along $y = g/2$, which is in between the wires, was used. The heights used were the same as before, i.e. $z/g = \pm 0.4$ and $z/g = \pm 0.8$.

It was found that very little changed with respect to the peak to peak amplitude of the near field anomalies. The average field level changed only slightly. By comparing the $y = 0$ and $y = g/2$ cases it was found that with $y = g/2$, E_x increased by 0.7 dB, and E_z decreased by 1.3 dB. This seems correct, as the wire tends to short out E_x and support the surface charge that is associated with E_z.

3 Near Field of the Sphere

The wire grid sphere is shown in Fig. 5. The surface patch model is similar, except that each quadrilateral area is divided into two triangular patches. The sphere is centered at the origin, and its radius is $a = 15$ m. The wire spacing is $\Delta\theta = \Delta\phi = \pi/8$. At the equator the grid size is $g = 5.853$ m and the wire radius is $a_w = 0.9128$ m. Near the poles the grid size is smaller and the wire radii are adjusted in accordance with the same surface rule.

The incident field is a plane wave with an amplitude of 1 V/m, polarized in the $\hat{y}$ direction and traveling in the $+x$ direction. It is given by $\vec{E}^{inc} = \hat{y}e^{-jkx}$. In all cases the total field $\vec{E} = \vec{E}^{inc} + \vec{E}^{scatt}$

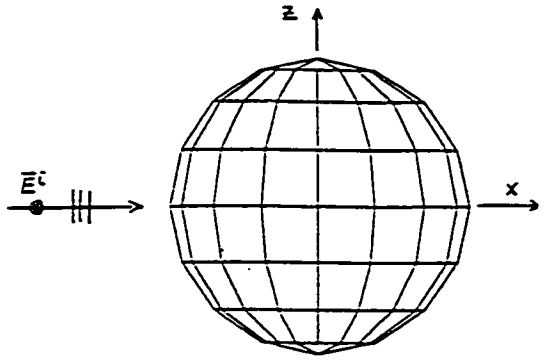

Figure 5: Wire grid model for the sphere. The radius is 15 m. A $\hat{y}$ polarized plane wave of 1 V/m is incident, travelling along $+x$. The field point is at a height h above the surface, at the equator where $\theta = 90°$ and $0 \leq \phi \leq 360°$.

is plotted, using a reference of 0 dB = 1 V/m. The field point is at a height h above the surface, at the equator where $\theta = 90°$ and $0 \leq \phi \leq 360°$. The frequency was chosen as 12.8 MHz so that ka =1.6 and $g = 0.1\lambda$.

A. Junction and Exact Solution for the Sphere

The Junction surface patch model of the sphere was evaluated by comparison with an exact solution obtained from an eigenfunction series [15]. The field was calculated at a height of $h = 2.34$ m off the surface, so that $h/g = 0.4$. The agreement was so close as to be almost indistinguishable, suggesting that Junction is highly suitable for the computation of the near field of a smooth body. As a reference solution, the eigenfunction series was used in the subsequent validations.

B. Extent of the Near Field Anomalies

The field was calculated with NEC, at heights of $h = 2.34$ m and 4.68 m off the surface, so that $h/g = 0.4$ and 0.8, respectively. Fig. 6 shows that for $h/g = 0.4$, on the lit side, the anomalies in E_ϕ

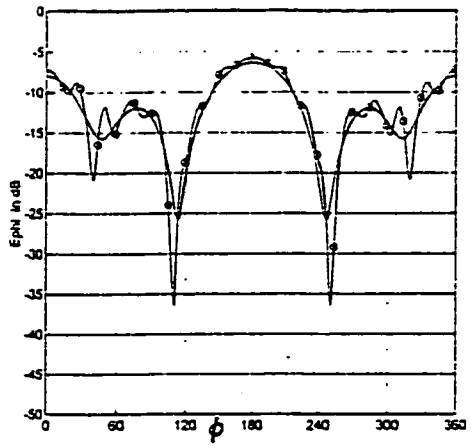

(a)

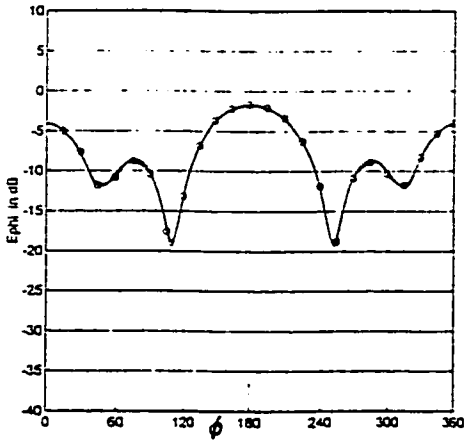

(b)

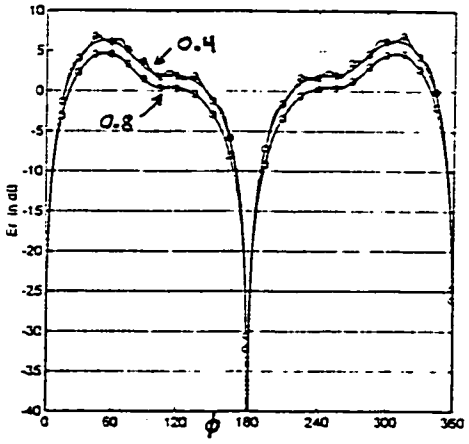

(c)

Figure 6: Near field of the sphere, grid size $g = 0.1\lambda$. Comparison of NEC wire grid (ooo) and exact solution (—). (a) E_ϕ, $h/g = 0.4$ (b) E_ϕ, $h/g = 0.8$ (c) E_r, $h/g = 0.4$ and 0.8.

and E_r are of comparable magnitude. For E_ϕ, the onset of anomalies occurs at about $h/g = 0.4$ on the lit side, and $h/g = -0.8$ on the shadow side. Similar behavior was noted for the plate, so these aspects appear to be independent of the precise shape of the scattering body.

A higher frequency was also tried. Using $ka = 4$ and $g = 0.25\lambda$, excellent agreement with the exact solution was observed, and we found that $h/g \geq 0.8$ was still a good criterion for avoiding anomalies.

C. Test of the Same Surface Rule

The field was calculated with NEC at a height of $h = 4.68$ m off the surface, so that $h/g = 0.8$. In Fig. 7 we see that the same surface rule gives the best result for both E_ϕ and E_r. The cases of too thick wires ($2a_w$) and too thin wires ($a_w/2$) straddle the exact result. (The case using the same surface rule was not plotted, as it is indistinguishable from the exact solution.) This is unlike the plate, where the same surface rule worked for the tangential field, but not for the normal field.

The tangential E for the sphere was much less sensitive to wire radius changes than the plate. This is not because of the shape, but because the field in the shadow of the plate is much lower. As already mentioned in Section 2 C, errors in the scattered field are more evident when the incident and scattered fields are supposed to be cancelling.

The internal field of a closed body is known to be a sensitive indicator of the quality of a moment method solution, as cancellation of the incident field must take place inside the scatterer. This was not explored here, as there is no corresponding test that can be used for the plate.

A higher frequency using $ka = 4$ and $g = 0.25\lambda$ was also tried. It was found that the sensitivity with respect to wire radius of E_ϕ was increased on the shadow side, and hardly affected on the lit side. The sensitivity of E_r remained relatively weak. Even at this higher frequency, the results remained good, with errors on the order of 1 dB or less when the same surface rule was obeyed.

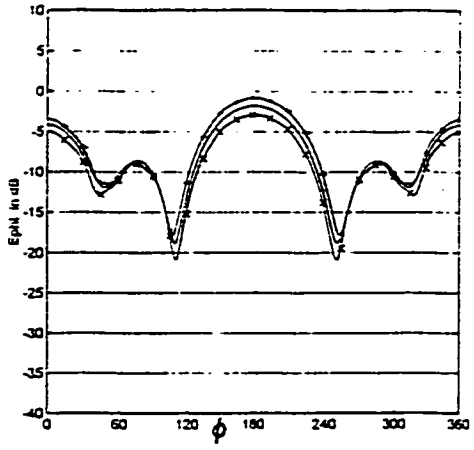

(a)

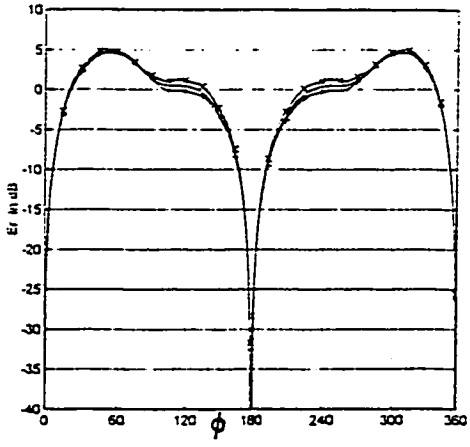

(b)

Figure 7: Effect of wire radius on the near field of the sphere, with grid size $g = 0.1\lambda$ and $h/g = 0.8$. The wire radius that satisfies the same surface rule is a_w=0.9128 m. Using NEC with $a_w/2$ (+++), $2a_w$ (xxx). Comparison is with exact solution (—). (a) E_ϕ (b) E_r.

4 Comparison of NEC and MBC

The NEC and MBC wire codes were used to compute the near field of the sphere at $h/g = 0.4$. Fig. 8 shows that the positions and amplitudes of the anomalies are very similar. This is noteworthy, as the two codes are quite different, i.e. NEC uses sine and cosine basis functions with point matching, whereas MBC uses piecewise sinusoids and Galerkin's method. Other tests using MBC revealed that the extent of near field anomalies and the dependence on wire radius were very similar to NEC. Hence, the comments made in previous sections with regard to the NEC wire grid models would seem to apply to MBC as well. The square plate was also tried, and similar near field behavior was found using both codes.

5 Conclusion

The near field of a surface patch model is smoother than for a wire grid with the same segmentation size. Nevertheless, a wire grid was found to give good results when the observer is a small distance h off the surface, provided that $h/g \geq 0.4$ on the lit side, and $h/g \geq 0.8$ on the shadow side. This was found to be true for both the plate and the sphere, and was tested for several grid sizes and frequencies.

Use of the same surface rule gives the best result for the near fields most of the time but not all of the time. It worked for the tangential E for the plate and sphere, for the normal E on the sphere, but not for the normal E on the plate.

The tangential E was more sensitive than the normal E with respect to wire radius, and the greatest errors occured in the tangential component when the same surface rule was violated. The greatest sensitivity occured with the field point in the deep shadow, where the incident and scattered fields are supposed to cancel. On the lit side, the effect of changing the wire radius was much smaller.

The type of MM formulation used in the wire codes was not a major factor, as similar results were obtained from the NEC code and MBC code.

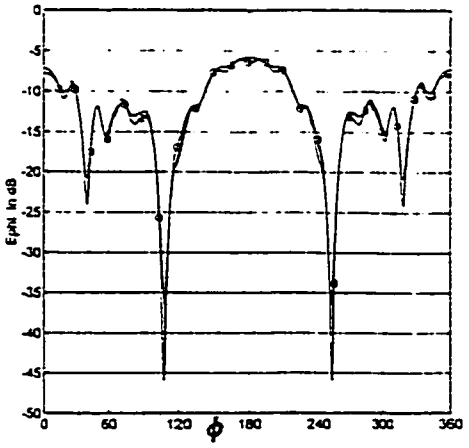

(a)

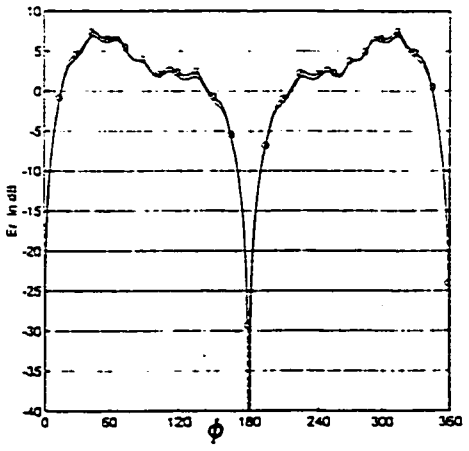

(b)

Figure 8: Comparison of NEC (—) and MBC (ooo) for the sphere, with grid size $g = 0.1\lambda$ and $h/g = 0.4$. (a) E_ϕ (b) E_r.

Acknowledgment

This work was partially supported by the National Science and Engineering Research Council of Canada, grant OGP0046227.

Thanks to Mr. Jim Logan of NRAD(NOSC) for helping to make the *Junction* and *NECBSC* codes available to the Concordia University EMC Laboratory, and to Drs. Don Wilton and Ron Marhefka for supplying them to us through the established channels.

References

[1] J.H. Richmond, "Radiation and scattering by thin wire structures in a homogeneous conducting medium ," IEEE Trans. on Antennas and Propagat., p.365, Mar. 1974.

[2] M.A. Tilston and K.G. Balmain, "A multiradius, reciprocal implementation of the thin wire moment method," IEEE Trans. on Antennas and Propagat., pp.1636–1644, Oct. 1990. Code description and ordering information: IEEE AP-S Magazine, p.61, Oct. 1991.

[3] G.J. Burke and A.J. Poggio, "Numerical Electromagnetic Code," Technical Document 116, Naval Electronic Systems Command, 18 Jul. 1977.

[4] S.M. Rao, D.R. Wilton, and A.W. Glisson, "Electromagnetic scattering by surfaces of arbitrary shape," IEEE Trans. on Antennas and Propagat., pp.409–418, May 1982.

[5] S.U. Hwu and D.R. Wilton, "Electromagnetic scattering and radiation by arbitrary configurations of conducting bodies and wires," Applied Electromagnetics Laboratory, University of Houston Dept. of Electrical Engineering Tech. Rept. 87–17, May 23, 1988.

[6] E.H. Newman, "A user's manual for electromagnetic surface patch code ESP," Department of Electrical Engineering, The Ohio State University ElectroScience Laboratory, Tech. Rep., prepared under Contract DAAG29–81–K–0020 for U.S. Army Research Office, 713402–1, Jul. 1981.

[7] J.H. Richmond, "On the edge mode in the theory of TM scattering by a strip or grating," IEEE Trans. on Antennas and Propagat., pp.883–887, Nov. 1980.

[8] A.C. Ludwig, "Wire grid modeling of surfaces," IEEE Trans. on Antennas and Propagat., pp.1045–1048, Sept. 1987.

[9] R. Paknys, "The near field of a wire grid model," IEEE Trans. on Antennas and Propagat., pp.994–999, Jul. 1991.

[10] X.H. Yang, L. Shafai, and A. Sebak, "A comparison study on wire grid model and point matching technique with subdomain basis functions," ANTEM Symposium on Antenna Technology and Applied Electromagnetics, Winnipeg Manitoba, Conference Proceedings pp.656–661, Aug. 5–7, 1992.

[11] S. Kashyap and A. Louie, "Surface modelling for EM interaction analysis," ACES Journal, Vol.6 No.2, pp.38–52, Winter 1991.

[12] M. Burton, A. Louie, S. Kashyap and R. Banik, "Penetration of the field of an HF antenna into ammunition lockers on a ship," IEEE International EMC Symposium Digest, pp.46–47, Aug. 9–13, 1993.

[13] E. Kemptner, "Determination of lines of constant phase in the near field of a metallic cube and an airplane," IEEE Trans. on Antennas and Propagat., pp.897–904, Jul. 1994.

[14] R.J. Marhefka and W.D. Burnside, "Numerical electromagnetic code– Basic scattering code (version 2), part 1: User's manual ," Department of Electrical Engineering, The Ohio State University ElectroScience Laboratory, Tech. Rep., prepared under Contract N00123–79–C–1469 for Naval Regional Contracting Office, 712242–14, Dec. 1982.

[15] R.F. Harrington, *Time Harmonic Electromagnetic Fields*. New York: Mc Graw–Hill, 1961.

Appendix B

NEC input file format

This Appendix contains a NEC input file for a 1 x 1 metre plate.

```
CM REVISED NEC INPUT FILE CREATED WITH PROGRAM FNDRAD
CM
CM NAME OF NEC INPUT FILE:Plate.gw
CM
CM DATE:11-Nov-98
CM
CM THE WIRE RADII IN THIS FILE WERE CALCULATED WITH PROGRAM FNDRAD
CE
GW  1 1 -0.500 -0.5000 0.00 -0.500 -0.2500 0.00 0.03183
GW  2 1 -0.500 -0.2500 0.00 -0.500  0.0000 0.00 0.03183
GW  3 1 -0.500  0.0000 0.00 -0.500  0.2500 0.00 0.03183
GW  4 1 -0.500  0.2500 0.00 -0.500  0.5000 0.00 0.03183
GW  5 1 -0.250 -0.5000 0.00 -0.250 -0.2500 0.00 0.03183
GW  6 1 -0.250 -0.2500 0.00 -0.250  0.0000 0.00 0.03183
GW  7 1 -0.250  0.0000 0.00 -0.250  0.2500 0.00 0.03183
GW  8 1 -0.250  0.2500 0.00 -0.250  0.5000 0.00 0.03183
GW  9 1  0.000 -0.5000 0.00  0.000 -0.2500 0.00 0.03183
GW 10 1  0.000 -0.2500 0.00  0.000  0.0000 0.00 0.03183
GW 11 1  0.000  0.0000 0.00  0.000  0.2500 0.00 0.03183
GW 12 1  0.000  0.2500 0.00  0.000  0.5000 0.00 0.03183
GW 13 1  0.250 -0.5000 0.00  0.250 -0.2500 0.00 0.03183
GW 14 1  0.250 -0.2500 0.00  0.250  0.0000 0.00 0.03183
GW 15 1  0.250  0.0000 0.00  0.250  0.2500 0.00 0.03183
GW 16 1  0.250  0.2500 0.00  0.250  0.5000 0.00 0.03183
GW 17 1  0.500 -0.5000 0.00  0.500 -0.2500 0.00 0.03183
GW 18 1  0.500 -0.2500 0.00  0.500  0.0000 0.00 0.03183
GW 19 1  0.500  0.0000 0.00  0.500  0.2500 0.00 0.03183
GW 20 1  0.500  0.2500 0.00  0.500  0.5000 0.00 0.03183
GW 21 1 -0.500 -0.5000 0.00 -0.250 -0.5000 0.00 0.03183
GW 22 1 -0.250 -0.5000 0.00  0.000 -0.5000 0.00 0.03183
GW 23 1  0.000 -0.5000 0.00  0.250 -0.5000 0.00 0.03183
GW 24 1  0.250 -0.5000 0.00  0.500 -0.5000 0.00 0.03183
GW 25 1 -0.500 -0.2500 0.00 -0.250 -0.2500 0.00 0.03183
GW 26 1 -0.250 -0.2500 0.00  0.000 -0.2500 0.00 0.03183
GW 27 1  0.000 -0.2500 0.00  0.250 -0.2500 0.00 0.03183
GW 28 1  0.250 -0.2500 0.00  0.500 -0.2500 0.00 0.03183
GW 29 1 -0.500  0.0000 0.00 -0.250  0.0000 0.00 0.03183
GW 30 1 -0.250  0.0000 0.00  0.000  0.0000 0.00 0.03183
GW 31 1  0.000  0.0000 0.00  0.250  0.0000 0.00 0.03183
GW 32 1  0.250  0.0000 0.00  0.500  0.0000 0.00 0.03183
GW 33 1 -0.500  0.2500 0.00 -0.250  0.2500 0.00 0.03183
GW 34 1 -0.250  0.2500 0.00  0.000  0.2500 0.00 0.03183
GW 35 1  0.000  0.2500 0.00  0.250  0.2500 0.00 0.03183
GW 36 1  0.250  0.2500 0.00  0.500  0.2500 0.00 0.03183
GW 37 1 -0.500  0.5000 0.00 -0.250  0.5000 0.00 0.03183
GW 38 1 -0.250  0.5000 0.00  0.000  0.5000 0.00 0.03183
GW 39 1  0.000  0.5000 0.00  0.250  0.5000 0.00 0.03183
GW 40 1  0.250  0.5000 0.00  0.500  0.5000 0.00 0.03183
GE
EK
FR  0 1  3.000  0.0
EX  0 400 1 1.0
NE  0 201  1  1  -1. 0. 0.04 0.01 0. 0.
NH  0 201  1  1  -1. 0. 0.04 0.01 0. 0.
EN
```

Appendix C

MBC input file format

This Appendix contains a MBC input file for a 1 x 1 metre plate.

```
mbc code 1990
/ MBC data for grid = 0.1*lambda/
/ Data for g/h=1.25 (0.2m), 2.5(0.1m), and 5(0.05m)/
-1 1.00 0.              epsilon=1.00 (medium is air)
0.03183  -1.00e6        wire radius (m), conductivity (S/m)
0 0 0.  0. 0.           wire insulation parameters
300.e6 1 0.             frequency (in Hz), no. of freq, freq inc.
40 25                   NM=no. of monopoles, NP=no. of points
0  0                    NGEN=0 for pw inc
0                       LEFL = no of lumped loads
0   0   0   0   0001    Output flags: impedance, rad. power, etc.
201                     No of near field points
0   0  0
0.,0.,0.,0.
0
SEGN
            1           2
            2           3
            3           4
            4           5
            6           7
            7           8
            8           9
            9          10
           11          12
           12          13
           13          14
           14          15
           16          17
           17          18
           18          19
           19          20
           21          22
           22          23
           23          24
           24          25
            1           6
            6          11
           11          16
           16          21
            2           7
            7          12
           12          17
           17          22
            3           8
            8          13
           13          18
           18          23
            4           9
            9          14
           14          19
           19          24
            5          10
           10          15
           15          20
           20          25
```

```
COOR
 -.5000    -.5000     0.000
 -.5000    -.2500     0.000
 -.5000     0.000     0.000
 -.5000    0.2500     0.000
 -.5000    0.5000     0.000
 -.2500    -.5000     0.000
 -.2500    -.2500     0.000
 -.2500     0.000     0.000
 -.2500    0.2500     0.000
 -.2500    0.5000     0.000
  0.000    -.5000     0.000
  0.000    -.2500     0.000
  0.000     0.000     0.000
  0.000    0.2500     0.000
  0.000    0.5000     0.000
 0.2500    -.5000     0.000
 0.2500    -.2500     0.000
 0.2500     0.000     0.000
 0.2500    0.2500     0.000
 0.2500    0.5000     0.000
 0.5000    -.5000     0.000
 0.5000    -.2500     0.000
 0.5000     0.000     0.000
 0.5000    0.2500     0.000
 0.5000    0.5000     0.000
SRC
3                                ;plane wave incident
0. 0. 0.                         ;pwi: theta phi pol
NPAT
201 1 1 -1. 0. -0.08 0.01 0. 0.  #x,#y,#z,xl,yl,zl,dx,dy,dz
XEND
/ /
```

Appendix D

Junction input file format

This Appendix contains a Junction input file for a 1 x 1 metre plate.

```
  -1    1
 25   56
 1   -.5000     -.5000      0.000
 2   -.5000     -.2500      0.000
 3   -.5000      0.000      0.000
 4   -.5000     0.2500      0.000
 5   -.5000     0.5000      0.000
 6   -.2500     -.5000      0.000
 7   -.2500     -.2500      0.000
 8   -.2500      0.000      0.000
 9   -.2500     0.2500      0.000
10   -.2500     0.5000      0.000
11   0.000     -.5000      0.000
12   0.000     -.2500      0.000
13   0.000      0.000      0.000
14   0.000     0.2500      0.000
15   0.000     0.5000      0.000
16   0.2500     -.5000      0.000
17   0.2500     -.2500      0.000
18   0.2500      0.000      0.000
19   0.2500     0.2500      0.000
20   0.2500     0.5000      0.000
21   0.5000     -.5000      0.000
22   0.5000     -.2500      0.000
23   0.5000      0.000      0.000
24   0.5000     0.2500      0.000
25   0.5000     0.5000      0.000
 1       1          2
 2       2          3
 3       3          4
 4       4          5
 5       6          7
 6       7          8
 7       8          9
 8       9         10
 9      11         12
10      12         13
11      13         14
12      14         15
13      16         17
14      17         18
15      18         19
16      19         20
17      21         22
18      22         23
19      23         24
20      24         25
21       1          6
22       6         11
23      11         16
24      16         21
25       2          7
26       7         12
27      12         17
28      17         22
29       3          8
30       8         13
31      13         18
32      18         23
33       4          9
34       9         14
35      14         19
36      19         24
```

```
37       5           10
38      10           15
39      15           20
40      20           25
41       1            7
42       2            8
43       3            9
44       4           10
45       6           12
46       7           13
47       8           14
48       9           15
49      11           17
50      12           18
51      13           19
52      14           20
53      16           22
54      17           23
55      18           24
56      19           25
 0
 0
 2
   1.00000
   1.00000     1.00000     1.00000
   2.00000     2.00000     2.00000
 1
P
0.00000E+00 0.00000E+00 0.00000E+00 0.00000E+00-0.26525E-02 0.00000E+00
   3.00000E+08
  -1.00000
```